Universal classification of Weyl semimetals via sixteen irreducible Weyl molecules

Ke-Xin Pang,[*] Hui-Jing Zheng,[*] and Yan Gao[†]
State Key Laboratory of Metastable Materials Science and Technology and Hebei Key Laboratory of Microstructural Material Physics, School of Science, Yanshan University, Qinhuangdao 066004, China

(Received 3 December 2025; revised 25 April 2026; accepted 13 August 2026; published 14 September 2026)

Governed by the Nielsen-Ninomiya theorem, Weyl points (WPs) function as topological monopoles that cannot exist in isolation but must form charge-neutral assemblies in the momentum space of crystals. While these WPs are locally characterized by quantized chiral charges, the finite generating family governing their global assembly into a Weyl semimetal (WSM) phase remains undiscovered. Here, we resolve this by identifying "irreducible Weyl molecules" (IWMs) as the elementary, charge-neutral topological building blocks of WSMs. By rigorously imposing the constraints of 1651 magnetic space groups on minimal zero-sum chiral-charge sequences, we obtain exactly 16 crystallographically realizable IWMs. We establish a universal linear-combination principle, demonstrating that any crystallographically realizable charge-neutral chiral-node configuration Y within $|C| \leqslant 4$ is constructed from a linear superposition of these 16 generators X_i with non-negative integer coefficients n_i, governed by $Y = \sum_{i=1}^{16} n_i X_i$. Utilizing first-principles calculations on a predicted family of boron allotropes, we reveal that this superposition principle organizes the bulk nodal configurations and constrains the admissible end point connectivity of Fermi arcs, while the realized surface geometry remains dependent on termination, energy, and allowed inter-IWM reconstruction. Our work establishes a "periodic table" for WSMs, offering a general theoretical framework for the classification and rational design of Weyl complexes.

DOI: 10.1103/qwrz-9xm9

I. INTRODUCTION

Weyl semimetals (WSMs) represent a paradigm shift in condensed matter physics, characterized not by global invariants on a closed manifold, but by local topological singularities in the Brillouin zone (BZ)—the Weyl points (WPs) [1–4]. These WPs act as monopoles of the Berry curvature field, carrying a quantized chiral charge (Chern number) C that is robust against local perturbations. This nontrivial bulk topology manifests physically through the bulk-boundary correspondence, giving rise to Fermi-arc surface states that connect the projections of WPs with opposite chirality on the surface BZ [5–7]. These arcs serve as the spectroscopic fingerprint of the bulk chiral charges, underpinning exotic transport phenomena such as the chiral anomaly and the anomalous Hall effect [8–10].

While the elementary WP typically carries a unit charge $|C| = 1$, specific crystalline symmetries can stabilize multi-Weyl points with higher topological charges $C \in \{\pm 2, \pm 3, \pm 4\}$ [11–18]. However, the existence of these diverse local charges is rigidly constrained by the global Nielsen-Ninomiya no-go theorem [19,20], which mandates that the net chiral charge across the entire BZ must vanish. Consequently, WPs are physically forbidden from existing in isolation in WSMs; they must emerge as charge-neutral assemblies. Despite intensive efforts to compile an encyclopedia of these isolated emergent particles across various nonmagnetic and magnetic space groups (MSGs) [21–23], a fundamental theoretical gap persists: What are the fundamental topological charge-neutral component units that constitute all WSMs? Current research largely treats the nodal configuration of each material as a unique case, lacking a unified theory to decompose complex multinode configurations into universal components [6,24–26]. This suggests a missing "chemistry" of Weyl physics—a systematic framework defining how elementary "atoms" (WPs) bond into a finite set of irreducible molecular clusters that fundamentally tile the momentum space of all WSMs.

In this article, we solve this classification problem by introducing the concept of Irreducible Weyl Molecules (IWMs). By rigorously imposing the constraints of 1651 MSGs on minimal zero-sum chiral-charge sequences, we show that exactly 16 fundamental units survive as crystallographically realizable entities (Fig. 1). This result establishes a universal linear-combination principle, governed by $Y = \sum_{i=1}^{16} n_i X_i$, which decomposes any crystallographically realizable charge-neutral chiral-node configuration Y within $|C| \leqslant 4$ into a non-negative-integer superposition of IWMs X_i. Beyond a charge classification, the framework exposes rules governing the global assembly of topological charges and conceptualizes WSMs as structured "molecular crystals" in momentum space. We test the framework by decomposing the WP configurations of representative WSMs and by visualizing the three assembly forms in a predicted class of boron allotropes. We further show that the IWM content constrains

[*]These authors contributed equally to this work.
[†]Contact author: yangao9419@ysu.edu.cn

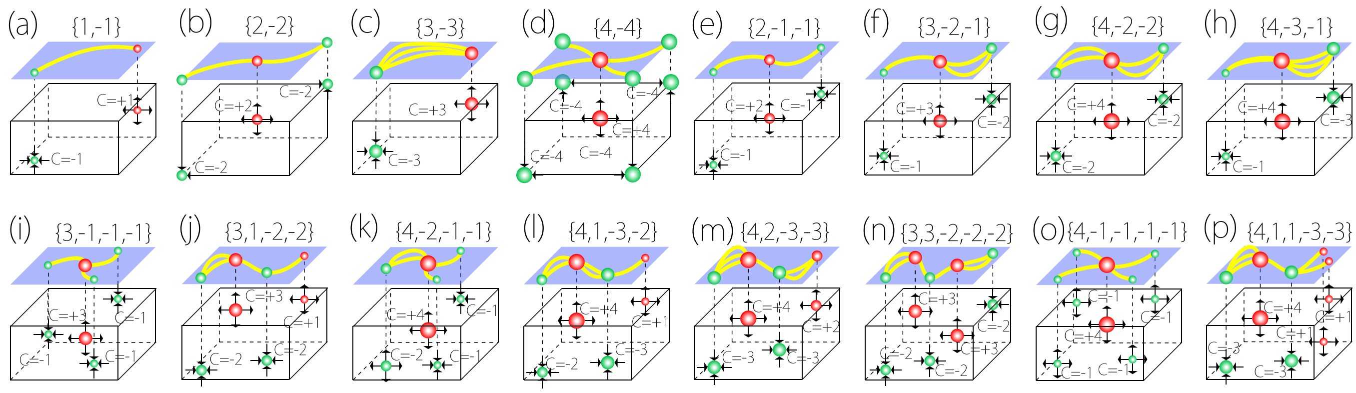

FIG. 1. Classification of the 16 IWMs. (a)–(p) Schematic representations of the 16 irreducible generators for crystallographically realizable charge-neutral Weyl-node configurations within $|C| \leqslant 4$. Red (green) spheres denote Weyl points carrying positive (negative) topological chiral charges, C. The yellow curves projected onto the blue planes schematically illustrate admissible connectivity motifs of the topological Fermi-arc surface states associated with each IWM configuration.

the admissible end point-incidence and connectivity classes of topological Fermi arcs; surface termination, energy window, and inter-IWM reconstruction select the physical realization. The resulting "periodic table" offers a unified language for classifying and rationally designing complex Weyl-node configurations.

II. MATHEMATICAL AND CRYSTALLOGRAPHIC FOUNDATION OF IRREDUCIBLE WEYL MOLECULES

In this section, we derive the finite generating family of IWMs in three steps. We first map the Nielsen-Ninomiya charge-neutrality condition to minimal zero-sum sequences over $G_0 = \{\pm 1, \pm 2, \pm 3, \pm 4\}$. A combinatorial derivation and an independent Hilbert-basis calculation yield 19 mathematical minimal zero-sum candidates. We then impose charge-coexistence and symmetry-orbit-multiplicity constraints across all 1651 magnetic space groups, separately in spinless and spinful regimes, reducing the mathematical set to 16 crystallographically realizable IWM classes. Finally, we establish the corresponding generation rule and distinguish algebraic nonuniqueness from the surface-resolved physical realization.

A. Theoretical foundation: From monopoles to molecules

WPs in the momentum space of three-dimensional crystals act as topological monopoles of the Berry curvature field, characterized by a quantized chiral charge (Chern number) C. However, the existence of these diverse local charges is subject to the global constraint of the Nielsen-Ninomiya no-go theorem, requiring a net vanishing chiral charge across the entire BZ [19,20]:

$$\sum_i C_i = 0. \tag{1}$$

This conservation law imposes a fundamental constraint: Weyl points are physically forbidden from existing as isolated entities. They must inevitably emerge in charge-neutral collections to satisfy the global topological boundary conditions.

The molecular analogy used here is algebraic and topological rather than dynamical: An IWM is a minimal charge-neutral node complex. Its bulk-boundary manifestation is encoded by Fermi-arc connectivity, which links projected sources and sinks of Berry curvature and can diagnose the physically realized organization of the nodes. In this limited sense, Fermi arcs provide an intuitive analog of bonds; they are not a dynamical mechanism that binds the bulk nodes.

To identify the elementary building blocks of this crystal, we must find the minimal clusters that satisfy charge neutrality but cannot be decomposed into smaller neutral subclusters. These minimal zero-sum units define the mathematical candidates for IWMs. At the algebraic stage, any zero-sum chiral-charge sequence over G_0 can be decomposed into mathematical minimal zero-sum generators; crystallographic realizability is imposed separately below.

B. Mathematical correspondence between minimal zero-sum sequences and irreducible Weyl molecules

We map this physical picture to combinatorial number theory. The set of allowable topological charges for WPs (atoms), constrained by crystalline symmetries, is finite [21–23]:

$$G_0 = \{\pm 1, \pm 2, \pm 3, \pm 4\}. \tag{2}$$

A collection of Weyl atoms forms an unordered sequence $S = s_1 \times s_2 \cdot \cdots \times s_t$, where $s_i \in G_0$. The set of all possible unconstrained combinations constitutes a free multiplicative Abelian monoid, denoted as $\mathcal{F}(G_0)$ [27]. The identity element of $\mathcal{F}(G_0)$ is the empty sequence, and the operation is sequence concatenation: For sequences $S_1 = s_1 \times \cdots \times s_i$ and $S_2 = s_j \times \cdots \times s_t$, their product is

$$S_1 \times S_2 = s_1 \times \cdots \times s_i \times s_j \times \cdots \times s_t \in \mathcal{F}(G_0). \tag{3}$$

The physical constraint of the no-go theorem [Eq. (1)] maps directly to the mathematical definition of a zero-sum sequence. The set of all zero-sum sequences over G_0 forms a submonoid known as a Krull monoid [27]:

$$\mathcal{B}_0 = \mathcal{B}(G_0) = \left\{ S \in \mathcal{F}(G_0) : \sigma(S) = \sum_{i=1}^{t} s_i = 0 \right\}. \tag{4}$$

Within this mathematical framework, a minimal charge-neutral configuration corresponds to a minimal zero-sum sequence of the monoid $\mathcal{B}_0$. Let $\mathcal{A}(\mathcal{B}_0)$ denote the mathematical minimal generators. An element $S \in \mathcal{A}(\mathcal{B}_0)$ is a sequence that sums to zero, but no proper subsequence of S sums to zero.

This irreducibility establishes the algebraic generating set. A key property of the Krull monoid is that any element in $\mathcal{B}_0$ can be decomposed into a product, or equivalently a non-negative-integer combination, of elements of $\mathcal{A}(\mathcal{B}_0)$. At this stage, the statement is purely mathematical: It includes 19 minimal zero-sum sequences, before charge-coexistence and symmetry-orbit-multiplicity constraints determine which generators are crystallographically realizable IWMs.

C. Derivation of the 19 mathematical minimal zero-sum candidates

To systematically identify all elements in $\mathcal{A}(\mathcal{B}_0)$, we define an equivalence relation under global chirality inversion: A sequence $S = s_1 \times \cdots \times s_t$ is equivalent to $-S = (-s_1) \times \cdots \times (-s_t)$. We adopt the convention that the element with the largest absolute charge is positive, specifically manifested in the representation of X_i where positive chiral charges within the braces {} are denoted without an explicit plus sign.

We employ the derivation operation introduced by Sissokho [28] to generate lower-order minimal sequences from higher-order ones. For a minimal zero-sum sequence $S \in \mathcal{A}(\mathcal{B}_0)$, its four-derived set $\mathcal{D}_4(S)$ is constructed recursively by (proven in Lemma 2.1 of Ref. [28]):

(1) Selecting any pair of elements s_i, s_j from a sequence $S \in \mathcal{D}_4(S)$ and replacing them with their sum $s_k = s_i + s_j$.

(2) Ensure the resulting sequence $S' = s'_1 \times \cdots \times s'_t$ satisfies

(a) $S' \in \mathcal{B}(G_0)$ (zero sum);

(b) $\|S'\|_\infty = \sup_{1\leqslant i\leqslant t} |s'_i| \leqslant 4$ (charge bound);

(c) S' is a minimal zero-sum sequence (irreducible).

(3) Add S' to $\mathcal{D}_4(S)$.

The generation of $\mathcal{A}(\mathcal{B}_0)$ proceeds by identifying the maximal elements $\mathcal{M}$—sequences that cannot be derived from any other sequence. For a given charge bound $n \in [1, 5]$, the maximal elements satisfy [28]

$$\mathcal{M}_n \subseteq \left\{a^{\lceil b/\gcd(a,b)\rceil} \times (-b)^{\lfloor a/\gcd(a,b)\rfloor} : a, b \in [1, n]\right\}. \quad (5)$$

For a charge limit of $n = 4$, we obtain

$$\mathcal{M}_4 \subseteq \mathcal{Q} = \begin{Bmatrix} 2\times(-1)^2, & 3\times(-1)^3, & 4\times(-1)^4, \\ 3^2\times(-2)^3, & 4\times(-2)^2, & 4^3\times(-3)^4 \end{Bmatrix}. \quad (6)$$

Here, the notation $x^{[k]}$ denotes that the element x appears k times in the sequence. Since $\mathcal{Q}$ contains all maximal elements, the complete set of minimal zero-sum sequences is

$$\mathcal{A}(\mathcal{B}_0) = \mathcal{D}_4^*(\mathcal{M}_4) = \mathcal{D}_4^*(\mathcal{Q}), \quad (7)$$

where D_4^* denotes the recursive closure under the derivation operation: $\mathcal{D}_4^*(\mathcal{Q}) = \bigcup_{S_i\in\mathcal{Q}} D_4(S_i)$. The hierarchical relationships among minimal zero-sum sequences form a partially ordered set (poset) $(\mathcal{A}(\mathcal{B}_0), \prec_4)$, where $S_1 \prec_4 S_2$ if and only if $S_1 \in \mathcal{D}_4(S_2)$. The Hasse diagram explicitly illustrates the evolutionary pathway from the maximal elements $\mathcal{M}_4$ to all 19 minimal zero-sum sequences, as shown in Fig. 2.

Through this rigorous derivation, we establish that $\mathcal{A}(\mathcal{B}_0)$ contains precisely 19 minimal zero-sum sequences that are inequivalent under charge conjugation and term reordering, corresponding to 19 mathematical minimal zero-sum candidates before crystallographic constraints are imposed.

D. Independent Hilbert-basis verification

As an independent verification, we cast the zero-sum condition as a non-negative integer-kernel problem [29]. The Hilbert basis computed with `4ti2` [30,31] contains 34 vectors; after identifying global chirality reversal and term reordering, these vectors reduce to exactly the same 19 inequivalent minimal zero-sum classes obtained in Sec. II C. The ordered charge coordinates, integer-cone construction, full vector list, and correspondence table are given in Appendix A.

E. Crystallographic constraints: From 19 mathematical candidates to 16 realizable irreducible Weyl molecules

Having obtained the same 19 mathematical candidates combinatorially in Sec. II C and independently through the Hilbert-basis calculation in Appendix A, we next impose crystallographic constraints. Their physical realization in crystalline materials is strictly governed by MSG symmetry. To bridge this gap, we incorporate the exhaustive constraints of the 1651 MSGs [21–23]. The enumeration is performed separately for without-SOC (single-valued representations) and with-SOC (double-valued representations) cases, using established symmetry constraints on isolated Weyl nodes [21–23]. The workflow is summarized in Fig. 3. Our systematic symmetry analysis (see Tables III–XVIII in Appendix C) establishes two rigorous selection rules for the crystallographic existence of an IWM: (1) There must exist at least one MSG that supports the simultaneous coexistence of all distinct topological charge types present in the molecule; and (2) the number of each charge type must be symmetry allowed. Applying these criteria to the 19 mathematical candidates reveals the following specific restrictions:

(1) Only magnetic space groups 196.6, 209.51, and 210.55 allow the coexistence of WPs with Chern numbers 3 and 4.

(2) Crucially, within these specific MSGs, only the Γ point can host a WP with Chern number 4.

These symmetry constraints strictly rule out 3 of the 19 mathematical candidates, as they necessitate multiple WPs with $|C| = 4$ that cannot be accommodated by any MSG:

$$\begin{aligned} &\{4, 4, -3, -3, -2\},\\ &\{4, 4, 1, -3, -3, -3\},\\ &\{4, 4, 4, -3, -3, -3, -3\}. \end{aligned} \quad (8)$$

The exclusion of the three mathematically valid zero-sum sequences listed in Eq. (8) (i.e., $\{4, 4, -3, -3, -2\}$, $\{4, 4, 1, -3, -3, -3\}$, and $\{4, 4, 4, -3, -3, -3, -3\}$) is not a mere numerical artifact, but arises from a fundamental group-theoretical obstruction, which we term the "crystallographic pigeonhole principle." It stems from an insurmountable conflict between the rotational-symmetry requirements needed

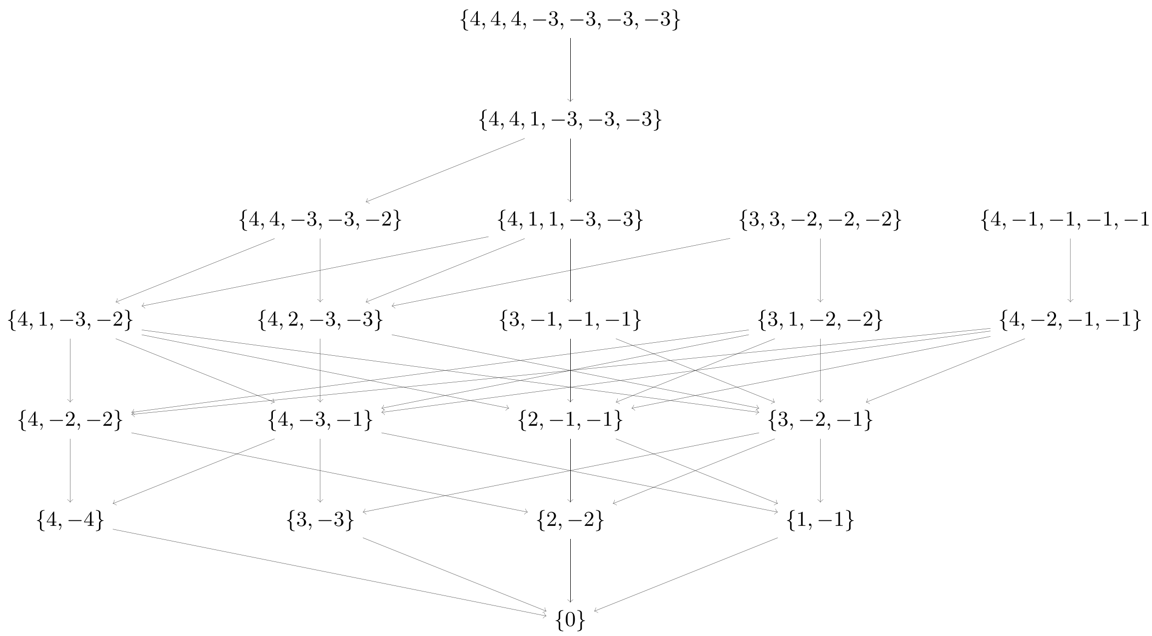

FIG. 2. The Hasse diagram of the poset P_4.

to protect high-charge nodes and the limited symmetry orbit multiplicities of the corresponding high-symmetry points or lines in the BZ.

We illustrate this mechanism collectively for these forbidden sequences:

(1) *Symmetry requirement for coexistence*: Stabilizing a Weyl node with maximum charge $|C| = 4$ requires intersecting high-fold rotational axes [21–23]. All three forbidden sequences further require that $|C| = 4$ and $|C| = 3$ nodes coexist in the same crystal. Our exhaustive symmetry screening (Tables III–XVIII in Appendix C) based on the encyclopedia of emergent particles [21–23] reveals that only three MSGs (MSGs 196.6, 209.51, and 210.55) can simultaneously support both charge types.

(2) *Global orbit multiplicity (symmetry orbit constraints)*: Analogous to Wyckoff positions in real space, symmetry operations in k space generate fixed counts of equivalent points, constraining the allowable number of each charge type. In these three specific MSGs, the rotational symmetries required to protect a $|C| = 4$ Weyl node ($\{C_{2z}, C_{2x}, C_{31}^{+}\}$ for MSG 196.6 and $\{C_{2z}, C_{2x}, C_{2a}, C_{31}^{+}\}$ for MSGs 209.51 and 210.55) exist exclusively at the Γ point, whose symmetry orbit has multiplicity 1.

(3) *The physical conflict*: The zero-sum sequences in Eq. (8) inherently demand the presence of multiple (two or three) $|C| = 4$ Weyl nodes. However, the lattice provides only one valid "slot" (the single Γ point). It is impossible to place multiple $|C| = 4$ nodes at Γ without inducing their hybridization or merging. Conversely, placing additional nodes away from Γ breaks the rotational-symmetry required to protect and stabilize their $|C| = 4$ topological charge.

Consequently, the geometric capacity of the BZ cannot accommodate the node multiplicity prescribed by these mathematical sequences, rendering them strictly forbidden in real crystalline materials. This exact physical mechanism reduces the 19 mathematical candidates to the 16 physically realizable

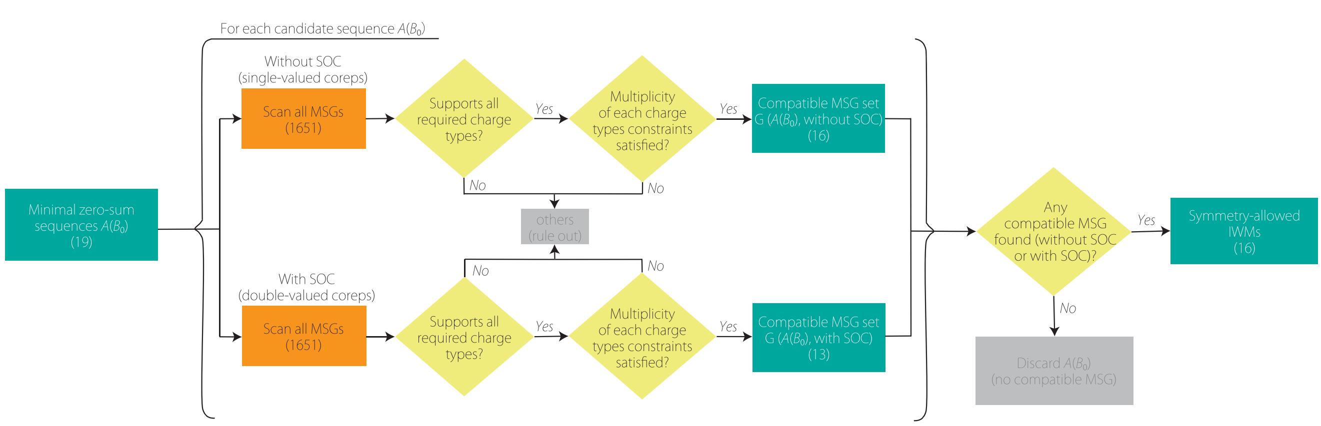

FIG. 3. Workflow for symmetry screening of the 16 IWMs in without-SOC (single-valued) and with-SOC (double-valued) regimes. Here, the single-valued and double-valued coreps denote the single-valued and double-valued corepresentations at high-symmetry points and along high-symmetry lines, respectively. The numbers in parentheses in the flowchart indicate the counts of the minimal zero-sum sequences $[\mathcal{A}(\mathcal{B}_0)]$, MSGs, and symmetry-allowed IWMs.

IWMs:

$$\begin{aligned}&\{1,-1\},\quad \{2,-2\},\quad \{3,-3\},\quad \{4,-4\},\\ &\{2,-1,-1\},\quad \{3,-2,-1\},\quad \{4,-3,-1\},\quad \{4,-2,-2\},\\ &\{3,1,-2,-2\},\quad \{3,-1,-1,-1\},\quad \{4,2,-3,-3\},\\ &\{4,1,-3,-2\},\quad \{4,-2,-1,-1\},\quad \{4,1,1,-3,-3\},\\ &\{3,3,-2,-2,-2\},\quad \{4,-1,-1,-1,-1\}.\end{aligned} \tag{9}$$

These 16 IWMs constitute a complete and minimal generating family for crystallographically realizable charge-neutral chiral-node configurations within $|C| \leqslant 4$. As established in Sec. II B, any zero-sum sequence over G_0 first decomposes into mathematical minimal generators; after the crystallographic constraints derived above are imposed, any crystallographically realizable configuration Y can be decomposed into a linear superposition of these 16 symmetry-allowed generators:

$$Y = \sum_{i=1}^{16} n_i X_i, \quad n_i \in \mathbb{Z}_{\geqslant 0}, \tag{10}$$

where X_i ($i = 1, 2, \dots, 16$) denotes the ith symmetry-allowed IWM, with each X_i implicitly including its chirality-reversed partner (the overall sign flip captured by the braces notation, where positive charges are written without explicit "+"). This formulation reduces the classification of crystallographically realizable charge-neutral chiral-node configurations within $|C| \leqslant 4$ to these 16 distinct IWMs.

F. Nonuniqueness of IWM decomposition and physical identification

We clarify the distinction between the mathematical nonuniqueness of the decomposition $Y = \sum n_i X_i$ and the identification of a physically relevant realization.

(1) Mathematical nonuniqueness (Krull monoid): The mathematical zero-sum sequences over G_0 form the Krull monoid $\mathcal{B}_0$, whose 19 inequivalent minimal generators were derived in Secs. II B–II D. After the crystallographic coexistence and orbit-multiplicity constraints are imposed, 16 of these generator classes remain crystallographically realizable as IWMs. Although this finite realizable generating family is fixed, the factorization of a composite crystallographically realizable configuration into these IWM classes need not be unique. For example, consider a system with net charges $\{+2, -2, +1, -1, +1, -1\}$. Mathematically, this can be decomposed as

(a) Option 1: $\{2, -2\} + \{1, -1\} + \{1, -1\}$.

(b) Option 2: $\{2, -1, -1\} + \{-2, 1, 1\}$.

Both validly satisfy charge conservation using the same generating family. This algebraic nonuniqueness is illustrated schematically in Fig. 4(c), where $\{2, -2\} + 2 \times \{1, -1\}$ is equivalently represented as $2 \times \{2, -1, -1\}$.

(2) Physical identification via arc connectivity: For a specified surface termination and energy window, the full Fermi-arc connectivity matrix can distinguish among algebraically admissible IWM organizations. In the unreconstructed sector $\Delta = 0$, individual IWM motifs may appear as disconnected graph components. When $\Delta \neq 0$, however, the physically relevant organization must be identified from the full connectivity matrix together with its reconstruction sector, rather than from disconnected components alone. Representative connectivity realizations for the nonunique decomposition above are shown in Fig. 4(c). For the representative unreconstructed patterns,

(a) if the physical system exhibits arcs connecting the $+2$ node directly to the -2 node, it realizes Option 1;

(b) if the physical system exhibits arcs splitting from the $+2$ node to two -1 nodes (an S-shaped connectivity), it realizes Option 2.

Thus, the finite set of irreducible generators is fixed, while the physically relevant decomposition can be constrained by the full Fermi-arc connectivity matrix and its reconstruction sector for a given surface termination and energy window.

III. UNIVERSAL FERMI-ARC CONNECTIVITY FROM IWM ASSEMBLY

In Sec. II, we established that the bulk topology of WSMs is governed by 16 IWMs, which serve as the minimal charge-neutral building blocks of WP configurations. We now turn to their manifestation on crystal surfaces. According to the bulk-boundary correspondence, each Weyl monopole in the bulk BZ generates open surface states known as Fermi arcs. These arcs connect the surface projections of Weyl points with opposite chirality. Within the molecular analogy, they provide a boundary visualization of the topological linkage among projected sources and sinks. They do not dynamically bind the bulk nodes or determine their existence.

In this section, we derive the universal connectivity rules governing Fermi arcs. We first formulate the end point-incidence constraints imposed by topology using the language of chains and boundary operators. We then show that the classification of arc connectivity reduces to an integer transportation problem. Subsequently, we incorporate the geometric winding freedom on the surface torus and formulate a general representation of Fermi-arc networks. Finally, we verify the completeness of the classification using Markov-basis enumeration implemented in `4ti2`. The resulting connectivity patterns for the 16 IWMs and representative composite WSM phases are visualized in Fig. 4.

A. Surface projections and connectivity constraints

For a given surface termination, the surface Brillouin zone can be regarded as a two-dimensional torus

$$\Sigma \cong \mathbb{T}^2. \tag{11}$$

Let

$$P = \{p_1, p_2, \dots, p_N\} \subset \Sigma \tag{12}$$

denote the set of surface projections of bulk Weyl points onto the surface Brillouin zone. Each projected point carries a nonzero integer chiral charge inherited from its corresponding bulk Weyl point,

$$C(p) \in \mathbb{Z}. \tag{13}$$

Within the framework of singular homology [32], the projected monopole distribution can be written as a zero chain:

$$\rho = \sum_{p \in P} C(p)\, p. \tag{14}$$

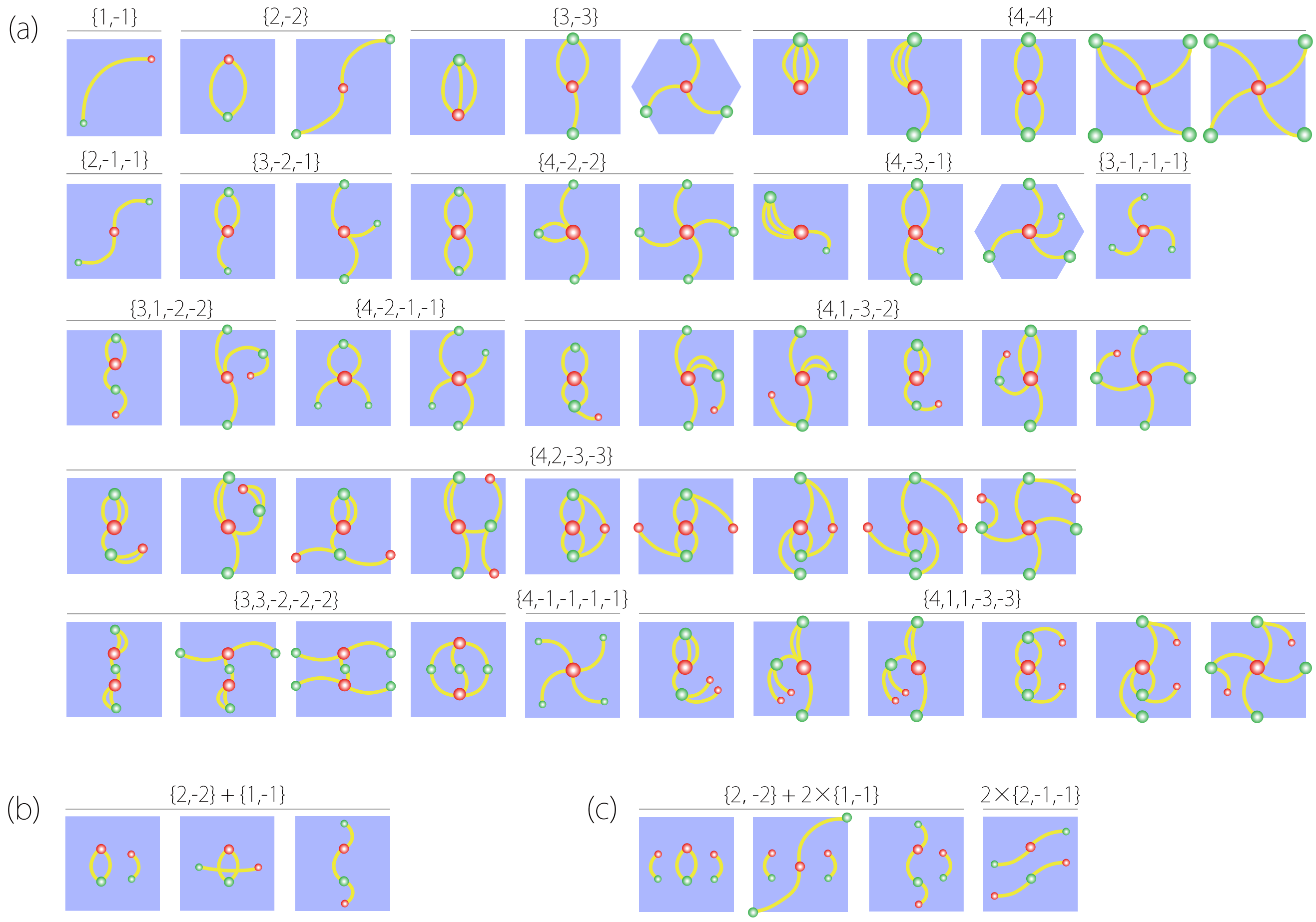

FIG. 4. Universal Fermi-arc connectivity patterns for the 16 independent IWMs and representative composite cases. (a) Fermi-arc patterns of individual IWMs, treated as basic structural units on a representative surface, where the projections of bulk WPs are spatially separated. (b) Illustration of the three superposition mechanisms—juxtaposition (left), overlap (middle), and reconfiguration (right)—using the $\{2, -2\} + \{1, -1\}$ combination as a representative example. (c) Representative Fermi-arc realizations corresponding to the algebraically nonunique decompositions $\{2, -2, +1, +1, -1, -1\} = \{2, -2\} + 2 \times \{1, -1\}$ or $2 \times \{2, -1, -1\}$. The second panel from the right illustrates a reconfigured case, analogous to the right panel of (b). Notably, the positions of the projected WPs in the surface Brillouin zone depend on the choice of surface termination. The Fermi-arc patterns shown here should therefore be regarded as a flexible connectivity map: Each projected WP (green and red) can shift with the surface orientation and may even merge with others. Red (green) spheres denote projected WPs carrying positive (negative) topological chiral charges, C, and the yellow curves denote Fermi arcs.

Because the total chiral charge in the bulk BZ must vanish according to the Nielsen-Ninomiya theorem [19,20], the projected charges satisfy

$$\sum_{p\in P} C(p) = 0. \tag{15}$$

After removing closed surface loops and topologically trivial counterpropagating pairs, we define the reduced oriented Fermi-arc network Γ_{top} as an integer one chain on Σ. The bulk-boundary correspondence imposes the boundary constraint

$$\partial\Gamma_{\text{top}} = \rho. \tag{16}$$

This condition requires that the end points of the reduced topological network reproduce exactly the projected monopole charges. Physically, it expresses the conservation of Berry-curvature flux between sources and sinks on the surface.

From this boundary condition, one obtains the following connectivity rule for the reduced topological network: Every oriented branch runs from a projected Weyl node carrying positive chiral charge to one carrying negative chiral charge. Hence, for any projected Weyl node $p \in P$, the reduced end point incidence is fixed directly by $C(p)$: A node with $C(p) > 0$ has exactly $C(p)$ outgoing topological branches and no incoming ones, whereas a node with $C(p) < 0$ has exactly $|C(p)|$ incoming topological branches and no outgoing ones. Consequently, the total number of reduced topological branches attached to p satisfies

$$\deg_{\text{top}}(p) = |C(p)|. \tag{17}$$

Equation (17) acts as a topological valence rule. A WP with $|C| = 1$ behaves as a monovalent "atom," whereas multi-Weyl points with $|C| = 2$, 3, or 4 act as multivalent centers supporting multiple arc branches. Additional topologically trivial surface contours do not change this reduced end point-

TABLE I. Complete graph-theoretic classification of end point-incidence Fermi-arc connectivities for the 16 IWMs shown in Fig. 4(a). Arc branches are oriented from positive to negative chiral charges. Matrices are listed up to permutations of identical-charge WPs (rows/columns). For four IWMs, there exist exactly two inequivalent patterns, labeled Type-A/Type-B. These entries define the sets $\mathcal{M}_i$.

IWM X_i [Eq. (9)]	Margins (α_i) versus (β_j)	Transportation-matrix classes $F^{(i,\mu)}$
$\{1, -1\}$	1 vs 1	Unique: [1]
$\{2, -2\}$	2 vs 2	Unique: [2]
$\{3, -3\}$	3 vs 3	Unique: [3]
$\{4, -4\}$	4 vs 4	Unique: [4]
$\{2, -1, -1\}$	2 vs 1, 1	Unique: $[1\ \ 1]$
$\{3, -2, -1\}$	3 vs 2, 1	Unique: $[2\ \ 1]$
$\{4, -3, -1\}$	4 vs 3, 1	Unique: $[3\ \ 1]$
$\{4, -2, -2\}$	4 vs 2, 2	Unique: $[2\ \ 2]$
$\{3, 1, -2, -2\}$	3, 1 vs 2, 2	Unique: $\begin{bmatrix} 2 & 1 \\ 0 & 1 \end{bmatrix} \sim \begin{bmatrix} 1 & 2 \\ 1 & 0 \end{bmatrix}$
$\{3, -1, -1, -1\}$	3 vs 1, 1, 1	Unique: $[1\ \ 1\ \ 1]$
$\{4, 2, -3, -3\}$	4, 2 vs 3, 3	Type-A: $\begin{bmatrix} 2 & 2 \\ 1 & 1 \end{bmatrix}$; Type-B: $\begin{bmatrix} 3 & 1 \\ 0 & 2 \end{bmatrix} \sim \begin{bmatrix} 1 & 3 \\ 2 & 0 \end{bmatrix}$
$\{4, 1, -3, -2\}$	4, 1 vs 3, 2	Type-A: $\begin{bmatrix} 2 & 2 \\ 1 & 0 \end{bmatrix}$; Type-B: $\begin{bmatrix} 3 & 1 \\ 0 & 1 \end{bmatrix}$
$\{4, -2, -1, -1\}$	4 vs 2, 1, 1	Unique: $[2\ \ 1\ \ 1]$
$\{4, 1, 1, -3, -3\}$	4, 1, 1 vs 3, 3	Type-A: $\begin{bmatrix} 2 & 2 \\ 1 & 0 \\ 0 & 1 \end{bmatrix}$; Type-B: $\begin{bmatrix} 3 & 1 \\ 0 & 1 \\ 0 & 1 \end{bmatrix} \sim \begin{bmatrix} 1 & 3 \\ 1 & 0 \\ 1 & 0 \end{bmatrix}$
$\{3, 3, -2, -2, -2\}$	3, 3 vs 2, 2, 2	Type-A: $\begin{bmatrix} 1 & 1 & 1 \\ 1 & 1 & 1 \end{bmatrix}$; Type-B: $\begin{bmatrix} 2 & 1 & 0 \\ 0 & 1 & 2 \end{bmatrix}$ (up to row/column permutations)
$\{4, -1, -1, -1, -1\}$	4 vs 1, 1, 1, 1	Unique: $[1\ \ 1\ \ 1\ \ 1]$

incidence class and are not included in the transportation matrix F.

To classify Fermi-arc connectivity patterns, we separate the projected WPs into positive and negative monopoles,

$$P_+ = \{a_1, \dots, a_m\}, \quad C(a_i) = \alpha_i > 0 \tag{18}$$

and

$$P_- = \{b_1, \dots, b_n\}, \quad C(b_j) = -\beta_j < 0. \tag{19}$$

Charge neutrality implies

$$\sum_{i=1}^{m} \alpha_i = \sum_{j=1}^{n} \beta_j. \tag{20}$$

Let f_{ij} denote the number of Fermi arcs connecting a_i to b_j. The arc connectivity can then be represented by a non-negative integer matrix

$$F = (f_{ij}) \in \mathbb{Z}_{\geqslant 0}^{m\times n}. \tag{21}$$

Flux conservation at each projected WP requires

$$\sum_{j=1}^{n} f_{ij} = \alpha_i, \quad \sum_{i=1}^{m} f_{ij} = \beta_j. \tag{22}$$

Equation (22) defines a classical integer transportation problem [29]. Each admissible matrix F represents a connectivity skeleton describing how projected WPs are linked by Fermi arcs. For a given IWM, the charge sets $\{\alpha_i\}$ and $\{\beta_j\}$ are fixed. Solving Eq. (22) yields a finite set of inequivalent connectivity matrices, summarized in Table I and visualized in Fig. 4(a).

B. Geometric winding on the surface torus

Although the connectivity skeleton fixes which projected WPs are connected, the geometric shapes of the arcs are not unique. Because the surface BZ is a torus $\mathbb{T}^2$, Fermi arcs may wind around nontrivial cycles before reaching their end points.

To characterize this freedom, we assign to each arc σ a winding vector

$$g(\sigma) = (n_x, n_y) \in \mathbb{Z}^2, \tag{23}$$

which counts the windings along the reciprocal-space directions k_x and k_y.

An arc connecting nodes a_i and b_j with winding vector g is denoted by σ_{ij}^{g}. Correspondingly, the connectivity matrix becomes winding resolved, $F_{ij}(g)$. The conservation laws generalize to

$$\sum_{j}\sum_{g} F_{ij}(g) = \alpha_i, \quad \sum_{i}\sum_{g} F_{ij}(g) = \beta_j. \tag{24}$$

The reduced topological Fermi-arc network on the surface can therefore be written as

$$\Gamma_{\text{top}} = \sum_{i,j}\sum_{g} F_{ij}(g)\sigma_{ij}^{g}. \tag{25}$$

C. Construction and reconfiguration of general Fermi-arc networks

We now formulate the surface-connectivity rule for a general WSM phase Y. As established in Sec. II, any crystallographically realizable charge-neutral chiral-node configuration within $|C| \leqslant 4$ can be decomposed into a linear superposition of the 16 symmetry-allowed IWMs:

$$Y = \sum_{i=1}^{16} n_i X_i, \quad n_i \in \mathbb{Z}_{\geqslant 0}, \tag{26}$$

where X_i denotes one of the sixteen symmetry-allowed IWMs listed in Eq. (9).

For each IWM class X_i, let $\mu \in \mathcal{M}_i$ label one of the inequivalent elementary end point-connectivity classes listed in Table I. The corresponding winding-resolved transport matrix is

$$F^{(i,\mu)}(g) = \left(F_{ab}^{(i,\mu)}(g)\right). \tag{27}$$

For the rth copy of X_i, with $r = 1, \ldots, n_i$, we choose a class $\mu_{ir} \in \mathcal{M}_i$. The entry $F_{ab}^{(i,\mu_{ir})}(g)$ denotes the number of arcs connecting a projected WP a with positive chirality to a projected WP b with negative chirality, characterized by a winding vector $g = (n_x, n_y) \in \mathbb{Z}^2$. In the absence of coupling between IWM units, the reduced topological Fermi-arc network is obtained as a direct superposition of these elementary connectivity motifs. This defines a reference, or uncoupled, transport matrix

$$F_{ab}^{(0)}(g) = \sum_{i=1}^{16} \sum_{r=1}^{n_i} F_{ab}^{(i,\mu_{ir})}(g). \tag{28}$$

Equation (28) should be understood as the additive composition rule at the level of arc-transport channels: Each IWM copy contributes one selected elementary connectivity pattern, and the direct sum of all such contributions provides a reference starting point for constructing the reduced topological surface network of the composite WSM phase Y. This is fully consistent with the linear-superposition principle established in Sec. II for the bulk WP configuration.

The physical surface configuration, however, need not remain identical to the uncoupled superposition in Eq. (28). When several IWMs coexist in the same surface BZ, their Fermi arcs may couple and reorganize. As a result, an arc that would be assigned to one elementary IWM in the reference construction can be rerouted into a connection involving projected WPs originating from another IWM. In this sense, the coexistence of multiple IWMs induces a reconstruction of the Fermi-arc transport matrix. We therefore write the general winding-resolved transport matrix as

$$F_{ab}(g) = F_{ab}^{(0)}(g) + \Delta_{ab}(g), \tag{29}$$

where $\Delta_{ab}(g) \in \mathbb{Z}$ denotes the reconstruction term generated by inter-IWM coupling. By construction, reconstruction redistributes arc channels among different node pairs, but it cannot modify the total arc incidence required at each projected WP. Therefore, $\Delta_{ab}(g)$ must satisfy the zero-marginal conditions

$$\sum_b \sum_g \Delta_{ab}(g) = 0, \quad \sum_a \sum_g \Delta_{ab}(g) = 0. \tag{30}$$

These relations indicate that reconstruction modifies the detailed pairing structure of the Fermi arcs while preserving the total number of outgoing arcs from each projected WP with positive chirality and the total number of incoming arcs to each projected WP with negative chirality. Equivalently, the full transport matrix $F_{ab}(g)$ continues to satisfy the same end point-incidence constraints as in Eq. (22), namely,

$$\begin{aligned} \sum_b \sum_g F_{ab}(g) &= \alpha_a, \\ \sum_a \sum_g F_{ab}(g) &= \beta_b, \\ F_{ab}(g) &\in \mathbb{Z}_{\geqslant 0}. \end{aligned} \tag{31}$$

With these definitions, the reduced topological Fermi-arc network associated with such a configuration Y can be written in the form

$$\Gamma_{\text{top}} = \sum_{a,b} \sum_g \left[\sum_{i=1}^{16} \sum_{r=1}^{n_i} F_{ab}^{(i,\mu_{ir})}(g) + \Delta_{ab}(g) \right] \sigma_{ab}^g. \tag{32}$$

Here, σ_{ab}^g denotes a reduced oriented surface arc connecting a and b with winding vector g. Equation (32) makes explicit that the construction of reduced topological surface networks has a two-level structure.

At the first level, the bulk chiral-charge multiset is generated by the 16 symmetry-allowed IWMs through $Y = \sum_{i=1}^{16} n_i X_i$. Correspondingly, the term $\sum_{i=1}^{16} \sum_{r=1}^{n_i} F_{ab}^{(i,\mu_{ir})}(g)$ gives a reference surface network, obtained by selecting and directly superposing one elementary Fermi-arc connectivity class for each constituent IWM copy.

At the second level, the physical surface configuration need not remain identical to this uncoupled reference pattern. The reconstruction term $\Delta_{ab}(g)$ describes the possible redistribution of arc channels among IWMs induced by surface coupling, while preserving all end point-incidence constraints. Within the reduced end point-incidence and reconstruction framework introduced here, Eq. (32) separates the admissible reduced topological surface networks into two sectors: the $\Delta \equiv 0$ sector, in which the Fermi-arc pattern is the direct superposition of elementary IWM motifs, and the $\Delta \not\equiv 0$ sector, in which inter-IWM reconfiguration occurs without changing the total node incidence. This classification is illustrated schematically in Fig. 5.

In this way, the Fermi-arc pattern associated with any crystallographically realizable configuration Y within the stated charge range can be understood as arising from a bulk-level linear combination of the 16 IWMs together with a surface-level choice between unreconstructed superposition and allowed reconstruction.

D. Complete enumeration and quotient-graph classification of Fermi-arc connectivity

To establish the completeness of the connectivity classification, we enumerate the winding-resolved transport matrices within a 3×3 repeated-zone representative domain. At fixed end point margins, the admissible matrices form an integer fiber, which is exhaustively connected using a Markov basis implemented in `4ti2`. We then quotient the raw solutions by repeated-zone translations, periodic boundary identifications, and permutations of symmetry-equivalent projected nodes carrying the same charge. The technical construction is detailed in Appendix B. The resulting inequivalent end

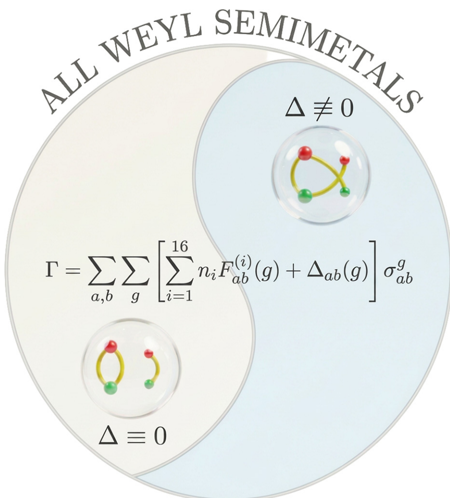

FIG. 5. Classification of surface Fermi-arc organization by the reconstruction parameter $\Delta_{ab}(g)$. Within the reduced end point-incidence and reconstruction framework introduced here, the admissible surface networks separate into a $\Delta \equiv 0$ sector, corresponding to direct superposition of elementary intra-IWM Fermi-arc motifs without inter-IWM reconstruction, and a $\Delta \not\equiv 0$ sector, corresponding to coupled inter-IWM Fermi-arc reconfigurations with conserved end point incidence.

point-connectivity classes are precisely those summarized in Fig. 4(a) and Table I.

E. Complete generation rules for Fermi-arc phases from the 16 IWM atlases

Within the stated projection, end point-incidence, and quotient-graph equivalences, Fig. 4(a) gives the elementary Fermi-arc connectivity classes associated with the 16 symmetry-allowed IWMs in Eq. (9). After a class μ_{ir} is selected for each IWM copy, these classes enter the reference superposition in Eq. (28). Combined with the bulk decomposition in Eq. (26), they provide elementary surface building blocks for general Weyl-node configurations.

The ways in which multiple elementary motifs combine on a given surface are summarized in Fig. 4(b), which contains three mechanisms.

The first mechanism is juxtaposition. In this case, the subnetworks contributed by IWM units remain disconnected as graphs on the surface torus. The full Fermi-arc pattern is then the direct superposition of the corresponding elementary motifs, namely, the uncoupled case already contained in Eq. (29) with $\Delta \equiv 0$.

The second mechanism is overlap. In the present work, this term refers specifically to arc overlap, i.e., the situation in which Fermi arcs associated with different elementary motifs geometrically intersect or overlap in the repeated-zone representation, while their end point-incidence relations remain unchanged. Such an overlap is purely a geometric feature of the surface embedding and does not alter the underlying connectivity skeleton: The same projected Weyl nodes remain connected with the same branching multiplicities required by their projected chiral charges. Consequently, overlap does not produce a new elementary connectivity family, but only a geometrically degenerate realization of the quotient-graph classes already included in Fig. 4(a). It therefore remains in the uncoupled sector with $\Delta \equiv 0$, differing from juxtaposition only in geometric embedding rather than in topological connectivity.

The third mechanism is reconfiguration. Here, arc channels originating from different elementary motifs no longer remain independent, but reconnect and are redistributed among different node pairs. This is the coupled situation described by Eq. (29) with $\Delta \not\equiv 0$, where the reconstruction term must satisfy the zero-marginal constraints in Eq. (30). A genuine reconfiguration does not occur for an arbitrary superposition of elementary motifs. In the present multichannel setting, a nontrivial reconfiguration requires the presence of projected vertices with multiple arc channels, which is precisely the situation created by higher-Chern Weyl nodes. Such a redistribution is possible only when different IWMs contain oppositely chiral higher-Chern projected nodes whose arc channels can be exchanged while preserving the total end point incidence fixed by Eq. (30). Physically, this means that the individual elementary motifs are not protected as separately conserved surface sectors: Once surface states from different motifs approach each other in surface momentum and energy and are not forbidden from mixing by symmetry, boundary-sensitive ingredients, such as surface termination, surface potential, adsorption, or other local surface perturbations can rearrange the detailed pairing pattern of the Fermi arcs without changing the bulk Weyl-node content. This picture is consistent with recent first-principles results for four-double-Weyl systems, where each $|C| = 2$ projected node emits two Fermi arcs and distinct opposite-chirality pairing channels generate different closed-loop or closed-ring surface geometries on different surfaces and enantiomers [33]. It is also supported by the explicit interface analysis of Ref. [34], which showed that coupling between Weyl semimetals with different arc connectivities can induce genuine Fermi-arc reconstruction, including reconnected zero-mode loci absent in the uncoupled motifs. Reconfiguration therefore changes the arc pairing structure while preserving the total incidence required at every projected Weyl node. If such oppositely chiral higher-Chern reconnectable channels are absent, the superposition may still realize juxtaposition or overlap, but not a nontrivial reconfiguration.

These three mechanisms exhaust the construction defined here. Juxtaposition and overlap cover direct-superposition realizations with $\Delta \equiv 0$, whereas reconfiguration covers the coupled sector with $\Delta \not\equiv 0$. Accordingly, Fig. 4(b) organizes the admissible connectivity classes within the stated charge, projection, end point-incidence, quotient-graph, and reconstruction assumptions.

Figure 4(c) illustrates an important subtlety: A fixed generating family does not imply unique factorization or a unique surface Fermi-arc realization. The same total Weyl-node configuration can admit multiple decompositions into IWMs and hence different admissible initial transport patterns. These patterns may remain distinct or become connected through allowed reconfiguration processes. Figure 4(c) is therefore a representative example of the residual connectivity freedom after the elementary IWM classes have been fixed.

Thus, the 16 elementary IWMs provide an atlas of admissible surface-connectivity classes under the assumptions above (Fig. 4). Panel (a) lists the elementary quotient-graph classes, panel (b) presents their combination mechanisms, and panel (c) illustrates the nonuniqueness of decomposing a fixed overall charge configuration. The atlas constrains end point pairing and reconstruction; the actual surface pattern is selected by boundary conditions and material-specific electronic structure.

Having established the bulk IWM classification and the associated surface-connectivity framework, we now describe the first-principles methodology and symmetry-constrained materials-discovery procedure used to identify representative realizations.

IV. COMPUTATIONAL METHODS AND MATERIALS-DISCOVERY WORKFLOW

A. First-principles methodology

The electronic structures and phonon spectra of the boron allotropes [H-P63-B_{36}, l/r-TQV-B_{24} (triangular-chain quadrangular-vortex), and l/r-THC-B_{24} (triangular helical chain)] were calculated within the framework of density functional theory [35,36] and density functional perturbation theory [37], as implemented in the QUANTUM ESPRESSO package [38]. Ion-electron interactions were modeled using norm-conserving pseudopotentials [39], with the exchange-correlation potential treated using the generalized gradient approximation of Perdew-Burke-Ernzerhof [40] type. The plane-wave kinetic energy cutoff was set to 80 Ry. BZ integrations were sampled using Γ-centered Monkhorst-Pack k-point grids [41] of $6 \times 6 \times 8$ for H-P63-B_{36} and $8 \times 8 \times 10$ for the l/r-TQV-B_{24} and l/r-THC-B_{24} phases. The Fermi-surface broadening was treated with a Gaussian smearing width of 0.003 Ry. The structures were fully relaxed until the Hellmann-Feynman forces on each atom converged to less than 10^{-4} Ry/Bohr. To investigate the topological properties, we constructed material-specific tight-binding Hamiltonians based on maximally localized Wannier functions [42]. In addition, to illustrate the symmetry-enforced $4 \times \{1, -1\}$ connectivity motif, we constructed a minimal symmetry-based tight-binding model using the MAGNETICTB package [43]; its topology and full specification are documented in Appendix G. The topological chiral charges of Weyl nodes were calculated by integrating the Berry curvature flux over closed surfaces using the Wilson loop method [44], and surface Fermi arcs were simulated via the iterative Green's function method for a semi-infinite system, as implemented in the WannierTools package [45].

B. Symmetry-constrained workflow for the discovery of IWM states in boron allotropes

While the IWM framework derived in this work is applicable to systems with strong spin-orbit coupling (SOC) (as detailed in Tables III–XVIII in Appendix C, with representative material realizations listed in Table XIX in Appendix D), we strategically select light-element boron allotropes as the validation platform. The weak SOC and versatile bonding in boron provide a "clean limit" electronic structure, which is essential for unambiguously verifying the linear superposition principle of IWMs without the interference of complex band entanglements typical of heavy-element compounds. Specifically, these allotropes allow us to construct and visualize the three fundamental assembly mechanisms—single IWM, integer multiplicity, and hybrid superposition—and to demonstrate how the intricate "spider-web" Fermi-arc connectivity emerges from the superposition of elementary Fermi-arc motifs associated with IWMs (Fig. 4).

In addition to the first-principles calculations described above, the boron allotropes considered in this work were identified through a symmetry-constrained generation-screening-identification workflow, as summarized in Fig. 6. Starting from the elemental composition (boron) and target space groups compatible with the elementary IWM $\{2, -1, -1\}$, candidate crystal structures were randomly generated using the `PyXtal` package [46], placing boron atoms on symmetry-allowed Wyckoff positions. The resulting structures were then subjected to geometric screening to eliminate crystallographically unreasonable or weakly connected configurations, retaining only three-dimensionally connected boron frameworks. These candidates were further prescreened via machine-learning-assisted structural relaxation using `CHGNet` [47] together with phonon analysis using `Phonopy` [48], where any structure exhibiting imaginary phonon modes was discarded.

The remaining dynamically stable three-dimensional (3D) boron frameworks were then used as input for first-principles electronic-structure calculations within QUANTUM ESPRESSO [38]. At this stage, the structures were further fully relaxed, after which their electronic band structures were computed to identify candidate topological semimetals, and among them those satisfying the more stringent criterion of ideal topological semimetals—namely, systems whose low-energy spectra near the Fermi level are not obscured by excessive trivial band entanglement. The resulting ideal topological semimetal candidates were subsequently analyzed at the Weyl-node level using `Wannier90` [42] and `WannierTools`-based [45] calculations, including the determination of Weyl-node positions, chiral charges, and the associated surface Fermi arcs.

For the boron systems considered here, the symmetry-constrained workflow leads to a progressive reduction of the candidate set at each stage. Geometric screening retains 19301 three-dimensionally connected boron allotropes from the symmetry-generated structures. Machine-learning-assisted relaxation and phonon prescreening then reduce this number to 216 dynamically stable candidates. Subsequent first-principles structural optimization and band-structure calculations identify 13 topological semimetal candidates, of which 9 satisfy the criteria for stable ideal Weyl semimetals. Among these, four are finally classified as hosting $\{2, -1, -1\}$-type IWMs. The full statistics of this generation-screening-identification procedure are summarized in Fig. 6.

Finally, the stable ideal Weyl semimetals obtained in this manner were classified within the IWM framework, from which three representative boron allotropes were selected to realize the single-IWM, integer-multiplicity, and hybrid-superposition assembly modes, respectively. This workflow is not intended as an unconstrained search for the thermodynamic ground state of boron, but rather as a targeted strategy to identify structurally viable and electronically clean boron platforms suitable for validating the universal superposition principle of IWMs.

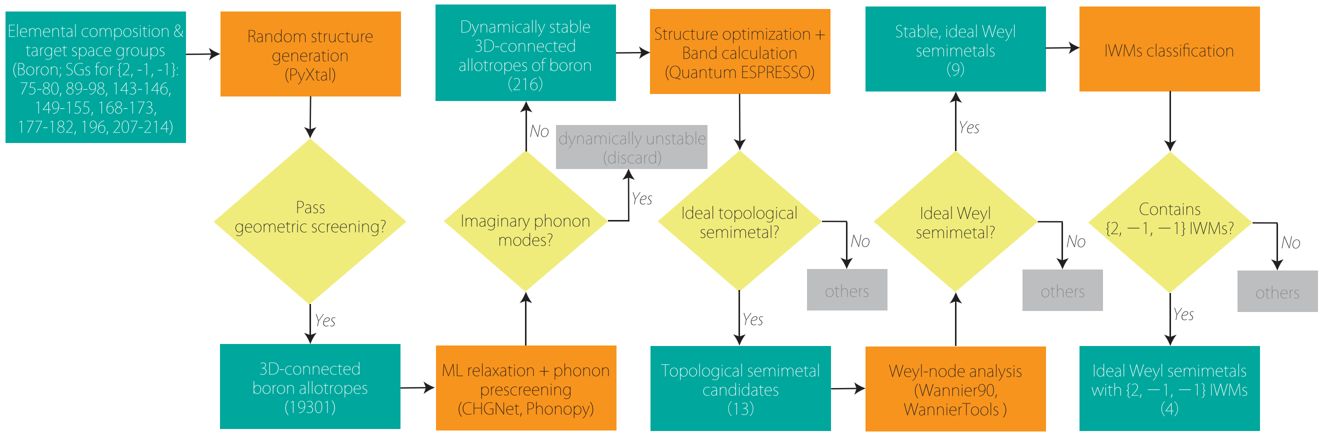

FIG. 6. Workflow for the symmetry-constrained discovery of Weyl semimetals hosting specific IWM configurations in three-dimensional boron allotropes. Starting from the elemental composition (boron) and target space groups compatible with the elementary IWM $\{2, -1, -1\}$ (see Table VII in Appendix C) in Type-II magnetic space groups without spin-orbit coupling, candidate crystal structures are generated using PyXtal under symmetry constraints. After geometric screening, 19 301 three-dimensionally connected boron allotropes are retained. Subsequent CHGNet-based relaxation and Phonopy prescreening reduce this set to 216 dynamically stable structures. First-principles structural optimization and band calculations using Quantum ESPRESSO identify 13 topological semimetal candidates, among which 9 are stable ideal Weyl semimetals. Final IWM classification yields four ideal Weyl semimetals containing $\{2, -1, -1\}$ IWMs. The three representative cases realize the three $\{2, -1, -1\}$-based assembly modes: a single IWM $\{2, -1, -1\}$, an integer multiple $2 \times \{2, -1, -1\}$, and a hybrid superposition $2 \times \{2, -1, -1\} + 4 \times \{1, -1\}$.

C. Dynamical, mechanical, and energetic stability

The five predicted boron phases exhibit no imaginary phonon branches along the calculated high-symmetry paths, as shown in Fig. 9 in Appendix F, and their elastic constants satisfy the relevant mechanical-stability criteria listed in Table XXII in Appendix E. Their calculated total energies are $-6.36\,\mathrm{eV/B}$ for H-P6_3-B_{36}, $-6.27\,\mathrm{eV/B}$ for the l/r-TQV-B_{24} pair, and $-6.16\,\mathrm{eV/B}$ for the l/r-THC-B_{24} pair, as listed in Table XXI in Appendix E. These calculations establish dynamically and mechanically stable theoretical platforms under the stated computational conditions; they do not imply that the phases are thermodynamic ground states or presently synthesizable.

V. FIRST-PRINCIPLES REALIZATIONS IN BORON ALLOTROPES

The symmetry-constrained workflow identifies three representative boron allotropes realizing the three elementary assembly forms of the IWM framework: a single IWM, an integer multiple of one IWM, and a hybrid superposition of distinct IWMs. We analyze these three cases in sequence below.

A. Single irreducible Weyl molecule

We first address the fundamental building block, the $\{2, -1, -1\}$ IWM, realized in the hexagonal H-P6_3-B_{36} allotrope (space group $P6_3$, No. 173). As shown in Fig. 7(a), the primitive cell contains 36 boron atoms arranged in intralayer puckered three-, five-, and six-membered rings that couple along the c axis through interlayer stacking. Our first-principles calculations reveal a clean band structure near the Fermi level (E_F), dominated by crossings between the highest occupied (Band 54) and lowest unoccupied (Band 55) bands [Fig. 7(b)]. In the entire BZ, these crossings manifest as three isolated points [Fig. 7(c)]: one located precisely at the high-symmetry Γ point (W_2) and two along the Γ-A path (W_1). The dispersion around W_2 exhibits a quadratic behavior in the k_x-k_y plane [Fig. 7(d)] but remains linear along k_z [Fig. 7(b)], a hallmark of a double Weyl fermion. To unambiguously determine the topological charges, we calculated the flux of the Berry curvature through closed surfaces enclosing each node [Fig. 7(e)]. The evolution of Wannier charge centers (WCCs) confirms that W_2 carries a chiral charge of $C = +2$, while the two symmetry-equivalent W_1 points each carry $C = -1$. The net chirality vanishes $[\sum C_i = +2 + (-1) + (-1) = 0]$, satisfying the Nielsen-Ninomiya theorem. Consequently, the global topological configuration of H-P6_3-B_{36} is uniquely identified as the single IWM $\{2, -1, -1\}$.

Importantly, the surface-state topology reflects this $\{2, -1, -1\}$ IWM configuration. The (100) surface bands [Fig. 7(f)] and constant-energy contour at $-50\,\mathrm{meV}$ [Fig. 7(g)] display a double-Fermi-arc pattern. Two Fermi arcs emerge from the projection of the W_2 node with $C = +2$ and terminate separately at the two equivalent W_1 nodes with $C = -1$, forming a characteristic S-shaped motif. This connectivity provides a diagnostic spectroscopic signature of the $\{2, -1, -1\}$ IWM. On the (001) surface, the three WPs project onto the same $\bar{\Gamma}$ point and produce four resolved arcs (Fig. 12 in Appendix F), furnishing a complementary signature of the three-terminal complex.

B. Integer multiple of an irreducible Weyl molecule

Having established the $\{2, -1, -1\}$ IWM, we now turn to a WSM with the nodal configuration $Y = 2 \times X_i$ (where $X_i = \{2, -1, -1\}$), composed of two copies of the same IWM. This configuration is realized in l-TQV-B_{24} (triangular-chain quadrangular-vortex) [Fig. 7(h)], a left-handed chiral tetrag-

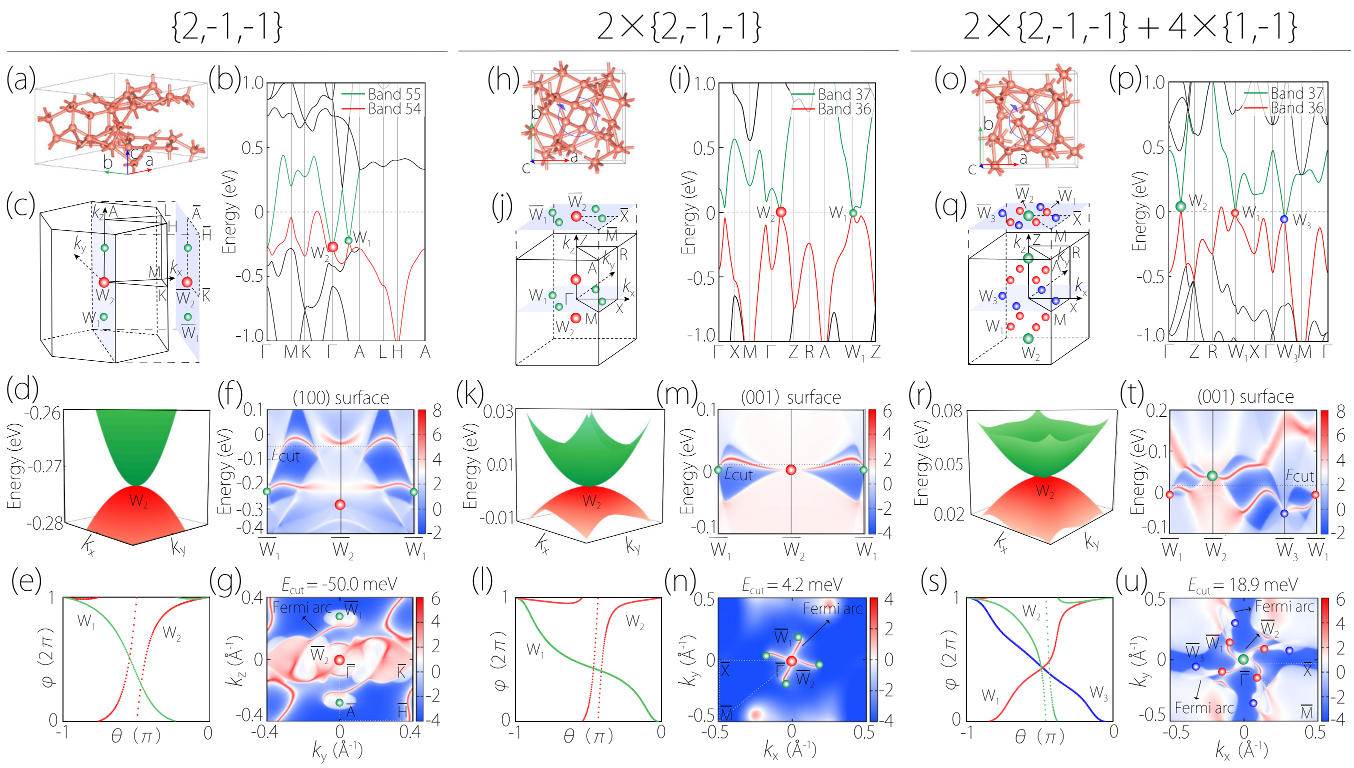

FIG. 7. Material realization of IWMs and the linear-superposition principle in boron allotropes. (a)–(g) Elementary IWM {2, −1, −1} in H-P6$_3$-B$_{36}$. (a) Primitive cell. (b) Electronic band structure showing crossings at Γ and along Γ–*A*. (c) Distribution of WPs in the bulk BZ. (d) Quadratic dispersion of the $C = +2$ WPs (W_2) in the k_x-k_y plane. (e) Evolution of WCCs confirming chiral charges $C = +2$ for W_2 and $C = -1$ for W_1. (f) (100) surface-state bands and (g) isoenergy contour at −50 meV. (h)–(n) Integer-multiplicity IWM 2 × {2, −1, −1} in *l*-TQV-B$_{24}$. (h) Primitive cell. (i) Band structure. (j) BZ distribution of six WPs. (k) Quadratic dispersion of W_2. (l) WCC evolution yielding $C = +2$ (W_2) and $C = -1$ (W_1). (m) (001) surface states and (n) isoenergy contour at 4.2 meV. (o)–(u) Hybrid superposition 2 × {2, −1, −1} + 4 × {1, −1} in *l*-THC-B$_{24}$. (o) Primitive cell. (p) Band structure. (q) Distribution of 14 WPs in the BZ. (r) Quadratic dispersion of W_2. (s) WCC calculations identifying $C = -2$ for W_2, $C = +1$ for W_1, and $C = -1$ for W_3. (t) (001) surface states and (u) isoenergy contour at 18.9 meV exhibiting a complex "spider-web" Fermi-arc pattern consistent with the admissible connectivity motifs of the constituent IWMs. Bulk and projected Weyl nodes are labeled by their chiral charges (red for positive and green for negative).

onal crystal (space group $P4_3$, No. 78) with 24 atoms per primitive cell. Its two interpenetrating structural motifs are width-2 triangular boron helical chains and vertex-sharing triangular boron spirals of the same handedness, both coiling around a central four-membered-ring vortex. The structure lacks inversion and mirror planes while preserving a four-fold screw axis along [001]. The right-handed enantiomer *r*-TQV-B$_{24}$ (space group $P4_1$, No. 76) has the same calculated total energy per atom and opposite structural chirality [Fig. 10(b) in Appendix F].

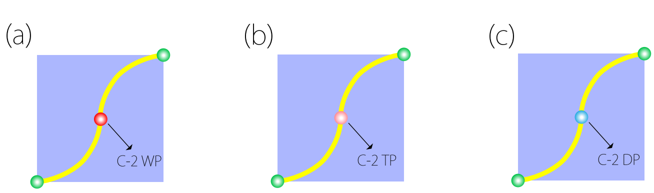

FIG. 8. Universality of the IWM theory for chiral particles with different band degeneracies. Schematic representation of the {2, −2} IWM where the central node with topological charge $C = +2$ is realized as (a) a twofold-degenerate charge-2 Weyl point (C-2 WP), (b) a threefold-degenerate charge-2 triple point (C-2 TP), and (c) a fourfold-degenerate charge-2 Dirac point (C-2 DP). Despite their different local degeneracies and dispersions, the three realizations belong to the same {2, −2} IWM class and obey the same topological end point-incidence constraint (yellow curves).

Notably, only bands 36 and 37 intersect near E_F in *l*-TQV-B$_{24}$ [Fig. 7(i)]. Across the BZ, these crossings produce six isolated WPs [Fig. 7(j)]: two W_2 points along Γ-*Z* and four W_1 points in the $k_z = 0$ plane; their coordinates and multiplicities are listed in Table XXIII in Appendix E. The W_2 dispersion is quadratic in the k_x-k_y plane [Fig. 7(k)] and linear along k_z, consistent with a double Weyl fermion and with the −1 ratio of the fourfold-screw eigenvalues of the crossing bands [11]. The WCC evolution [Fig. 7(l)] assigns $C = +2$ to each W_2 and $C = -1$ to each of the four W_1 nodes, identifying the global configuration as 2 × {2, −1, −1}.

The 2 × {2, −1, −1} content constrains the surface end point incidence. On the (001) surface, the spectrum [Fig. 7(m)] and contour at 4.2 meV [Fig. 7(n)] show arcs from the two $\bar{W}_2$ projections to the four equivalent $\bar{W}_1$ points, forming two interleaved *S*-shaped motifs. The (100) surface exhibits the same doubled-IWM content in another embedding (Fig. 13 in Appendix F). For this surface and energy window, the arcs can be traced to the two IWM motifs without cross-unit reconstruction. The right-handed enantiomer reverses all WP chiralities while preserving the corresponding incidence structure (Fig. 14 in Appendix F).

C. Hybrid superposition of irreducible Weyl molecules

Finally, we consider a hybrid of distinct IWM types in the l-THC-B_{24} (triangular helical chain) allotrope (space group $P4_3$, No. 78). This tetragonal crystal consists of 24 boron atoms forming homochiral triangular helical chains [Fig. 7(o)]. We focus on l-THC-B_{24}; the structure and calculated topology of its right-handed enantiomer are shown in Figs. 11 and 15 in Appendix F.

Our calculations show that the highest occupied (36) and lowest unoccupied (37) bands cross to form 14 Weyl nodes in the whole BZ [Figs. 7(p) and 7(q)]: two W_2 points along the Γ-Z path, eight W_1 points, and four W_3 points at general momenta. The W_2 point exhibits quadratic dispersion in the k_x-k_y plane [Fig. 7(r)] and linear dispersion along the k_z direction—a clear signature of a $|C| = 2$ WP protected by fourfold screw symmetry. This is further confirmed by the -1 ratio of the fourfold-screw eigenvalues of the two crossing bands [11]. The evolution of WCCs [Fig. 7(s)] confirms that the two W_2 points carry $C = -2$, the eight W_1 points carry $C = +1$, and the four W_3 points carry $C = -1$. Combining the bulk chiral-charge distribution with the calculated (001)-surface connectivity at the selected energy, we identify the physically realized decomposition of l-THC-B_{24} as

$$Y = 2 \times \{2, -1, -1\} + 4 \times \{1, -1\}. \tag{33}$$

A global reversal of chirality yields equivalent IWMs in our classification (e.g., $\{-2, +1, +1\}$ and $\{+2, -1, -1\}$).

The composite IWM content $2 \times \{2, -1, -1\} + 4 \times \{1, -1\}$ constrains the allowed end points of the apparently complex surface network. On the (001) surface, the spectrum [Fig. 7(t)] and constant-energy contour at 18.9 meV [Fig. 7(u)] display a "spider-web" pattern: two crossed S-shaped motifs associated with the doubled $\{2, -1, -1\}$ content, together with four additional arcs connecting the $C = +1$ W_1 and $C = -1$ W_3 projections. This pattern is a diagnostic realization of the hybrid superposition under the selected surface termination and energy window. To independently isolate the unit-charge sector entering this hybrid configuration, we also constructed a symmetry-based tight-binding reference model realizing $4 \times \{1, -1\}$. Its bulk topology, Wilson-loop charges, and surface Fermi-arc connectivity are presented together with the complete model specification in Appendix G.

VI. DISCUSSION

A. Relation to existing classification paradigms

We now place the IWM construction in relation to established topological-classification frameworks and clarify its range of applicability. The defining distinction is organizational: Existing approaches primarily diagnose local band crossings or band representations, whereas the IWM framework classifies how quantized chiral nodes assemble globally into irreducible neutral complexes.

First, the "Encyclopedia of emergent particles" and related symmetry-based classifications systematically catalog which isolated band crossings are symmetry allowed in the 1651 magnetic space groups, including their degeneracies, little-group structures, and topological charges [21–23]. These works provide the local building inventory of topological nodes. Our framework operates at a different level. Starting from the allowed chiral charges, it imposes the global Nielsen-Ninomiya neutrality constraint [19,20] and identifies the minimal charge-neutral clusters (i.e., IWMs) that cannot be further decomposed into smaller neutral subsets. In this sense, the encyclopedia answers what kinds of isolated chiral nodes can exist locally, whereas the IWM framework answers how such nodes must organize globally into irreducible neutral molecules and how crystallographically realizable charge-neutral chiral-node configurations within $|C| \leqslant 4$ are generated from them. The former constitutes a catalog of nodes, whereas the latter provides an assembly theory of IWMs within chiral topological semimetals.

Second, topological quantum chemistry (TQC) and symmetry-based indicators classify topological phases from the viewpoint of band representations, symmetry eigenvalues, and compatibility relations [49,50]. These methods are exceptionally powerful for diagnosing global band topology, especially in gapped systems, and for identifying symmetry-detectable topological semimetal features. However, they are not formulated to provide a minimal decomposition of a chiral nodal configuration into charge-neutral elementary units, nor do they directly determine the detailed stoichiometry of Weyl charges or the connectivity atlas of surface Fermi arcs. The IWM framework fills precisely this gap: It resolves the nodal content into irreducible chiral-neutral modules and further translates these bulk modules into surface-connectivity constraints.

Third, it is important to distinguish the present notion of "irreducibility" from other common uses of the word in topological-band theory. Our irreducibility is not representation-theoretic irreducibility of a little-group representation, nor irreducible band representation in the sense of TQC, nor merely minimal multiplicity under a symmetry orbit. Instead, it is charge-neutrality irreducibility: An IWM is a minimal zero-sum chiral cluster that cannot be partitioned into smaller charge-neutral subclusters. This distinction is essential. The object classified here is not an isolated local degeneracy and not a band representation, but a globally neutral topological node complex in momentum space. Accordingly, the IWM framework should be understood as a complementary layer of classification, orthogonal to local symmetry diagnosis and to representation-based topology.

B. Generality across multifold fermionic and bosonic chiral systems

The IWM construction is fundamentally based on chiral topological charge, rather than on the degeneracy of band-crossing points. The only local datum required for a node to enter the framework is that it carries a well-defined integer chiral charge, namely, a quantized Chern number obtained from the Berry-flux integral over a closed surface enclosing the node. Once this charge is defined, the subsequent logic of the theory depends only on three ingredients: charge additivity, global neutrality in the BZ, and the end point-incidence constraints that determine the connectivity of surface arcs. None of these ingredients requires the node to be a conventional twofold-degenerate Weyl point.

For this reason, the present framework applies equally to unconventional chiral band crossings with higher degeneracy, provided that they carry quantized chiral charge. Well-known examples include spin-1 Weyl fermions [51–53] and other multifold chiral fermions in chiral crystals [51–56]. In all such cases, the local band degeneracy may differ substantially, while the global topological bookkeeping relevant to the linear superposition of IWMs remains unchanged.

This is precisely the point illustrated schematically in Fig. 8. The same IWM $\{2, -2\}$ can be realized by different local quasiparticles: a twofold-degenerate charge-2 Weyl point (C-2 WP), a threefold-degenerate charge-2 triple point (C-2 TP), or a fourfold-degenerate charge-2 Dirac point (C-2 DP). These realizations are microscopically distinct in local dispersion and symmetry representation, yet they are topologically equivalent at the level relevant to the present theory because they carry the same chiral charge content and therefore obey the same neutrality rule and the same arc-incidence constraints. In other words, the invariant object in our framework is not the degeneracy label of the node, but the chiral-charge composition of the entire nodal set.

A representative material example is furnished by the chiral-crystal family CoSi/RhSi, where unconventional multifold fermions carry nonzero chiral charge and generate long topological Fermi arcs [51–53]. Within the present viewpoint, such systems are classified by the same charge-neutral assembly principle as ordinary Weyl semimetals. Therefore, the IWM framework should not be interpreted narrowly as a theory of only simple twofold Weyl points; rather, it is a general classification language for chiral-node configurations whose constituent charges lie within $|C| \leqslant 4$, irrespective of the local band degeneracy.

The same logic extends naturally beyond electronic band structures. The IWM framework does not rely on Fermi statistics, electron filling, or any specifically fermionic notion. Its prerequisites are quantized chiral charge, global charge neutrality over the BZ, and boundary states whose connectivity is governed by the same charge-conservation principle. These conditions also arise in topological bosonic spectra, so the framework is equally applicable to bosonic systems whenever their band crossings are chiral in the same topological sense.

A particularly important example is provided by topological chiral phonons. Over the past few years, a series of works have established that phonon spectra can host Weyl points, spin-1 Weyl points, charge-2 Weyl points, charge-3 Weyl points, and even charge-4 Weyl points, together with surface phonon arcs [57–61]. In such systems, the local quasiparticles are bosonic normal modes rather than electronic Bloch states, but the enclosed Berry flux and the resulting chiral charges are defined in exactly the same topological manner. Consequently, the decomposition into irreducible neutral chiral molecules remains valid. As shown in Table XX in Appendix D, a variety of known topological phonon materials can already be organized naturally within the 16-IWM framework.

An analogous extension holds for photonic systems. Weyl points and helicoid surface states have been theoretically proposed and experimentally observed in three-dimensional photonic crystals and metamaterials [62–65]. These photonic Weyl nodes likewise carry quantized topological charge and exhibit surface-arc connectivity governed by the same source-sink structure in momentum space. Therefore, once the relevant photonic crossings are isolated and assigned integer chiral charge, they can be classified by the same irreducible zero-sum principle used here for electronic Weyl matter.

From this perspective, the true scope of the IWM framework is broader than "Weyl semimetals" in the narrow electronic sense. Its natural domain encompasses the class of chiral topological quasiparticle systems, irrespective of whether the quasiparticles are electrons, phonons, photons, or other bosonic excitations. What remains universal across these realizations is not the microscopic origin of the bands, but the topological algebra of chiral charge: local quantization, global neutrality, irreducible zero-sum decomposition, and boundary connectivity. This is the sense in which the present theory provides a universal classification principle.

C. Predictive scope and boundary dependence of Fermi arcs

The decomposition is a classification of chiral-charge multisets rather than a unique factorization of a Hamiltonian or material phase. When a charge set admits multiple algebraic factorizations, the projected surface network, surface termination, energy window, and reconstruction term $\Delta_{ab}(g)$ determine which connectivity realization is physically relevant. The framework therefore constrains admissible end point-incidence and quotient-graph classes; it does not fix material-specific arc lengths, curvature, spectral weight, or the boundary-selected pairing without further calculation.

D. Symmetry-guided inverse design and material implications

The boron allotropes and their enantiomeric counterparts, together with the survey of representative WSMs in Appendix D, test the IWM linear-combination framework across single, repeated, and hybrid assemblies. This organizing principle reduces the broad variety of crystallographically realizable charge-neutral Weyl-node configurations to nonnegative-integer combinations of the 16 IWMs summarized in Fig. 1.

This separation suggests an inverse-design strategy. One may first select an IWM or combination of IWMs, use Appendix C to identify compatible magnetic space groups and charge multiplicities, and then search within those symmetry classes for electronically clean realizations. The same search logic can be extended to the multifold fermionic and bosonic chiral systems discussed above and cataloged in Appendix D.

The IWM framework therefore supplies a complementary global assembly layer that connects local chiral nodes, crystallographic realizability, surface-connectivity classes, and symmetry-guided materials design.

VII. CONCLUSION

In summary, we have established that WSMs constitute a "molecular crystal" in momentum space, constructed from a finite complete generating family of 16 crystallographically realizable IWMs that serve as the fundamental building blocks of crystallographically realizable charge-neutral chiral-node configurations within $|C| \leqslant 4$. This classification establishes

TABLE II. Correspondence between the Hilbert basis $\mathcal{H}$ and the minimal zero-sum sequences $\mathcal{A}(\mathcal{B}_0)$ (i.e., the mathematical IWM candidates).

No.	$\mathcal{H}$	$\mathcal{A}(\mathcal{B}_0)$
1	(1, 0, 0, 0, 1, 0, 0, 0)	{1, −1}
2	(0, 1, 0, 0, 0, 1, 0, 0)	{2, −2}
3	(0, 0, 1, 0, 0, 0, 1, 0)	{3, −3}
4	(0, 0, 0, 1, 0, 0, 0, 1)	{4, −4}
5	(0, 1, 0, 0, 2, 0, 0, 0) (2, 0, 0, 0, 0, 1, 0, 0)	{2, −1, −1}
6	(0, 0, 1, 0, 1, 1, 0, 0) (1, 1, 0, 0, 0, 0, 1, 0)	{3, −2, −1}
7	(0, 0, 0, 1, 0, 2, 0, 0) (0, 2, 0, 0, 0, 0, 0, 1)	{4, −2, −2}
8	(0, 0, 0, 1, 1, 0, 1, 0) (1, 0, 1, 0, 0, 0, 0, 1)	{4, −3, −1}
9	(0, 0, 1, 0, 3, 0, 0, 0) (3, 0, 0, 0, 0, 0, 1, 0)	{3, −1, −1, −1}
10	(1, 0, 1, 0, 0, 2, 0, 0) (0, 2, 0, 0, 1, 0, 1, 0)	{3, 1, −2, −2}
11	(0, 0, 0, 1, 2, 1, 0, 0) (2, 1, 0, 0, 0, 0, 0, 1)	{4, −2, −1, −1}
12	(1, 0, 0, 1, 0, 1, 1, 0) (0, 1, 1, 0, 1, 0, 0, 1)	{4, 1, −3, −2}
13	(0, 1, 0, 1, 0, 0, 2, 0) (0, 0, 2, 0, 0, 1, 0, 1)	{4, 2, −3, −3}
14	(0, 0, 2, 0, 0, 3, 0, 0) (0, 3, 0, 0, 0, 0, 2, 0)	{3, 3, −2, −2, −2}
15	(0, 0, 0, 1, 4, 0, 0, 0) (4, 0, 0, 0, 0, 0, 0, 1)	{4, −1, −1, −1, −1}
16	(2, 0, 0, 1, 0, 0, 2, 0) (0, 0, 2, 0, 2, 0, 0, 1)	{4, 1, 1, −3, −3}
17	(0, 0, 0, 2, 0, 1, 2, 0) (0, 1, 2, 0, 0, 0, 0, 2)	{4, 4, −3, −3, −2}
18	(1, 0, 0, 2, 0, 0, 3, 0) (0, 0, 3, 0, 1, 0, 0, 2)	{4, 4, 1, −3, −3, −3}
19	(0, 0, 0, 3, 0, 0, 4, 0) (0, 0, 4, 0, 0, 0, 0, 3)	{4, 4, 4, −3, −3, −3, −3}

a universal linear-combination principle, governed by the formula $Y = \sum_{i=1}^{16} n_i X_i$, which reduces any such configuration Y to a non-negative-integer superposition of these units X_i. Through the prediction of three boron allotropes hosting single, double, and composite IWMs, we have illustrated that this superposition principle organizes the bulk Weyl-node configuration and constrains the admissible end point connectivity of topological Fermi arcs, while the realized surface geometry remains dependent on termination, energy, and allowed inter-IWM reconstruction. Our framework delivers the "periodic table" for Weyl physics, offering a unifying language for classifying, diagnosing, and rationally designing Weyl complexes.

ACKNOWLEDGMENTS

The authors thank Weikang Wu and Shengyuan A. Yang for valuable discussions. This work was supported by the National Natural Science Foundation of China (Grant No. 12304202), Hebei Natural Science Foundation (Grant No. A2023203007), and Science Research Project of Hebei Education Department (Grant No. BJK2024085).

DATA AVAILABILITY

There are no publicly available research data or software supporting this manuscript. Requests for further information or data should be sent to the authors.

APPENDIX A: HILBERT-BASIS VERIFICATION OF THE MINIMAL ZERO-SUM ENUMERATION

For an independent integer-programming verification, identifying minimal zero-sum sequences is equivalent to solving the homogeneous linear Diophantine equation $\sum_{g\in G_0} n_g g = 0$, where n_g denotes the number of Weyl atoms with charge g. We use the ordered charge coordinates

$$(-1, -2, -3, -4, +1, +2, +3, +4) \tag{A1}$$

and the one-row integer matrix

$$A = (-1, -2, -3, -4, 1, 2, 3, 4). \tag{A2}$$

The set of non-negative integer solutions forms the integer cone [29]

$$C = \{\mathbf{n} \in \mathbb{Z}^8_{\geqslant 0} | A\mathbf{n} = 0\}. \tag{A3}$$

Its Hilbert basis $\mathcal{H}$ is the unique minimal generating set of the affine monoid C and therefore enumerates the indecomposable charge-balanced structures [30]. Supplying A to `4ti2` gives the following 34 Hilbert-basis vectors [31]:

$$\begin{aligned}\mathcal{H} = \{&(1, 0, 0, 0, 1, 0, 0, 0), (0, 1, 0, 0, 2, 0, 0, 0), (0, 0, 1, 0, 3, 0, 0, 0),\\ &(0, 0, 0, 1, 4, 0, 0, 0), (0, 0, 4, 0, 0, 0, 0, 3), (0, 0, 0, 3, 0, 0, 4, 0),\\ &(1, 0, 0, 2, 0, 0, 3, 0), (0, 0, 3, 0, 1, 0, 0, 2), (0, 1, 2, 0, 0, 0, 0, 2),\\ &(0, 3, 0, 0, 0, 0, 2, 0), (0, 1, 0, 0, 0, 1, 0, 0), (0, 0, 0, 2, 0, 1, 2, 0),\\ &(0, 0, 2, 0, 0, 3, 0, 0), (0, 0, 1, 0, 1, 1, 0, 0), (0, 0, 1, 0, 0, 0, 1, 0),\\ &(2, 0, 0, 1, 0, 0, 2, 0), (0, 0, 0, 1, 2, 1, 0, 0), (0, 0, 0, 1, 1, 0, 1, 0),\\ &(0, 0, 0, 1, 0, 0, 0, 1), (2, 0, 0, 0, 0, 1, 0, 0), (1, 1, 0, 0, 0, 0, 1, 0),\\ &(1, 0, 1, 0, 0, 0, 0, 1), (4, 0, 0, 0, 0, 0, 0, 1), (0, 0, 2, 0, 0, 1, 0, 1),\\ &(0, 1, 0, 1, 0, 0, 2, 0), (0, 2, 0, 0, 1, 0, 1, 0), (0, 1, 1, 0, 1, 0, 0, 1),\\ &(0, 2, 0, 0, 0, 0, 0, 1), (0, 0, 2, 0, 2, 0, 0, 1), (1, 0, 0, 1, 0, 1, 1, 0),\\ &(1, 0, 1, 0, 0, 2, 0, 0), (0, 0, 0, 1, 0, 2, 0, 0), (2, 1, 0, 0, 0, 0, 0, 1),\\ &(3, 0, 0, 0, 0, 0, 1, 0)\}.\end{aligned} \tag{A4}$$

The ordered coordinates distinguish a vector from its charge-conjugate partner. After identifying global charge conjugation and term reordering, the 34 vectors reduce to 19 inequivalent minimal zero-sum classes. Their one-to-one correspondence with the combinatorial set $\mathcal{A}(\mathcal{B}_0)$ is listed in Table II. Thus, the Hilbert-basis calculation independently reproduces the complete combinatorial enumeration in Sec. II C.

Applying the magnetic-space-group coexistence and multiplicity filters in Sec. II E, with the complete compatibility lists in Appendix C, removes the three sequences containing multiple charge-4 nodes and leaves the 16 crystallographically realizable IWMs in Eq. (9).

APPENDIX B: ENUMERATION AND EQUIVALENCE REDUCTION OF SURFACE-CONNECTIVITY CLASSES

The winding-resolved transport matrix $F_{ab}(g)$ in Eq. (31) formally allows $g = (n_x, n_y) \in \mathbb{Z}^2$, so the space of geometric realizations is infinite in the universal-cover description. The quantity to be classified, however, is the periodic connectivity on the surface torus $\Sigma \simeq \mathbb{T}^2$ modulo lattice translations and periodic identification, rather than the literal length or shape of an arc in the repeated-zone picture. For a fixed pair of projected end points a and b, an arc with winding vector g is represented by a connection from a in the central surface BZ to an image of b in a periodically translated copy of the BZ labeled by g. Under quotient-graph reduction, extra detours by whole reciprocal-lattice periods do not produce new connectivity classes; they only provide different repeated-zone representatives of the same periodic connection on $\mathbb{T}^2$. Therefore, every quotient-graph class admits a representative for which each winding component takes one of the three values,

$$n_x, n_y \in \{-1, 0, 1\}. \tag{B1}$$

Equivalently, all inequivalent periodic end point connectivities can be represented within the 3×3 repeated surface-BZ window

$$S = \{(u, v) \in \mathbb{Z}^2 \mid u, v \in \{-1, 0, 1\}\}, \quad |S| = 9. \tag{B2}$$

The 3×3 construction is thus a complete representative domain for quotient-graph classification, rather than a merely convenient visualization choice.

After restricting g to S, the admissible Fermi-arc networks are encoded by the non-negative integer variables $F_{ab}(g)$ with $g \in S$, still subject to the end point-incidence constraints in Eq. (31). For a fixed IWM, or more generally for a fixed composite Weyl-node content, these constraints define a linear Diophantine system

$$Ax = b, \tag{B3}$$

where $x = \mathrm{vec}(F)$ is the vectorized transport array and b records the prescribed outgoing and incoming multiplicities. The corresponding solution set is the integer fiber

$$\mathcal{F}_b = \{x \in \mathbb{Z}^N_{\geqslant 0} | Ax = b\}, \tag{B4}$$

with $N = m\,n\,|S|$.

We exhaustively enumerated $\mathcal{F}_b$ using the Markov-basis method implemented in `4ti2` [31,66,67]. A Markov basis provides a complete set of integer moves connecting all solutions within the same fiber while preserving the node-incidence constraints. The resulting solution list therefore contains all admissible winding-resolved transport matrices in the 3×3 representative domain.

The raw integer solutions are still redundant from the viewpoint of Fermi-arc topology. A key reason is that Weyl points in the Brillouin zone are not, in general, immovably fixed at specific momenta: Except for nodes pinned to high-symmetry points, lines, or planes by symmetry, they can move continuously in momentum space under band-structure deformations, provided that the relevant space-group (or magnetic-space-group) symmetry constraints and their chiral charges are maintained. Their surface projections therefore also admit symmetry-allowed deformations. As a result, different matrices $F_{ab}(g)$ may describe the same periodic connectivity, differing only by the geometric placement of end points rather than by the underlying topological pairing structure. Such redundancy is removed once one identifies (1) translations of the repeated-zone embedding, (2) periodic identifications of equivalent boundary-crossing segments, and (3) permutations of symmetry-equivalent projected Weyl points carrying the same charge. We therefore reduce the enumerated solution set by quotient-graph equivalence and retain only inequivalent classes. The patterns displayed in Fig. 4(a) are precisely these quotient-graph-inequivalent classes for the 16 IWMs, with their representative end point-incidence data summarized in Table I. For each IWM X_i, these inequivalent classes constitute the set $\mathcal{M}_i$ used in Eq. (28).

Reconstruction between IWM units is subsequently represented by $\Delta_{ab}(g)$, subject to the zero-marginal constraints in Eq. (30). This term changes the pairing of arc channels without changing the total incidence at any projected Weyl node.

APPENDIX C: COMPLETE MAGNETIC-SPACE-GROUP COMPATIBILITY OF THE 16 IRREDUCIBLE WEYL MOLECULES

Charge neutrality alone does not ensure crystallographic realizability, because the constituent Weyl charges must coexist within a single magnetic space group with symmetry-compatible orbit multiplicities. We therefore screened all 1651 magnetic space groups separately in the spinless and spinful regimes. The compatibility relations in Tables III–XVIII provide the crystallographic basis for reducing the 19 mathematical minimal zero-sum classes to the 16 realizable IWMs used throughout the main text.

TABLE III. $\{1,\ -1\}$.

Type	MSGs
Type-I MSGs (without SOC)	3.1, 4.7, 5.13, 10.42, 11.50, 12.58, 13.65, 14.75, 15.85, 16.1, 17.7, 18.16, 19.25, 20.31, 21.38, 22.45, 23.49, 24.53, 36.172, 71.533, 72.539, 73.548, 74.554, 75.1, 76.7, 77.13, 78.19, 79.25, 80.29, 81.33, 82.39, 83.43, 84.51, 85.59, 86.67, 87.75, 88.81, 89.87, 90.95, 91.103, 92.111, 93.119, 94.127, 95.135, 96.143, 97.151, 98.157, 111.251, 112.259, 113.267, 114.275, 115.283, 116.291, 117.299, 118.307, 119.315, 120.321, 121.327, 122.333, 143.1, 144.4, 145.7, 146.10, 147.13, 148.17, 149.21, 150.25, 151.29, 152.33, 153.37, 154.41, 155.45, 156.49, 158.57, 162.73, 163.79, 164.85, 165.91, 166.97, 167.103, 168.109, 169.113, 170.117, 171.121, 172.125, 173.129, 174.133, 175.137, 176.143, 177.149, 178.155, 179.161, 180.167, 181.173, 182.179, 187.209, 188.215, 195.1, 196.4, 197.7, 198.9, 199.12, 200.14, 201.18, 202.22, 203.26, 204.30, 205.33, 206.37, 207.40, 208.44, 209.48, 210.52, 211.56, 212.59, 213.63, 214.67
Type-I MSGs (with SOC)	3.1, 4.7, 5.13, 10.42, 11.50, 12.58, 13.65, 14.75, 15.85, 16.1, 17.7, 18.16, 19.25, 20.31, 21.38, 22.45, 23.49, 24.53, 71.533, 72.539, 73.548, 74.554, 75.1,76.7, 77.13, 78.19, 79.25, 80.29, 81.33, 82.39, 83.43, 84.51, 85.59, 86.67, 87.75, 88.81, 89.87, 90.95, 91.103, 92.111, 93.119, 94.127, 95.135, 96.143, 97.151, 98.157, 111.251, 112.259, 113.267, 114.275, 115.283, 116.291, 117.299, 118.307, 119.315, 120.321, 121.327, 122.333, 143.1, 144.4, 145.7, 146.10, 147.13, 148.17, 149.21, 150.25, 151.29, 152.33, 153.37, 154.41, 155.45, 156.49, 158.57, 162.73, 163.79, 164.85, 165.91, 166.97, 167.103, 168.109, 169.113, 170.117, 171.121, 172.125, 173.129, 174.133, 175.137, 176.143, 177.149, 178.155, 179.161, 180.167, 181.173, 182.179, 187.209, 188.215, 195.1, 196.4, 197.7, 198.9, 199.12, 200.14, 201.18, 202.22, 203.26, 204.30, 205.33, 206.37, 207.40, 208.44, 209.48, 210.52, 211.56, 212.59, 213.63, 214.67
Type-II MSGs (without SOC)	3.2, 4.8, 5.14, 16.2, 17.8, 18.17, 19.26, 20.32, 21.39, 22.46, 23.50, 24.54, 75.2, 76.8, 77.14, 78.20, 79.26, 80.30, 89.88, 90.96, 91.104, 92.112, 93.120, 94.128, 95.136, 96.144, 97.152, 98.158, 111.252, 112.260, 113.268, 114.276, 115.284, 116.292, 117.300, 118.308, 119.316, 120.322, 121.328, 122.334, 143.2, 144.5, 145.8, 146.11, 149.22, 150.26, 151.30, 152.34, 153.38, 154.42, 155.46, 156.50, 158.58, 168.110, 169.114, 170.118, 171.122, 172.126, 173.130, 174.134, 177.150, 178.156, 179.162, 180.168, 181.174, 182.180, 187.210, 188.216, 195.2, 196.5, 197.8, 198.10, 199.13, 207.41, 208.45, 209.49, 210.53, 211.57, 212.60, 213.64, 214.68
Type-II MSGs (with SOC)	1.2, 3.2, 4.8, 5.14, 8.33, 9.38, 16.2, 17.8, 18.17, 19.26, 20.32, 21.39, 22.46, 23.50, 24.54, 35.166, 36.173, 37.181, 44.230, 45.236, 46.242, 75.2, 76.8, 77.14, 78.20, 79.26, 80.30, 81.34, 82.40, 89.88, 90.96, 91.104, 92.112, 93.120, 94.128, 95.136, 96.144, 97.152, 98.158, 111.252, 112.260, 113.268, 114.276, 115.284, 116.292, 117.300, 118.308, 119.316, 120.322, 121.328, 122.334, 143.2, 144.5, 145.8, 146.11, 149.22, 150.26, 151.30, 152.34, 153.38, 154.42, 155.46, 156.50, 158.58, 168.110, 169.114, 170.118, 171.122, 172.126, 173.130, 174.134, 177.150, 178.156, 179.162, 180.168, 181.174, 182.180, 187.210, 188.216, 195.2, 196.5, 197.8, 198.10, 199.13, 207.41, 208.45, 209.49, 210.53, 211.57, 212.60, 213.64, 214.68
Type-III MSGs (without SOC)	16.3, 17.9, 17.10, 18.19, 20.33, 20.34, 21.40, 21.41, 22.47, 23.51, 24.55, 25.60, 26.70,27.81,28.91, 29.103, 30.115, 31.127, 32.138, 33.148, 34.159, 35.168, 36.176, 37.183, 38.191, 39.199, 40.207, 41.215, 42.222, 43.227, 44.232, 45.238, 46.245, 47.252, 48.260, 49.269, 49.270, 50.281, 50.282, 51.294, 51.295, 51.296, 52.310, 52.311, 52.312, 53.326, 53.327, 53.328, 54.342, 54.343, 54.344, 55.358, 56.370, 57.382, 57.384, 58.398, 59.410, 60.422, 60.423, 63.462, 63.463, 63.464, 64.474, 64.475, 64.476, 65.485, 65.486, 66.495, 66.496, 67.505, 67.506, 68.515, 68.516, 69.524, 70.530, 71.536, 72.543, 72.544, 73.551, 74.558, 74.559, 75.3, 76.9, 77.15, 78.21, 79.27, 80.31, 88.83, 89.89, 89.90, 89.91, 90.97, 90.98, 90.99, 91.105, 91.106, 91.107, 92.113, 92.114, 92.115, 93.121, 93.122, 93.123, 94.129, 94.130, 94.131, 95.137, 95.138, 95.139, 96.145, 96.146, 96.147, 97.153, 97.154, 97.155, 98.159, 98.160, 98.161, 99.167, 100.175, 101.183, 102.191, 103.199, 104.207, 105.215, 106.223, 107.231, 108.237, 109.242, 109.243, 110.248, 110.249, 111.254, 111.255, 112.262, 112.263, 113.270, 114.278, 115.285, 115.287, 116.293, 116.295, 117.301, 117.303, 118.309, 118.311, 119.317, 119.319, 120.323, 120.325, 121.330, 121.331, 122.336, 122.337, 123.345, 124.357, 125.369, 126.381, 127.393, 128.405, 129.417, 130.429, 131.441, 132.453, 133.465, 134.477, 135.489, 136.501, 137.513, 138.525, 139.535, 139.537, 140.545, 140.547, 141.555, 141.557, 142.565, 142.567, 149.23, 150.27, 151.31, 152.35, 153.39, 154.43, 155.47, 156.51, 157.55, 158.59, 159.63, 160.67, 161.71, 162.77, 163.83, 164.89, 165.95, 166.101, 167.107, 168.111, 169.115, 170.119, 171.123, 172.127, 173.131, 174.135, 175.141, 176.147, 177.151, 177.152, 177.153, 178.157, 178.158, 178.159, 179.163, 179.164, 179.165, 180.169, 180.170, 180.171, 181.175, 181.176, 181.177, 182.181, 182.182, 182.183, 183.188, 183.189, 184.194, 184.195, 185.200, 185.201, 186.206, 186.207, 187.211, 187.212, 187.213, 188.217, 188.218, 188.219, 189.224, 189.225, 190.230, 190.231, 191.238, 191.239, 191.240, 192.248, 192.249, 192.250, 193.259, 193.260, 194.269, 194.270, 207.42, 208.46, 209.50, 210.54, 211.58, 212.61, 213.65, 214.69, 215.72, 216.76, 217.80, 218.83, 219.87, 220.91, 221.95, 222.101, 223.107, 224.113, 225.119, 226.125, 227.131, 228.137, 229.143, 230.148

TABLE III. (*Continued.*)

Type	MSGs
Type-III MSGs (with SOC)	16.3, 17.9, 17.10, 18.19, 20.33, 20.34, 21.40, 21.41, 22.47, 23.51, 24.55, 25.60, 26.70, 27.81, 28.91, 29.103, 30.115, 31.127, 32.138, 33.148, 34.159, 35.168, 36.176, 37.183, 38.191, 39.199, 40.207, 41.215, 42.222, 43.227, 44.232, 45.238, 46.245, 47.252, 48.260, 49.269, 49.270, 50.281, 50.282, 51.294, 51.295, 51.296, 52.310, 52.311, 52.312, 53.326, 53.327, 53.328, 54.342, 54.343, 54.344, 55.358, 56.370, 57.382, 57.384, 58.398, 59.410, 60.422, 60.423, 63.462, 63.463, 63.464, 64.474, 64.475, 64.476, 65.485, 65.486, 66.495, 66.496, 67.505, 67.506, 68.515, 68.516, 69.524, 70.530, 71.536, 72.543, 72.544, 73.551, 74.558, 74.559, 75.3, 76.9, 77.15, 78.21, 79.27, 80.31, 87.77, 89.89, 89.90, 89.91, 90.97, 90.98, 90.99, 91.105, 91.106, 91.107, 92.113, 92.114, 92.115, 93.121, 93.122, 93.123, 94.129, 94.130, 94.131, 95.137, 95.138, 95.139, 96.145, 96.146, 96.147, 97.153, 97.154, 97.155, 98.159, 98.160, 98.161, 99.167, 100.175, 101.183, 102.191, 103.199, 104.207, 105.215, 106.223, 107.230, 107.231, 108.236, 108.237, 109.242, 109.243, 110.249, 111.254, 111.255, 112.262, 112.263, 113.270, 114.278, 115.285, 115.287, 116.293, 116.295, 117.301, 117.303, 118.309, 118.311, 119.317, 119.319, 120.323, 120.325, 121.330, 121.331, 122.336, 122.337, 123.345, 124.357, 125.369, 126.381, 127.393, 128.405, 129.417, 130.429, 131.441, 132.453, 133.465, 134.477, 135.489, 136.501, 137.513, 138.525, 139.535, 139.537, 140.545, 140.547, 141.555, 141.557, 142.565, 142.567, 149.23, 150.27, 151.31, 152.35, 153.39, 154.43, 155.47, 156.51, 157.55, 158.59, 159.63, 160.67, 161.71, 162.77, 163.83, 164.89, 165.95, 166.101, 167.107, 168.111, 169.115, 170.119, 171.123, 172.127, 173.131, 174.135, 175.141, 176.147, 177.151, 177.152, 177.153, 178.157, 178.158, 178.159, 179.163, 179.164, 179.165, 180.169, 180.170, 180.171, 181.175, 181.176, 181.177, 182.181, 182.182, 182.183, 183.188, 183.189, 184.194, 184.195, 185.200, 185.201, 186.206, 186.207, 187.211, 187.212, 187.213, 188.217, 188.218, 188.219, 189.224, 189.225, 190.230, 190.231, 191.238, 191.239, 191.240, 192.248, 192.249, 192.250, 193.259, 193.260, 194.269, 194.270, 207.42, 208.46, 209.50, 210.54, 211.58, 212.61, 213.65, 214.69, 215.72, 216.76, 217.80, 218.83, 219.87, 220.91, 221.95, 222.101, 223.107, 224.113, 225.119, 226.125, 227.131, 228.137, 229.143, 230.148
Type-IV MSGs (without SOC)	3.4, 3.5, 3.6, 4.10, 4.11, 4.12, 5.16, 5.17, 8.36, 9.41, 16.4, 16.5, 16.6, 17.11, 17.12, 17.13, 17.14, 17.15, 18.20, 18.21, 18.22, 18.23, 18.24, 19.28, 19.29, 19.30, 20.35, 20.36, 20.37, 21.42, 21.43, 21.44, 22.48, 23.52, 24.56, 35.170, 35.171, 36.177, 36.178, 36.179, 37.185, 37.186, 43.228, 44.234, 45.240, 46.247, 46.248, 75.4, 75.5, 75.6, 76.10, 76.11, 76.12, 77.16, 77.17, 77.18, 78.22, 78.23, 78.24, 79.28, 80.32, 81.36, 81.37, 81.38, 82.42, 89.92, 89.93, 89.94, 90.100, 90.101, 90.102, 91.108, 91.109, 91.110, 92.116, 92.117, 92.118, 93.124, 93.125, 93.126, 94.132, 94.133, 94.134, 95.140, 95.141, 95.142, 96.148, 96.149, 96.150, 97.156, 98.162, 111.256, 111.257, 112.264, 112.265, 113.273, 113.274, 114.281, 114.282, 115.289, 116.297, 117.305, 118.313, 119.320, 120.326, 121.332, 122.338, 143.3, 144.6, 145.9, 146.12, 149.24, 150.28, 151.32, 152.36, 153.40, 154.44, 155.48, 156.52, 158.60, 168.112, 169.116, 170.120, 171.124, 172.128, 173.132, 174.136, 177.154, 178.160, 179.166, 180.172, 181.178, 182.184, 187.214, 188.220, 195.3, 196.6, 198.11, 207.43, 208.47, 209.51, 210.55, 212.62, 213.66
Type-IV MSGs (with SOC)	1.3, 3.4, 3.5, 3.6, 4.10, 4.11, 4.12, 5.16, 5.17, 16.4, 16.5, 16.6, 17.11, 17.12, 17.13, 17.14, 17.15, 18.20, 18.21, 18.22, 18.23, 18.24, 19.28, 19.29, 19.30, 20.35, 20.36, 20.37, 21.42, 21.43, 21.44, 22.48, 23.52, 24.56, 35.169, 36.177, 36.179, 37.184, 44.233, 45.239, 46.246, 75.4, 75.5, 75.6, 76.10, 76.11, 76.12, 77.16, 77.17, 77.18, 78.22, 78.23, 78.24, 79.28, 80.32, 81.36, 82.42, 89.92, 89.93, 89.94, 90.100, 90.101, 90.102, 91.108, 91.109, 91.110, 92.116, 92.117, 92.118, 93.124, 93.125, 93.126, 94.132, 94.133, 94.134, 95.140, 95.141, 95.142, 96.148, 96.149, 96.150, 97.156, 98.162, 111.256, 111.257, 112.264, 112.265, 113.273, 113.274, 114.281, 114.282, 115.289, 116.297, 117.305, 118.313, 119.320, 120.326, 121.332, 122.338, 143.3, 144.6, 145.9, 146.12, 149.24, 150.28, 151.32, 152.36, 153.40, 154.44, 155.48, 156.52, 158.60, 168.112, 169.116, 170.120, 171.124, 172.128, 173.132, 174.136, 177.154, 178.160, 179.166, 180.172, 181.178, 182.184, 187.214, 188.220, 195.3, 196.6, 198.11, 207.43, 208.47, 209.51, 210.55, 212.62, 213.66

TABLE IV. {2, −2}.

Type	MSGs
Type-I MSGs (without SOC)	75.1, 76.7, 77.13, 78.19, 79.25, 80.29, 83.43, 84.51, 85.59, 86.67, 87.75, 88.81, 89.87, 90.95, 91.103, 92.111, 93.119, 94.127, 95.135, 96.143, 97.151, 98.157, 168.109, 169.113, 170.117, 171.121, 172.125, 173.129, 175.137, 176.143, 177.149, 178.155, 179.161, 180.167, 181.173, 182.179, 207.40, 208.44, 209.48, 210.52, 211.56, 212.59, 213.63, 214.67
Type-I MSGs (with SOC)	75.1, 76.7, 77.13, 78.19, 79.25, 80.29, 83.43, 84.51, 85.59, 86.67, 87.75, 88.81, 89.87, 90.95, 91.103, 92.111, 93.119, 94.127, 95.135, 96.143, 97.151, 98.157, 168.109, 169.113, 170.117, 171.121, 172.125, 173.129, 175.137, 176.143, 177.149, 178.155, 179.161, 180.167, 181.173, 182.179, 207.40, 208.44, 209.48, 210.52, 211.56, 212.59, 213.63, 214.67
Type-II MSGs (without SOC)	75.2, 76.8, 77.14, 78.20, 79.26, 80.30, 89.88, 90.96, 91.104, 92.112, 93.120, 94.128, 95.136, 96.144, 97.152, 98.158, 143.2, 144.5, 145.8, 146.11, 149.22, 150.26, 151.30, 152.34, 153.38, 154.42, 155.46, 168.110, 169.114, 170.118, 171.122, 172.126, 173.130, 177.150, 178.156, 179.162, 180.168, 181.174, 182.180, 196.5, 207.41, 208.45, 209.49, 210.53, 211.57, 212.60, 213.64, 214.68
Type-II MSGs (with SOC)	75.2, 76.8, 77.14, 78.20, 79.26, 80.30, 89.88, 90.96, 91.104, 92.112, 93.120, 94.128, 95.136, 96.144, 97.152, 98.158, 168.110, 169.114, 170.118, 171.122, 172.126, 173.130, 177.150, 178.156, 179.162, 180.168, 181.174, 182.180, 207.41, 208.45, 209.49, 210.53, 211.57, 212.60, 213.64, 214.68
Type-III MSGs (without SOC)	75.3, 76.9, 77.15, 78.21, 79.27, 80.31, 87.77, 89.89, 89.90, 89.91, 90.97, 90.98, 90.99, 91.105, 91.106, 91.107, 92.113, 92.114, 92.115, 93.121, 93.122, 93.123, 94.129, 94.130, 94.131, 95.137, 95.138, 95.139, 96.145, 96.146, 96.147, 97.153, 97.154, 97.155, 98.159, 98.160, 98.161, 99.167, 100.175, 101.183, 102.191, 103.199, 104.207, 105.215, 106.223, 107.230, 107.231, 108.236, 108.237, 109.243, 110.249, 123.345, 124.357, 125.369, 126.381, 127.393, 128.405, 129.417, 130.429, 131.441, 132.453, 133.465, 134.477, 135.489, 136.501, 137.513, 138.525, 139.535, 139.537, 140.545, 140.547, 141.557, 142.567, 177.153, 178.159, 179.165, 180.171, 181.177, 182.183, 183.189, 184.195, 185.201, 186.207, 191.240, 192.250, 193.260, 194.270, 207.42, 208.46, 209.50, 210.54, 212.61, 213.65
Type-III MSGs (with SOC)	76.9, 78.21, 80.31, 88.83, 89.90, 90.98, 91.105, 91.106, 91.107, 92.113, 92.114, 92.115, 93.122, 94.130, 95.137, 95.138, 95.139, 96.145, 96.146, 96.147, 97.154, 98.159, 98.160, 98.161, 99.167, 100.175, 101.183, 102.191, 103.199, 104.207, 105.215, 106.223, 107.231, 108.237, 109.242, 109.243, 110.248, 110.249, 123.345, 124.357, 125.369, 126.381, 127.393, 128.405, 129.417, 130.429, 131.441, 132.453, 133.465, 134.477, 135.489, 136.501, 137.513, 138.525, 139.537, 140.547, 141.555, 141.557, 142.565, 142.567, 177.153, 178.159, 179.165, 180.171, 181.177, 182.183, 183.189, 184.195, 185.201, 186.207, 191.240, 192.250, 193.260, 194.270, 210.54, 212.61, 213.65
Type-IV MSGs (without SOC)	75.4, 75.5, 75.6, 76.10, 76.11, 76.12, 77.16, 77.17, 77.18, 78.22, 78.23, 78.24, 79.28, 80.32, 89.92, 89.93, 89.94, 90.100, 90.101, 90.102, 91.108, 91.109, 91.110, 92.116, 92.117, 92.118, 93.124, 93.125, 93.126, 94.132, 94.133, 94.134, 95.140, 95.141, 95.142, 96.148, 96.149, 96.150, 97.156, 98.162, 168.112, 169.116, 170.120, 171.124, 172.128, 173.132, 177.154, 178.160, 179.166, 180.172, 181.178, 182.184, 207.43, 208.47, 209.51, 210.55, 212.62, 213.66
Type-IV MSGs (with SOC)	75.4, 75.5, 75.6, 76.10, 76.11, 76.12, 77.16, 77.17, 77.18, 78.22, 78.23, 78.24, 79.28, 80.32, 89.92, 89.93, 89.94, 90.100, 90.101, 90.102, 91.108, 91.109, 91.110, 92.116, 92.117, 92.118, 93.124, 93.125, 93.126, 94.132, 94.133, 94.134, 95.140, 95.141, 95.142, 96.148, 96.149, 96.150, 97.156, 98.162, 168.112, 169.116, 170.120, 171.124, 172.128, 173.132, 177.154, 178.160, 179.166, 180.172, 181.178, 182.184, 196.6, 207.43, 208.47, 209.51, 210.55, 212.62, 213.66

TABLE V. {3, −3}.

Type	MSGs
Type-I MSGs (without SOC)	168.109, 169.113, 170.117, 171.121, 172.125, 173.129, 175.137, 176.143, 177.149, 178.155, 179.161, 180.167, 181.173, 182.179
Type-I MSGs (with SOC)	168.109, 169.113, 170.117, 171.121, 172.125, 173.129, 175.137, 176.143, 177.149, 178.155, 179.161, 180.167, 181.173, 182.179
Type-II MSGs (without SOC)	168.110, 169.114, 170.118, 171.122, 172.126, 173.130, 177.150, 178.156, 179.162, 180.168, 181.174, 182.180
Type-II MSGs (with SOC)	143.2, 144.5, 145.8, 146.11, 149.22, 150.26, 151.30, 152.34, 153.38, 154.42, 155.46, 168.110, 169.114, 170.118, 171.122, 172.126, 173.130, 177.150, 178.156, 179.162, 180.168, 181.174, 182.180, 196.5, 209.49, 210.53
Type-III MSGs (without SOC)	177.153, 178.159, 179.165, 180.171, 181.177, 182.183, 183.189, 184.195, 185.201, 186.207, 191.240, 192.250, 193.260, 194.270
Type-III MSGs (with SOC)	177.153, 178.159, 179.165, 180.171, 181.177, 182.183, 183.189, 184.195, 185.201, 186.207, 191.240, 192.250, 193.260, 194.270
Type-IV MSGs (without SOC)	168.112, 169.116, 170.120, 171.124, 172.128, 173.132, 177.154, 178.160, 179.166, 180.172, 181.178, 182.184, 196.6, 209.51, 210.55
Type-IV MSGs (with SOC)	168.112, 169.116, 170.120, 171.124, 172.128, 173.132, 177.154, 178.160, 179.166, 180.172, 181.178, 182.184

TABLE VI. {4, −4}.

Type	MSGs
Type-I MSGs (without SOC)	207.40, 208.44, 211.56, 214.67
Type-I MSGs (with SOC)	
Type-II MSGs (without SOC)	195.2, 197.8, 199.13, 207.41, 208.45, 211.57, 214.68
Type-II MSGs (with SOC)	
Type-III MSGs (without SOC)	
Type-III MSGs (with SOC)	
Type-IV MSGs (without SOC)	
Type-IV MSGs (with SOC)	

TABLE VII. {2, −1, −1}.

Type	MSGs
Type-I MSGs (without SOC)	75.1, 76.7, 77.13, 78.19, 79.25, 80.29, 83.43, 84.51, 85.59, 86.67, 87.75, 88.81, 89.87, 90.95, 91.103, 92.111, 93.119, 94.127, 95.135, 96.143, 97.151, 98.157, 168.109, 169.113, 170.117, 171.121, 172.125, 173.129, 175.137, 176.143, 177.149, 178.155, 179.161, 180.167, 181.173, 182.179, 207.40, 208.44, 209.48, 210.52, 211.56, 212.59, 213.63, 214.67
Type-I MSGs (with SOC)	75.1, 76.7, 77.13, 78.19, 79.25, 80.29, 83.43, 84.51, 85.59, 86.67, 87.75, 88.81, 89.87, 90.95, 91.103, 92.111, 93.119, 94.127, 95.135, 96.143, 97.151, 98.157, 168.109, 169.113, 170.117, 171.121, 172.125, 173.129, 175.137, 176.143, 177.149, 178.155, 179.161, 180.167, 181.173, 182.179, 207.40, 208.44, 209.48, 210.52, 211.56, 212.59, 213.63, 214.67
Type-II MSGs (without SOC)	75.2, 76.8, 77.14, 78.20, 79.26, 80.30, 89.88, 90.96, 91.104, 92.112, 93.120, 94.128, 95.136, 96.144, 97.152, 98.158, 143.2, 144.5, 145.8, 146.11, 149.22, 150.26, 151.30, 152.34, 153.38, 154.42, 155.46, 168.110, 169.114, 170.118, 171.122, 172.126, 173.130, 177.150, 178.156, 179.162, 180.168, 181.174, 182.180, 196.5, 207.41, 208.45, 209.49, 210.53, 211.57, 212.60, 213.64, 214.68
Type-II MSGs (with SOC)	75.2, 76.8, 77.14, 78.20, 79.26, 80.30, 89.88, 90.96, 91.104, 92.112, 93.120, 94.128, 95.136, 96.144, 97.152, 98.158, 168.110, 169.114, 170.118, 171.122, 172.126, 173.130, 177.150, 178.156, 179.162, 180.168, 181.174, 182.180, 207.41, 208.45, 209.49, 210.53, 211.57, 212.60, 213.64, 214.68
Type-III MSGs (without SOC)	75.3, 76.9, 77.15, 78.21, 79.27, 80.31, 87.77, 89.89, 89.90, 89.91, 90.97, 90.98, 90.99, 91.105, 91.106, 91.107, 92.113, 92.114, 92.115, 93.121, 93.122, 93.123, 94.129, 94.130, 94.131, 95.137, 95.138, 95.139, 96.145, 96.146, 96.147, 97.153, 97.154, 97.155, 98.159, 98.160, 98.161, 99.167, 100.175, 101.183, 102.191, 103.199, 104.207, 105.215, 106.223, 107.230, 107.231, 108.236, 108.237, 109.243, 110.249, 123.345, 124.357, 125.369, 126.381, 127.393, 128.405, 129.417, 130.429, 131.441, 132.453, 133.465, 134.477, 135.489, 136.501, 137.513, 138.525, 139.535, 139.537, 140.545, 140.547, 141.557, 142.567, 177.153, 178.159, 179.165, 180.171, 181.177, 182.183, 183.189, 184.195, 185.201, 186.207, 191.240, 192.250, 193.260, 194.270, 207.42, 208.46, 209.50, 210.54, 212.61, 213.65
Type-III MSGs (with SOC)	76.9, 78.21, 80.31, 88.83, 89.90, 90.98, 91.105, 91.106, 91.107, 92.113, 92.114, 92.115, 93.122, 94.130, 95.137, 95.138, 95.139, 96.145, 96.146, 96.147, 97.154, 98.159, 98.160, 98.161, 99.167, 100.175, 101.183, 102.191, 103.199, 104.207, 105.215, 106.223, 107.231, 108.237, 109.242, 109.243, 110.248, 110.249, 123.345, 124.357, 125.369, 126.381, 127.393, 128.405, 129.417, 130.429, 131.441, 132.453, 133.465, 134.477, 135.489, 136.501, 137.513, 138.525, 139.537, 140.547, 141.555, 141.557, 142.565, 142.567, 177.153, 178.159, 179.165, 180.171, 181.177, 182.183, 183.189, 184.195, 185.201, 186.207, 191.240, 192.250, 193.260, 194.270, 210.54, 212.61, 213.65
Type-IV MSGs (without SOC)	75.4, 75.5, 75.6, 76.10, 76.11, 76.12, 77.16, 77.17, 77.18, 78.22, 78.23, 78.24, 79.28, 80.32, 89.92, 89.93, 89.94, 90.100, 90.101, 90.102, 91.108, 91.109, 91.110, 92.116, 92.117, 92.118, 93.124, 93.125, 93.126, 94.132, 94.133, 94.134, 95.140, 95.141, 95.142, 96.148, 96.149, 96.150, 97.156, 98.162, 143.3, 144.6, 145.9, 146.12, 149.24, 150.28, 151.32, 152.36, 153.40, 154.44, 155.48, 168.112, 169.116, 170.120, 171.124, 172.128, 173.132, 177.154, 178.160, 179.166, 180.172, 181.178, 182.184, 207.43, 208.47, 209.51, 210.55, 212.62, 213.66
Type-IV MSGs (with SOC)	75.4, 75.5, 75.6, 76.10, 76.11, 76.12, 77.16, 77.17, 77.18, 78.22, 78.23, 78.24, 79.28, 80.32, 89.92, 89.93, 89.94, 90.100, 90.101, 90.102, 91.108, 91.109, 91.110, 92.116, 92.117, 92.118, 93.124, 93.125, 93.126, 94.132, 94.133, 94.134, 95.140, 95.141, 95.142, 96.148, 96.149, 96.150, 97.156, 98.162, 143.3, 144.6, 145.9, 146.12, 149.24, 150.28, 151.32, 152.36, 153.40, 154.44, 155.48, 168.112, 169.116, 170.120, 171.124, 172.128, 173.132, 177.154, 178.160, 179.166, 180.172, 181.178, 182.184, 196.6, 207.43, 208.47, 209.51, 210.55, 212.62, 213.66

TABLE VIII. $\{3, -2, -1\}$.

Type	MSGs
Type-I MSGs (without SOC)	168.109, 169.113, 170.117, 171.121, 172.125, 173.129, 175.137, 176.143, 177.149, 178.155, 179.161, 180.167, 181.173, 182.179
Type-I MSGs (with SOC)	168.109, 169.113, 170.117, 171.121, 172.125, 173.129, 175.137, 176.143, 177.149, 178.155, 179.161, 180.167, 181.173, 182.179
Type-II MSGs (without SOC)	168.110, 169.114, 170.118, 171.122, 172.126, 173.130, 177.150, 178.156, 179.162, 180.168, 181.174, 182.180
Type-II MSGs (with SOC)	168.110, 169.114, 170.118, 171.122, 172.126, 173.130, 177.150, 178.156, 179.162, 180.168, 181.174, 182.180, 209.49, 210.53
Type-III MSGs (without SOC)	177.153, 178.159, 179.165, 180.171, 181.177, 182.183, 183.189, 184.195, 185.201, 186.207, 191.240, 192.250, 193.260, 194.270
Type-III MSGs (with SOC)	177.153, 178.159, 179.165, 180.171, 181.177, 182.183, 183.189, 184.195, 185.201, 186.207, 191.240, 192.250, 193.260, 194.270
Type-IV MSGs (without SOC)	143.3, 144.6, 145.9, 146.12, 149.24, 150.28, 151.32, 152.36, 153.40, 154.44, 155.48, 168.112, 169.116, 170.120, 171.124, 172.128, 173.132, 177.154, 178.160, 179.166, 180.172, 181.178, 182.184, 209.51, 210.55
Type-IV MSGs (with SOC)	143.3, 144.6, 145.9, 146.12, 149.24, 150.28, 151.32, 152.36, 153.40, 154.44, 155.48, 168.112, 169.116, 170.120, 171.124, 172.128, 173.132, 177.154, 178.160, 179.166, 180.172, 181.178, 182.184

TABLE IX. $\{4, -2, -2\}$.

Type	MSGs
Type-I MSGs (without SOC)	207.40, 208.44, 209.48, 210.52, 211.56, 212.59, 213.63, 214.67
Type-I MSGs (with SOC)	212.59, 213.63
Type-II MSGs (without SOC)	196.5, 207.41, 208.45, 209.49, 210.53, 211.57, 212.60, 213.64, 214.68
Type-II MSGs (with SOC)	
Type-III MSGs (without SOC)	
Type-III MSGs (with SOC)	
Type-IV MSGs (without SOC)	207.43, 208.47, 209.51, 210.55, 212.62, 213.66
Type-IV MSGs (with SOC)	212.62, 213.66

TABLE X. $\{4, -3, -1\}$.

Type	MSGs
Type-I MSGs (without SOC)	
Type-I MSGs (with SOC)	
Type-II MSGs (without SOC)	
Type-II MSGs (with SOC)	
Type-III MSGs (without SOC)	
Type-III MSGs (with SOC)	
Type-IV MSGs (without SOC)	196.6, 209.51, 210.55
Type-IV MSGs (with SOC)	

TABLE XI. $\{3, -1, -1, -1\}$.

Type	MSGs
Type-I MSGs (without SOC)	168.109, 169.113, 170.117, 171.121, 172.125, 173.129, 175.137, 176.143, 177.149, 178.155, 179.161, 180.167, 181.173, 182.179
Type-I MSGs (with SOC)	168.109, 169.113, 170.117, 171.121, 172.125, 173.129, 175.137, 176.143, 177.149, 178.155, 179.161, 180.167, 181.173, 182.179
Type-II MSGs (without SOC)	168.110, 169.114, 170.118, 171.122, 172.126, 173.130, 177.150, 178.156, 179.162, 180.168, 181.174, 182.180
Type-II MSGs (with SOC)	143.2, 144.5, 145.8, 146.11, 149.22, 150.26, 151.30, 152.34, 153.38, 154.42, 155.46, 168.110, 169.114, 170.118, 171.122, 172.126, 173.130, 177.150, 178.156, 179.162, 180.168, 181.174, 182.180, 196.5, 209.49, 210.53
Type-III MSGs (without SOC)	177.153, 178.159, 179.165, 180.171, 181.177, 182.183, 183.189, 184.195, 185.201, 186.207, 191.240, 192.250, 193.260, 194.270
Type-III MSGs (with SOC)	177.153, 178.159, 179.165, 180.171, 181.177, 182.183, 183.189, 184.195, 185.201, 186.207, 191.240, 192.250, 193.260, 194.270
Type-IV MSGs (without SOC)	143.3, 144.6, 145.9, 146.12, 149.24, 150.28, 151.32, 152.36, 153.40, 154.44, 155.48, 168.112, 169.116, 170.120, 171.124, 172.128, 173.132, 177.154, 178.160, 179.166, 180.172, 181.178, 182.184, 196.6, 209.51, 210.55
Type-IV MSGs (with SOC)	143.3, 144.6, 145.9, 146.12, 149.24, 150.28, 151.32, 152.36, 153.40, 154.44, 155.48, 168.112, 169.116, 170.120, 171.124, 172.128, 173.132, 177.154, 178.160, 179.166, 180.172, 181.178, 182.184

TABLE XII. {3, 1, −2, −2}.

Type	MSGs
Type-I MSGs (without SOC)	168.109, 169.113, 170.117, 171.121, 172.125, 173.129, 175.137, 176.143, 177.149, 178.155, 179.161, 180.167, 181.173, 182.179
Type-I MSGs (with SOC)	168.109, 169.113, 170.117, 171.121, 172.125, 173.129, 175.137, 176.143, 177.149, 178.155, 179.161, 180.167, 181.173, 182.179
Type-II MSGs (without SOC)	168.110, 169.114, 170.118, 171.122, 172.126, 173.130, 177.150, 178.156, 179.162, 180.168, 181.174, 182.180
Type-II MSGs (with SOC)	168.110, 169.114, 170.118, 171.122, 172.126, 173.130, 177.150, 178.156, 179.162, 180.168, 181.174, 182.180, 209.49, 210.53
Type-III MSGs (without SOC)	177.153, 178.159, 179.165, 180.171, 181.177, 182.183, 183.189, 184.195, 185.201, 186.207, 191.240, 192.250, 193.260, 194.270
Type-III MSGs (with SOC)	177.153, 178.159, 179.165, 180.171, 181.177, 182.183, 183.189, 184.195, 185.201, 186.207, 191.240, 192.250, 193.260, 194.270
Type-IV MSGs (without SOC)	168.112, 169.116, 170.120, 171.124, 172.128, 173.132, 177.154, 178.160, 179.166, 180.172, 181.178, 182.184, 209.51, 210.55
Type-IV MSGs (with SOC)	168.112, 169.116, 170.120, 171.124, 172.128, 173.132, 177.154, 178.160, 179.166, 180.172, 181.178, 182.184

TABLE XIII. {4, −2, −1, −1}.

Type	MSGs
Type-I MSGs (without SOC)	207.40, 208.44, 209.48, 210.52, 211.56, 212.59, 213.63, 214.67
Type-I MSGs (with SOC)	212.59, 213.63
Type-II MSGs (without SOC)	196.5, 207.41, 208.45, 209.49, 210.53, 211.57, 212.60, 213.64, 214.68
Type-II MSGs (with SOC)	
Type-III MSGs (without SOC)	
Type-III MSGs (with SOC)	
Type-IV MSGs (without SOC)	207.43, 208.47, 209.51, 210.55, 212.62, 213.66
Type-IV MSGs (with SOC)	212.62, 213.66

TABLE XIV. {4, 1, −3, −2}.

Type	MSGs
Type-I MSGs (without SOC)	
Type-I MSGs (with SOC)	
Type-II MSGs (without SOC)	
Type-II MSGs (with SOC)	
Type-III MSGs (without SOC)	
Type-III MSGs (with SOC)	
Type-IV MSGs (without SOC)	209.51, 210.55
Type-IV MSGs (with SOC)	

TABLE XV. {4, 2, −3, −3}.

Type	MSGs
Type-I MSGs (without SOC)	
Type-I MSGs (with SOC)	
Type-II MSGs (without SOC)	
Type-II MSGs (with SOC)	
Type-III MSGs (without SOC)	
Type-III MSGs (with SOC)	
Type-IV MSGs (without SOC)	209.51, 210.55
Type-IV MSGs (with SOC)	

TABLE XVI. {3, 3, −2, −2, −2}.

Type	MSGs
Type-I MSGs (without SOC)	168.109, 169.113, 170.117, 171.121, 172.125, 173.129, 175.137, 176.143, 177.149, 178.155, 179.161, 180.167, 181.173, 182.179
Type-I MSGs (with SOC)	168.109, 169.113, 170.117, 171.121, 172.125, 173.129, 175.137, 176.143, 177.149, 178.155, 179.161, 180.167, 181.173, 182.179
Type-II MSGs (without SOC)	168.110, 169.114, 170.118, 171.122, 172.126, 173.130, 177.150, 178.156, 179.162, 180.168, 181.174, 182.180
Type-II MSGs (with SOC)	168.110, 169.114, 170.118, 171.122, 172.126, 173.130, 177.150, 178.156, 179.162, 180.168, 181.174, 182.180, 209.49, 210.53
Type-III MSGs (without SOC)	177.153, 178.159, 179.165, 180.171, 181.177, 182.183, 183.189, 184.195, 185.201, 186.207, 191.240, 192.250, 193.260, 194.270
Type-III MSGs (with SOC)	177.153, 178.159, 179.165, 180.171, 181.177, 182.183, 183.189, 184.195, 185.201, 186.207, 191.240, 192.250, 193.260, 194.270
Type-IV MSGs (without SOC)	168.112, 169.116, 170.120, 171.124, 172.128, 173.132, 177.154, 178.160, 179.166, 180.172, 181.178, 182.184, 209.51, 210.55
Type-IV MSGs (with SOC)	168.112, 169.116, 170.120, 171.124, 172.128, 173.132, 177.154, 178.160, 179.166, 180.172, 181.178, 182.184

TABLE XVII. {4, −1, −1, −1, −1}.

Type	MSGs
Type-I MSGs (without SOC)	207.40, 208.44, 209.48, 210.52, 211.56, 212.59, 213.63, 214.67
Type-I MSGs (with SOC)	212.59, 213.63
Type-II MSGs (without SOC)	195.2, 196.5, 197.8, 198.10, 199.13, 207.41, 208.45, 209.49, 210.53, 211.57, 212.60, 213.64, 214.68
Type-II MSGs (with SOC)	
Type-III MSGs (without SOC)	
Type-III MSGs (with SOC)	
Type-IV MSGs (without SOC)	195.3, 196.6, 198.11, 207.43, 208.47, 209.51, 210.55, 212.62, 213.66
Type-IV MSGs (with SOC)	198.11, 212.62, 213.66

TABLE XVIII. {4, 1, 1, −3, −3}.

Type	MSGs
Type-I MSGs (without SOC)	
Type-I MSGs (with SOC)	
Type-II MSGs (without SOC)	
Type-II MSGs (with SOC)	
Type-III MSGs (without SOC)	
Type-III MSGs (with SOC)	
Type-IV MSGs (without SOC)	196.6, 209.51, 210.55
Type-IV MSGs (with SOC)	

APPENDIX D: CLASSIFICATION OF REPRESENTATIVE ELECTRONIC AND BOSONIC CHIRAL SYSTEMS

Because the IWM construction depends on the global organization of chiral charges, it applies to both electronic and bosonic band structures. Representative Weyl and chiral multifold semimetals and chiral phonon systems decompose into non-negative integer combinations drawn from the same IWM family (Tables XIX and XX). The occurrence of repeated elementary units and hybrid higher-charge combinations illustrates the applicability of the linear-combination principle across distinct microscopic platforms.

TABLE XIX. Classification of representative Weyl and chiral multifold semimetals into linear combinations of the 16 IWMs. An asterisk denotes a material for which the listed Weyl phase is induced by magnetism or applied strain.

Weyl and chiral multifold semimetals	IWMs
$(CdO)_n/(EuO)_m$ [68]	$\{1,-1\}$
Cs_2Tl_3 [69]	$\{1,-1\}$
$EuCd_2As_2$* [70,71]	$\{1,-1\}$
GdBi [72]	$\{1,-1\}$
GdSb [72]	$\{1,-1\}$
$Hg_{1-x-y}Cd_xMn_yTe$ [73]	$\{1,-1\}$
$HgCr_2Se_{3.5}Te_{0.5}$ [74]	$\{1,-1\}$
$MnBi_2Te_4$* [75]	$\{1,-1\}$
$MnSn_2Sb_2Te_6$ [76]	$\{1,-1\}$
KCrTe [77]	$\{1,-1\}$
$K_2Mn_3(AsO_4)_3$ [78]	$\{1,-1\}$
RbCrTe [77]	$\{1,-1\}$
$Sn_{1-x}Cr_xTe$ [79]	$\{1,-1\}$
UNiSn* [80]	$\{1,-1\}$
$(PbSe)_{1-x}(SnSe)_x$ [81]	$2\times\{1,-1\}$
$BAsO_4$ [82]	$2\times\{1,-1\}$
fco-C_6 [83]	$2\times\{1,-1\}$
Rb_3Bi [84]	$2\times\{1,-1\}$
$TaIrTe_4$ [85]	$2\times\{1,-1\}$
Te* [86]	$2\times\{1,-1\}$
WTeS [87]	$2\times\{1,-1\}$
WTeSe [87]	$2\times\{1,-1\}$
β-Ag_2Se [88]	$2\times\{1,-1\}$
β-Bi_4I_4* [89]	$2\times\{1,-1\}$
$Co_3Sn_2S_2$ [90]	$3\times\{1,-1\}$
GdB_4 [91]	$3\times\{1,-1\}$
Hf_3Sb [69]	$3\times\{1,-1\}$
$TlBi(S_{1-x}Se_x)_2$ [92]	$3\times\{1,-1\}$
$TlBi(S_{1-x}Te_x)_2$ [92]	$3\times\{1,-1\}$
Ag_2S [93]	$4\times\{1,-1\}$
$AgTlTe_2$ [94]	$4\times\{1,-1\}$
$AuTlTe_2$ [94]	$4\times\{1,-1\}$
$CaOs_2O_4$ [95]	$4\times\{1,-1\}$
$CuTlSe_2$ [94]	$4\times\{1,-1\}$
$CuTlTe_2$ [94]	$4\times\{1,-1\}$
HgTe/CdTe multilayer [96]	$4\times\{1,-1\}$
$HgTe_xS_{1-x}$ [97]	$4\times\{1,-1\}$
$Hg_xCd_{1-x}Te$ [98]	$4\times\{1,-1\}$
MoP_2 [99]	$4\times\{1,-1\}$
$MoTe_2$ [100]	$4\times\{1,-1\}$
$Mo_xW_{1-x}Te_2$ [101]	$4\times\{1,-1\}$
$SrOs_2O_4$ [95]	$4\times\{1,-1\}$

TABLE XIX. (*Continued.*)

Weyl and chiral multifold semimetals	IWMs
Ta_3S_2 [102]	$4 \times \{1, -1\}$
WP_2 [99]	$4 \times \{1, -1\}$
WTe_2 [103]	$4 \times \{1, -1\}$
$YbMnBi_2$ [104]	$4 \times \{1, -1\}$
$ZnPbAs_2$ [94]	$4 \times \{1, -1\}$
$ZnPbSb_2$ [94]	$4 \times \{1, -1\}$
CrO_2(p-CrO_2) [105]	$5 \times \{1, -1\}$
$Bi_{0.5}Sb_{0.5}$ [106]	$6 \times \{1, -1\}$
BiTeI* [107]	$6 \times \{1, -1\}$
CaAuBi* [108]	$6 \times \{1, -1\}$
$CaGe_2$ [109]	$6 \times \{1, -1\}$
CaHgSn [108]	$6 \times \{1, -1\}$
CrO_2(o-CrO_2) [105]	$6 \times \{1, -1\}$
HfS [110]	$6 \times \{1, -1\}$
HfSe [110]	$6 \times \{1, -1\}$
HfTe [110]	$6 \times \{1, -1\}$
$InNbSe_2$ [111]	$6 \times \{1, -1\}$
$K(Au_{0.5}Hg_{0.5})(Te_{0.5}As_{0.5})$ [112]	$6 \times \{1, -1\}$
$LaBi_{1-x}Sb_xTe_3$ [107]	$6 \times \{1, -1\}$
$LuBi_{1-x}Sb_xTe_3$ [107]	$6 \times \{1, -1\}$
Mn_3Ge [113]	$6 \times \{1, -1\}$
Mn_3Sn [114]	$6 \times \{1, -1\}$
$MnNb_3S_6$ [115]	$6 \times \{1, -1\}$
$MnNb_3Se_6$ [115]	$6 \times \{1, -1\}$
$MnTa_3S_6$ [115]	$6 \times \{1, -1\}$
$MnTa_3Se_6$ [115]	$6 \times \{1, -1\}$
Ni_3S_3 [116]	$6 \times \{1, -1\}$
Ni_3Se_3 [116]	$6 \times \{1, -1\}$
SrHgPb [108]	$6 \times \{1, -1\}$
SrHgSn [108]	$6 \times \{1, -1\}$
TaS [117]	$6 \times \{1, -1\}$
TiSe [110]	$6 \times \{1, -1\}$
TiTe [110]	$6 \times \{1, -1\}$
VNb_3S_6 [115]	$6 \times \{1, -1\}$
VNb_3Se_6 [115]	$6 \times \{1, -1\}$
VTa_3S_6 [115]	$6 \times \{1, -1\}$
VTa_3Se_6 [115]	$6 \times \{1, -1\}$
ZrS [110]	$6 \times \{1, -1\}$
ZrSe [110]	$6 \times \{1, -1\}$
ZrTe [110]	$6 \times \{1, -1\}$
$CaSn_3$ [118]	$8 \times \{1, -1\}$
$CeRu_4Sn_6$ [119]	$8 \times \{1, -1\}$
$NbIrTe_4$ [120]	$8 \times \{1, -1\}$
CrO_2(r-CrO_2) [105]	$12 \times \{1, -1\}$
CuF [121]	$12 \times \{1, -1\}$
FeRhCrGe [122]	$12 \times \{1, -1\}$
HfRuP [123]	$12 \times \{1, -1\}$
$InMnTi_2$ [116]	$12 \times \{1, -1\}$
Mo_2SeS [124]	$12 \times \{1, -1\}$
Mo_2TeS [124]	$12 \times \{1, -1\}$
Mo_2TeSe [124]	$12 \times \{1, -1\}$
NbAs [5]	$12 \times \{1, -1\}$
NbP [5]	$12 \times \{1, -1\}$
TaAs [5]	$12 \times \{1, -1\}$
TaP [5]	$12 \times \{1, -1\}$
W_2SeS [125]	$12 \times \{1, -1\}$

TABLE XIX. (*Continued.*)

Weyl and chiral multifold semimetals	IWMs
W_2SeTe [125]	$12 \times \{1, -1\}$
W_2SSe [125]	$12 \times \{1, -1\}$
W_2STe [125]	$12 \times \{1, -1\}$
W_2TeS [125]	$12 \times \{1, -1\}$
W_2TeSe [125]	$12 \times \{1, -1\}$
$Y_2Ir_2O_7$ [1]	$12 \times \{1, -1\}$
YPtP [126]	$12 \times \{1, -1\}$
CeAlGe [127]	$20 \times \{1, -1\}$
PrAlGe [127]	$20 \times \{1, -1\}$
LaAlGe [128]	$20 \times \{1, -1\}$
$SrSi_2$ [129]	$30 \times \{1, -1\}$
RhSi [52]	$\{2, -2\}$
RhSn [130]	$\{2, -2\}$
LiC_2 [131]	$\{2, -2\}$
$BaNiIO_6$ [132]	$\{2, -2\}$
$CaKFe_4As_4$ [133]	$\{2, -2\}$
$Pb_9Cu(PO_4)_6O$ [134]	$\{2, -2\}$
$HgCr_2Se_4$ [135]	$\{2, -2\}$
K_2RhF_6 [136]	$2 \times \{2, -2\}$
Rb_2RhF_6 [136]	$2 \times \{2, -2\}$
Cs_2RhF_6 [136]	$2 \times \{2, -2\}$
$CaGe_2$ [109]	$6 \times \{2, -2\}$
AlPt [56]	$\{4, -4\}$
ReO_3 [137]	$4 \times \{1, -1\} + 2 \times \{2, -2\} + 2 \times \{2, -1, -1\}$
$(TaSe_4)_2I$ [138]	$4 \times \{1, -1\} + 4 \times \{2, -1, -1\}$
$SrRuO_3$ [139]	$16 \times \{1, -1\} + 4 \times \{2, -1, -1\}$
BaIrP [17]	$6 \times \{2, -1, -1\} + \{4, -2, -2\}$
Li_2CO_4 [16]	$2 \times \{3, -1, -1, -1\}$
$BaNiIO_6$ [140]	$2 \times \{3, -1, -1, -1\}$
La_3AlCrS_7 [141]	$2 \times \{3, -1, -1, -1\}$
$SrNiIO_6$ [142]	$2 \times \{3, -1, -1, -1\}$
cP-C24 [143]	$8 \times \{1, -1\} + \{4, -1, -1, -1, -1\}$

TABLE XX. Classification of representative chiral phonon materials in terms of linear combinations of the 16 IWMs.

Chiral phonon materials	IWMs
$LaRhC_2$ [144]	$\{2, -2\}$
BeH_2 [61]	$\{4, -4\}$
$BaZnO_2$ [59]	$\{2, -1, -1\}$
α-SiO_2 [145]	$\{2, -1, -1\}$
$SrSi_2$ [146]	$6 \times \{2, -1, -1\}$
$CsBe_2F_5$ [147]	$12 \times \{1, -1\} + 6 \times \{2, -1, -1\}$
$LiIO_3$ [14]	$2 \times \{3, -1, -1, -1\}$
α-$LiIO_3$ [15]	$2 \times \{3, -1, -1, -1\}$
BiIrSe [60]	$8 \times \{1, -1\} + \{4, -1, -1, -1, -1\}$

APPENDIX E: STRUCTURAL, ELASTIC, ENERGETIC, AND WEYL-NODE DATA

Quantitative comparison of the five predicted boron allotropes requires their structural, mechanical, energetic, and topological properties to be considered together. The TQV-B24 and THC-B24 enantiomeric pairs have closely matched lattice, energetic, and elastic properties (Tables XXI and XXII), whereas their Weyl-node chiralities reverse with handedness (Table XXIII). The elastic tensors satisfy the listed mechanical-stability criteria, and the tabulated node coordinates, energies, charges, and multiplicities define the bulk configurations analyzed in Sec. V.

TABLE XXI. Structural parameters, densities, bulk moduli, and calculated total energies of the predicted and reference boron phases.

Structures		Space group	Lattice parameters (Å) a	b	c	Angles (deg) α	β	γ	Wyckoff positions x	y	z	Density (g/cm^3)	Bulk modulus (GPa)	E_{tot} (eV/B)
H-$P6_3$-B_{36}	B1(6c)	$P6_3$	7.40	7.40	5.73	90	90	120	0.1566	0.0668	0.3627	2.38	187	−6.36
	B2(6c)								0.0583	0.4645	0.6658			
	B3(6c)								0.0946	0.2566	0.5800			
	B4(6c)								0.2587	0.3963	0.0091			
	B5(6c)								0.5183	0.2149	0.0208			
	B6(6c)								0.9255	0.5289	0.4676			
l-TQV-B_{24}	B1(4a)	$P4_3$	6.19	6.19	4.36	90	90	90	0.0672	0.8427	0.2594	2.58	184	−6.27
	B2(4a)								0.5475	0.3593	0.2887			
	B3(4a)								0.2546	0.7242	0.5549			
	B4(4a)								0.8644	0.4377	0.7740			
	B5(4a)								0.6700	0.0153	0.8919			
	B6(4a)								0.8201	0.2731	0.4339			
r-TQV-B_{24}	B1(4a)	$P4_1$	6.19	6.19	4.36	90	90	90	0.9328	0.1573	0.7406	2.58	184	−6.27
	B2(4a)								0.4525	0.6407	0.7113			
	B3(4a)								0.7454	0.2759	0.4451			
	B4(4a)								0.1356	0.5623	0.2260			
	B5(4a)								0.3300	0.9847	0.1083			
	B6(4a)								0.1799	0.7269	0.5661			
l-THC-B_{24}	B1(4a)	$P4_3$	6.39	6.39	4.66	90	90	90	0.9921	0.1423	0.2216	2.26	143	−6.16
	B2(4a)								0.2079	0.2678	0.0680			
	B3(4a)								0.2151	0.5309	0.2448			
	B4(4a)								0.4840	0.6277	0.2235			
	B5(4a)								0.7201	0.8277	0.2181			
	B6(4a)								0.3078	0.8791	0.6894			
r-THC-B_{24}	B1(4a)	$P4_1$	6.39	6.39	4.66	90	90	90	0.0079	0.8578	0.7786	2.26	143	−6.16
	B2(4a)								0.7915	0.7323	0.9314			
	B3(4a)								0.7852	0.4689	0.7555			
	B4(4a)								0.5161	0.3722	0.7766			
	B5(4a)								0.2796	0.1722	0.7818			
	B6(4a)								0.6927	0.1210	0.3108			
cF-B_8 [148]	B1(32e)	$Fd\bar{3}m$	8.57	8.57	8.57	90	90	90	−0.1796	0.3204	0.1796	0.91	70.42	−5.81
3D borophene [149]	B1(4i)	$C2/m$	5.47	2.81	1.85	90	70.22	90	0.6675	0.5000	0.8325	2.68	241.23	−6.31
α-B_{12} [150]	B1(18h)	$R\bar{3}m$	4.90	4.90	12.55	90	90	120	0.1188	0.8812	0.8915	2.48	237.16	−6.68
	B2(18h)								0.1969	0.8031	0.0242			

TABLE XXII. Elastic constants and mechanical-stability criteria of the five predicted boron structures. All elastic constants are given in gigapascals.

Structures	Elastic constants C_{11}	C_{12}	C_{13}	C_{16}	C_{33}	C_{44}	C_{66}	Stability criteria [151]
H-$P6_3$-B_{36}	463.41	99.82	70.49	–	271.87	81.01	181.80	$C_{11} > \lvert C_{12}\rvert$; $2C_{13}^2 < C_{33}(C_{11}+C_{12})$; $C_{44} > 0$; $C_{66} > 0$ or $2C_{16}^2 < C_{66}(C_{11}-C_{12})$
l-TQV-B_{24}	317.00	153.00	104.36	−19.74	295.49	150.17	135.64	
r-TQV-B_{24}	317.00	153.00	104.36	−19.74	295.48	150.17	135.64	
l-THC-B_{24}	204.47	125.71	90.81	18.04	267.46	114.88	75.60	
r-THC-B_{24}	203.23	124.03	90.17	17.16	268.60	114.92	73.11	

TABLE XXIII. Weyl-node positions, energies, chiral charges, and multiplicities in the five predicted boron structures. The momenta are given in fractional coordinates with respect to the primitive reciprocal-lattice vectors, and the energies are measured relative to the Fermi level.

Structures	WP	E (meV)	Coordinates (k_1, k_2, k_3)	Charge	Multiplicity
H-P6_3-B_{36}	W_1	−226.0	(0, 0, ±0.308)	−1	2
	W_2	−273.0	(0, 0, 0)	+2	1
l-TQV-B_{24}	W_1	0.0	±(0.184, −0.037, 0) ±(0.037, 0.184, 0)	−1	4
	W_2	0.0	(0, 0, ±0.195)	+2	2
r-TQV-B_{24}	W_1	0.0	±(0.184, −0.037, 0) ±(0.037, 0.184, 0)	+1	4
	W_2	0.0	(0, 0, ±0.195)	−2	2
l-THC-B_{24}	W_1	−2.1	±(−0.164, −0.097, ±0.185) ±(0.097, −0.164, ±0.185)	+1	8
	W_2	40.0	(0, 0, ±0.239)	−2	2
	W_3	−52.5	±(0.305, 0.081, 0) ±(0.081, −0.305, 0)	−1	4
r-THC-B_{24}	W_1	−8.4	±(0.171, 0.099, ±0.186) ±(0.099, −0.171, ±0.186)	−1	8
	W_2	39.8	(0, 0, ±0.242)	+2	2
	W_3	−60.2	±(0.308, 0.081, 0) ±(0.081, −0.308, 0)	+1	4

APPENDIX F: ADDITIONAL STRUCTURAL, PHONON, ELECTRONIC, AND SURFACE-STATE RESULTS

The five predicted boron allotropes are dynamically stable under the stated computational conditions, as their phonon dispersions contain no imaginary branches along the sampled high-symmetry paths (Fig. 9). The left- and right-handed TQV-B24 and THC-B24 structures form enantiomeric pairs (Figs. 10 and 11), while complementary bulk and surface electronic results for the predicted phases connect their structures to their IWM assignments (Figs. 12–15). Together, these calculations corroborate the single-IWM, integer-multiple, and hybrid-superposition realizations discussed in Sec. V.

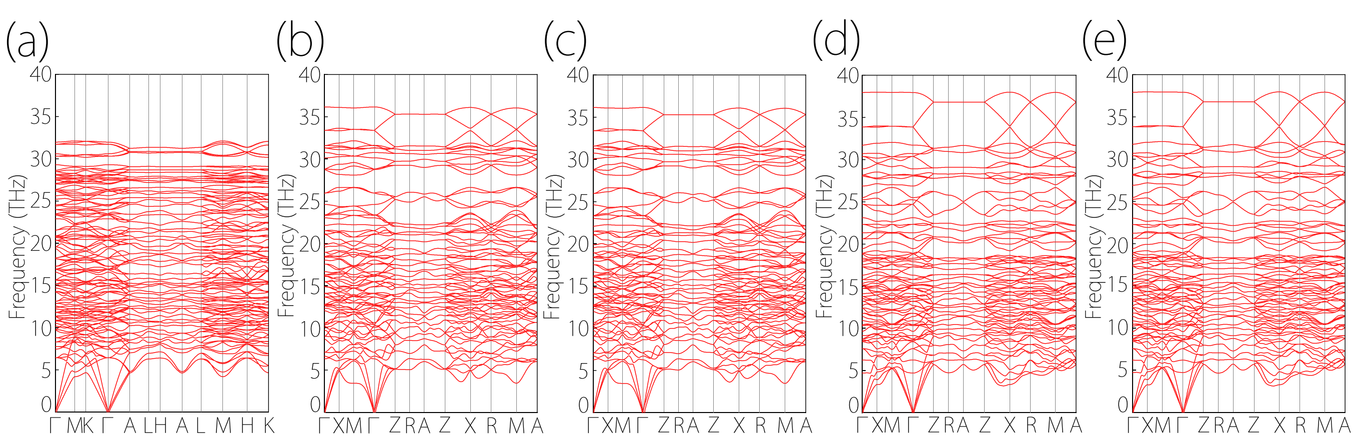

FIG. 9. Phonon dispersions of the five predicted boron allotropes: (a) H-P6_3-B_{36}, (b) l-TQV-B_{24}, (c) r-TQV-B_{24}, (d) l-THC-B_{24}, and (e) r-THC-B_{24}, calculated along all high-symmetry directions in the Brillouin zone.

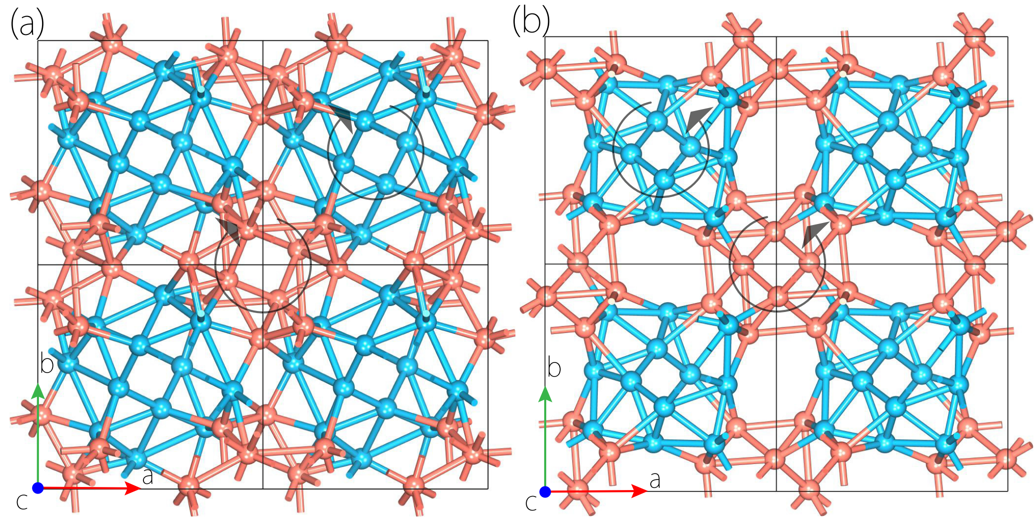

FIG. 10. Top views of the left-handed (a) *l*-TQV-B_{24} and right-handed (b) *r*-TQV-B_{24} structures.

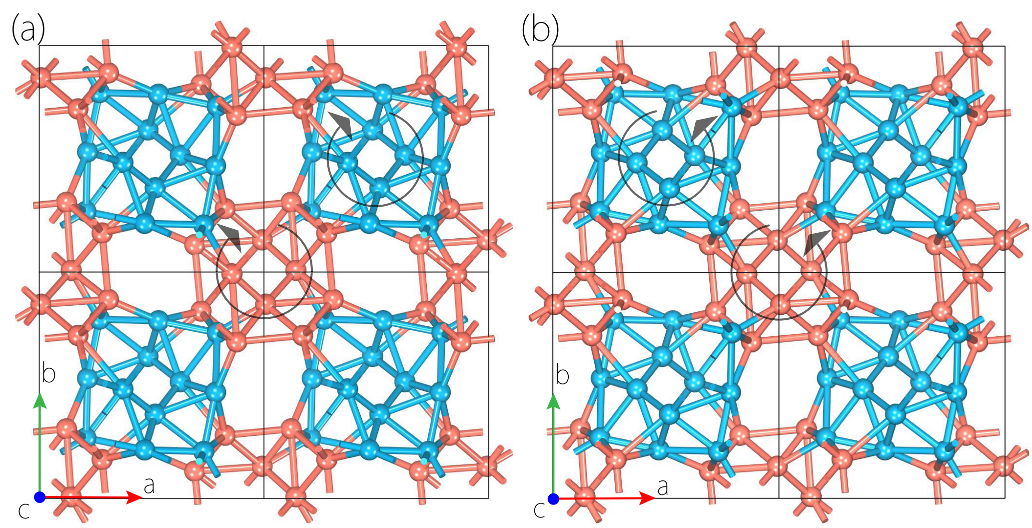

FIG. 11. Top views of the left-handed (a) *l*-THC-B_{24} and right-handed (b) *r*-THC-B_{24} structures.

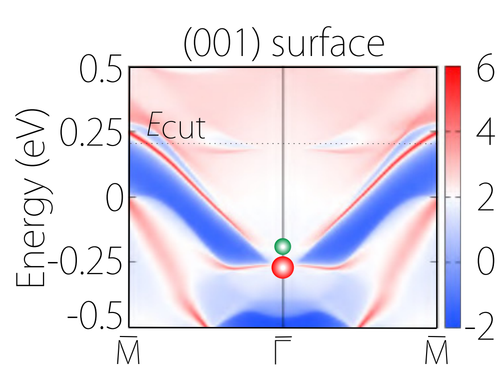

FIG. 12. Topological surface states of H-P6_3-B_{36} on the (001) surface.

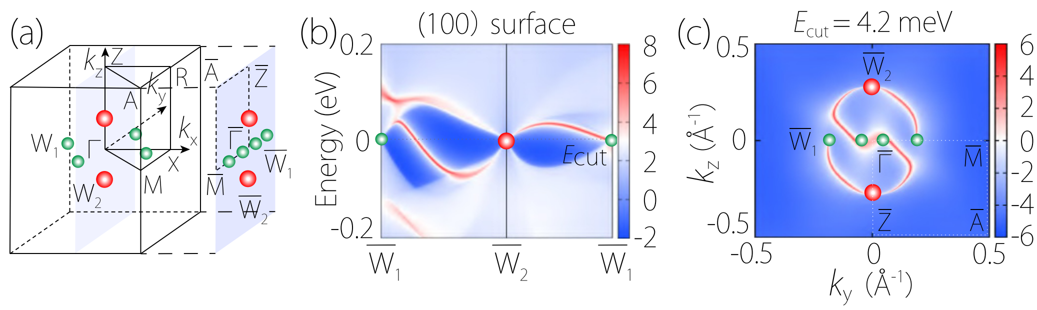

FIG. 13. The doubled IWM $2 \times \{2, -1, -1\}$ in *l*-TQV-B_{24}. (a) BZ distribution of six WPs. (b) Surface states and (c) isoenergy contour at 4.2 meV on the (100) surface. Bulk and projected Weyl nodes are marked by their chiral charges, with red and green spheres denoting positive and negative charges, respectively.

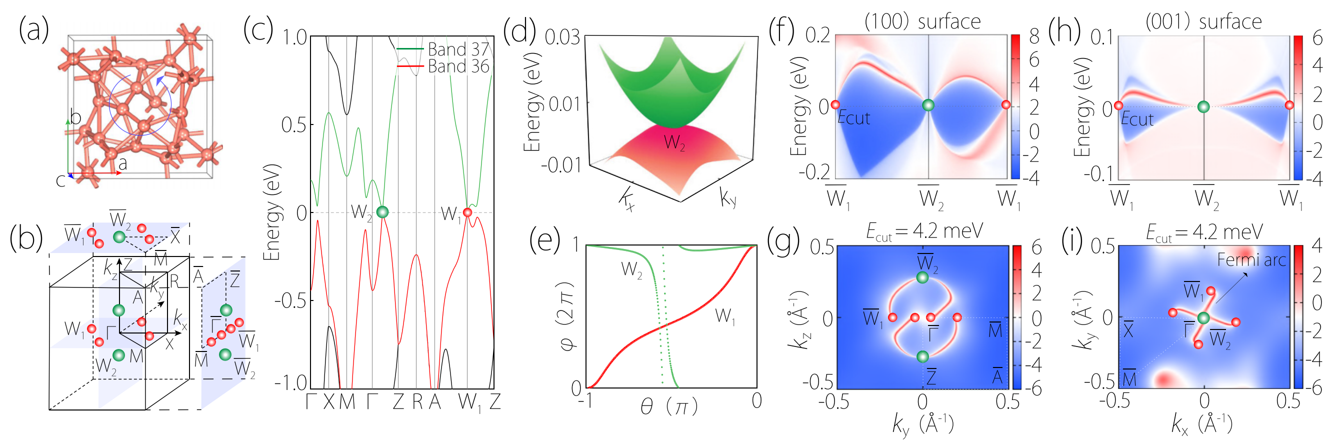

FIG. 14. Integer multiplicity IWM $2 \times \{2, -1, -1\}$ in *r*-TQV-B_{24}. (a) Primitive cell. (b) BZ distribution of six WPs. (c) Band structure. (d) Quadratic dispersion of W_2. (e) WCCs evolution yielding $C = -2$ (W_2) and $C = +1$ (W_1). (f) Surface states and (g) isoenergy contour at 4.2 meV on the (100) surface. (h) Surface states and (i) isoenergy contour at 4.2 meV on the (001) surface.

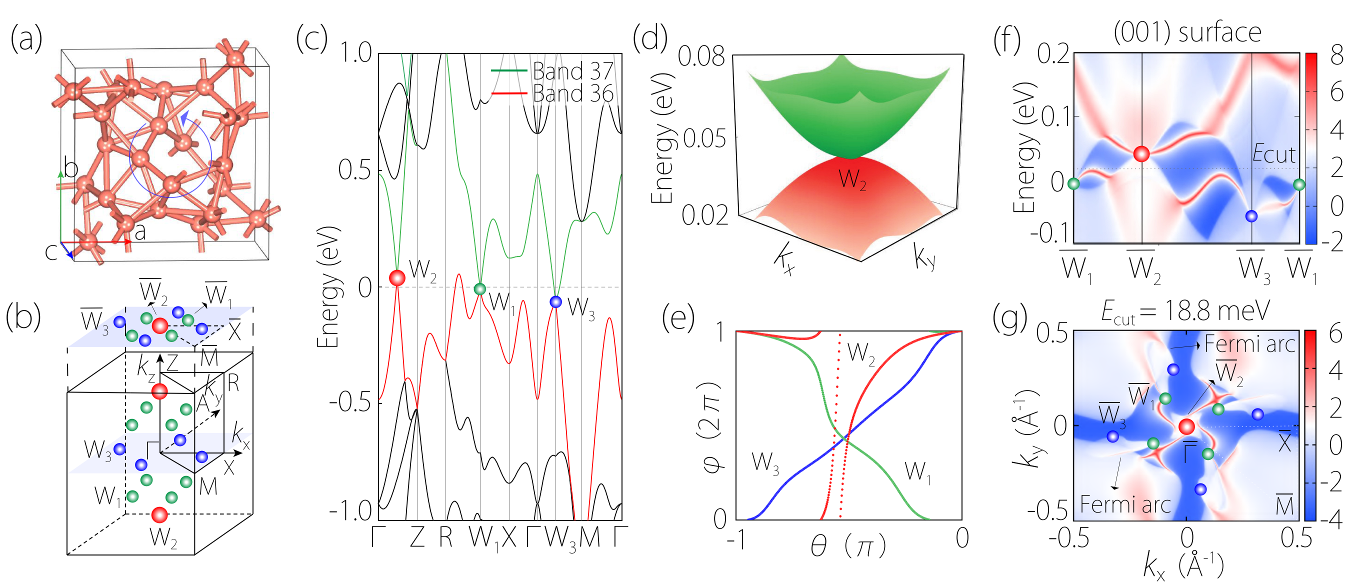

FIG. 15. Linear superposition $2 \times \{2, -1, -1\} + 4 \times \{1, -1\}$ in *r*-THC-B_{24}. (a) Primitive cell. (b) A rich constellation of 14 WPs in the BZ. (c) Band structure. (d) Quadratic dispersion of W_2. (e) WCCs calculations identifying chiral charges $C = +2$ for W_2, $C = -1$ for W_1 and $C = +1$ for W_3. (f) (001) surface states and (g) isoenergy contour at 18.8 meV exhibiting a complex "spider-web" Fermi-arc pattern consistent with the admissible connectivity motifs of the constituent IWM sectors for the selected surface and energy.

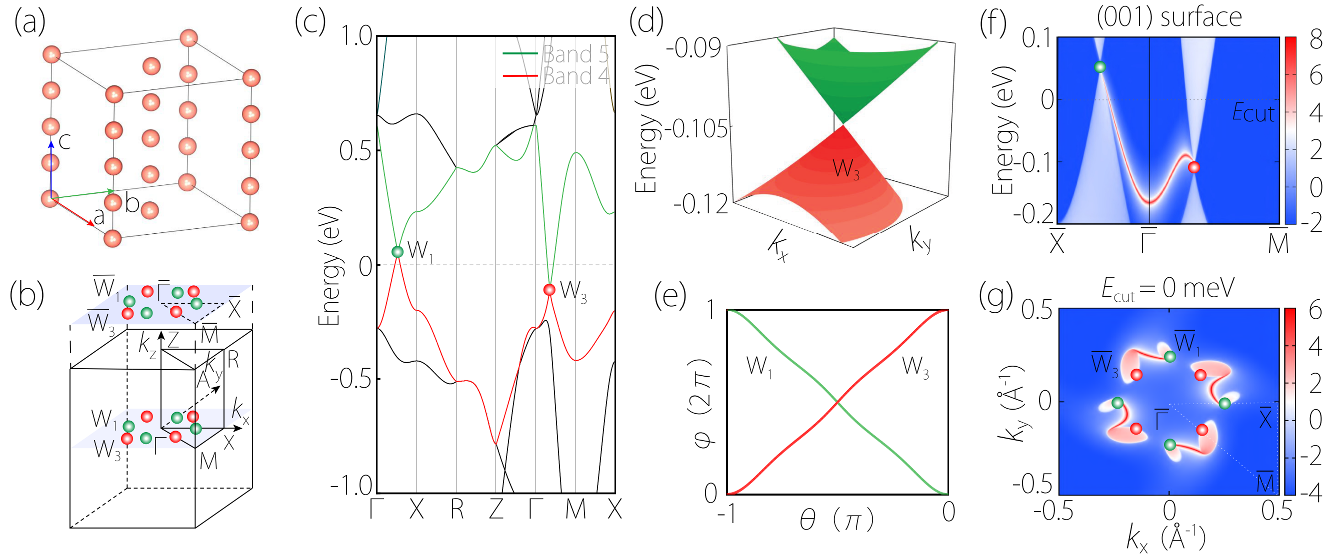

FIG. 16. Tight-binding model realization of the $4 \times \{1, -1\}$ IWM configuration. (a) Primitive unit cell. (b) Distribution of the eight Weyl points in the Brillouin zone. (c) Band structure. (d) Enlarged linear dispersion around a representative Weyl point W_3. (e) Evolution of Wannier charge centers confirming the unit chiral charge $|C| = 1$. (f) Surface states on the (001) surface. (g) Isoenergy contour at $E_{\mathrm{cut}} = 0$, exhibiting the characteristic single-arc connectivity of the $4 \times \{1, -1\}$ configuration. The corresponding lattice, basis, Hamiltonian construction, and nonzero model coefficients are given in Appendix G. The bulk and projected Weyl nodes are explicitly labeled by their respective chiral charges (red spheres for positive and green spheres for negative).

APPENDIX G: SYMMETRY-BASED TIGHT-BINDING REFERENCE FOR THE $4 \times \{1, -1\}$ SECTOR

1. Bulk and surface topology of the reference model

To isolate the unit-charge sector that enters the hybrid decomposition of l-THC-B$_{24}$, we constructed a symmetry-based tight-binding reference model realizing $4 \times \{1, -1\}$. The model contains eight Weyl points, or four charge-neutral pairs of unit-charge nodes, in the bulk Brillouin zone [Fig. 16(b)]. The representative linear crossing and Wannier-charge-center evolution confirm $|C| = 1$ [Figs. 16(d) and 16(e)]. On the (001) surface, the projected nodes are connected by four single Fermi arcs [Figs. 16(f) and 16(g)], providing an independent realization of the $4 \times \{1, -1\}$ end point-incidence sector used in the hybrid assembly.

2. Tight-binding construction and model parameters

The $4 \times \{1, -1\}$ reference in Fig. 16 is constructed for space group No. 78 on a tetragonal lattice with primitive vectors $\mathbf{a}_1 = (1, 0, 0)$, $\mathbf{a}_2 = (0, 1, 0)$, and $\mathbf{a}_3 = (0, 0, 1)$. Two s-orbital basis functions occupy $(0, 0, 0)$ and $(\frac{1}{2}, \frac{1}{2}, \frac{1}{2})$. The MAGNETICTB Hamiltonian is generated through the fourth-nearest-neighbor shell,

$$H(\mathbf{k}) = \sum_{n=1}^{5} H_n(\mathbf{k}), \tag{G1}$$

where H_1–H_5 denote the on site through fourth-nearest-neighbor contributions. In the MAGNETICTB notation, the nonzero coefficients are

$$e_1 = -0.145, \quad t_1 = -0.420, \quad t_2 = 0.805, \tag{G2}$$

$$r_1 = -0.055, \quad r_2 = -0.205, \quad s_1 = -0.700, \tag{G3}$$

$$s_2 = 0.840, \quad s_3 = -0.215, \quad s_4 = -0.120, \tag{G4}$$

$$p_{5n8} = -0.150, \quad p_{5n9} = 0.210, \tag{G5}$$

with all other coefficients set to zero.

[1] X. Wan, A. M. Turner, A. Vishwanath, and S. Y. Savrasov, Topological semimetal and Fermi-arc surface states in the electronic structure of pyrochlore iridates, Phys. Rev. B 83, 205101 (2011).

[2] A. A. Burkov and L. Balents, Weyl semimetal in a topological insulator multilayer, Phys. Rev. Lett. **107**, 127205 (2011).
[3] S.-Y. Xu, I. Belopolski, N. Alidoust, M. Neupane, G. Bian, C. Zhang, R. Sankar, G. Chang, Z. Yuan, C.-C. Lee, *et al.*, Discovery of a Weyl fermion semimetal and topological Fermi arcs, Science **349**, 613 (2015).
[4] A. A. Burkov, Weyl metals, Annu. Rev. Condens. Matter Phys. **9**, 359 (2018).
[5] H. Weng, C. Fang, Z. Fang, B. A. Bernevig, and X. Dai, Weyl semimetal phase in noncentrosymmetric transition-metal monophosphides, Phys. Rev. X **5**, 011029 (2015).
[6] B. Yan and C. Felser, Topological materials: Weyl semimetals, Annu. Rev. Condens. Matter Phys. **8**, 337 (2017).
[7] N. P. Armitage, E. J. Mele, and A. Vishwanath, Weyl and Dirac semimetals in three-dimensional solids, Rev. Mod. Phys. **90**, 015001 (2018).
[8] H. B. Nielsen and M. Ninomiya, The Adler-Bell-Jackiw anomaly and Weyl fermions in a crystal, Phys. Lett. B **130**, 389 (1983).
[9] D. T. Son and B. Z. Spivak, Chiral anomaly and classical negative magnetoresistance of Weyl metals, Phys. Rev. B **88**, 104412 (2013).
[10] K.-Y. Yang, Y.-M. Lu, and Y. Ran, Quantum Hall effects in a Weyl semimetal: Possible application in pyrochlore iridates, Phys. Rev. B **84**, 075129 (2011).
[11] C. Fang, M. J. Gilbert, X. Dai, and B. A. Bernevig, Multi-Weyl topological semimetals stabilized by point group symmetry, Phys. Rev. Lett. **108**, 266802 (2012).
[12] S. S. Tsirkin, I. Souza, and D. Vanderbilt, Composite Weyl nodes stabilized by screw symmetry with and without time-reversal invariance, Phys. Rev. B **96**, 045102 (2017).
[13] M.-L. Chang, M. Xiao, W.-J. Chen, and C. T. Chan, Multiple Weyl points and the sign change of their topological charges in woodpile photonic crystals, Phys. Rev. B **95**, 125136 (2017).
[14] G. Liu, Z. Chen, P. Wu, and H. Xu, Triple hourglass Weyl phonons, Phys. Rev. B **106**, 214308 (2022).
[15] X. Wang, F. Zhou, Z. Zhang, Z.-M. Yu, and Y. Yao, Hourglass charge-three Weyl phonons, Phys. Rev. B **106**, 214309 (2022).
[16] X. Xiao, Y. Jin, D.-S. Ma, W. Kong, J. Fan, R. Wang, and X. Wu, Ideal hourglass-type charge-three Weyl fermions in spinless systems, Phys. Rev. B **109**, 075160 (2024).
[17] T. Zhang, R. Takahashi, C. Fang, and S. Murakami, Twofold quadruple Weyl nodes in chiral cubic crystals, Phys. Rev. B **102**, 125148 (2020).
[18] Q. Chen, F. Chen, Y. Pan, C. Cui, Q. Yan, L. Zhang, Z. Gao, S. A. Yang, Z.-M. Yu, H. Chen, B. Zhang, and Y. Yang, Discovery of a maximally charged Weyl point, Nat. Commun. **13**, 7359 (2022).
[19] H. B. Nielsen and M. Ninomiya, Absence of neutrinos on a lattice: (I). Proof by homotopy theory, Nucl. Phys. B **185**, 20 (1981).
[20] H. B. Nielsen and M. Ninomiya, Absence of neutrinos on a lattice: (II). Intuitive topological proof, Nucl. Phys. B **193**, 173 (1981).
[21] Z.-M. Yu, Z. Zhang, G.-B. Liu, W. Wu, X.-P. Li, R.-W. Zhang, S. A. Yang, and Y. Yao, Encyclopedia of emergent particles in three-dimensional crystals, Sci. Bull. **67**, 375 (2022).
[22] G.-B. Liu, Z. Zhang, Z.-M. Yu, S. A. Yang, and Y. Yao, Systematic investigation of emergent particles in type-III magnetic space groups, Phys. Rev. B **105**, 085117 (2022).
[23] Z. Zhang, G.-B. Liu, Z.-M. Yu, S. A. Yang, and Y. Yao, Encyclopedia of emergent particles in type-IV magnetic space groups, Phys. Rev. B **105**, 104426 (2022).
[24] B. Q. Lv, T. Qian, and H. Ding, Experimental perspective on three-dimensional topological semimetals, Rev. Mod. Phys. **93**, 025002 (2021).
[25] M. Zhong, N. T. T. Vu, W. Zhai, J. R. Soh, Y. Liu, J. Wu, A. Suwardi, H. Liu, G. Chang, K. P. Loh, W. Gao, C.-W. Qiu, J. K. W. Yang, and Z. Dong, Weyl semimetals: From principles, materials to applications, Adv. Mater. **37**, 2506236 (2025).
[26] H. Gao, J. W. Venderbos, Y. Kim, and A. M. Rappe, Topological semimetals from first principles, Annu. Rev. Mater. Res. **49**, 153 (2019).
[27] D. J. Grynkiewicz, *Structural Additive Theory*, *Developments in Mathematics* (Springer International Publishing, Heidelberg, 2013), Vol. 30.
[28] P. A. Sissokho, A note on minimal zero-sum sequences over Z, Acta Arith. **166**, 279 (2014).
[29] A. Schrijver, *Theory of Linear and Integer Programming* (John Wiley & Sons, New York, NY, 1998).
[30] W. Bruns and H. J. Herzog, *Cohen-Macaulay Rings* (Cambridge University Press, Cambridge, 1998), Vol. 39.
[31] 4ti2 team, 4ti2—A software package for algebraic, geometric and combinatorial problems on linear spaces.
[32] A. Hatcher, *Algebraic Topology* (Cambridge University Press, Cambridge, 2002).
[33] Y.-Y. Bai, K.-X. Pang, and Y. Gao, Symmetry-protected four double-Weyl fermions and their topological phase transitions in nonmagnetic crystals, arXiv:2604.07301 (2026).
[34] V. Dwivedi, Fermi arc reconstruction at junctions between Weyl semimetals, Phys. Rev. B **97**, 064201 (2018).
[35] P. Hohenberg and W. Kohn, Inhomogeneous electron gas, Phys. Rev. **136**, B864 (1964).
[36] W. Kohn and L. J. Sham, Self-consistent equations including exchange and correlation effects, Phys. Rev. **140**, A1133 (1965).
[37] S. Baroni, S. De Gironcoli, A. Dal Corso, and P. Giannozzi, Phonons and related crystal properties from density-functional perturbation theory, Rev. Mod. Phys. **73**, 515 (2001).
[38] P. Giannozzi, S. Baroni, N. Bonini, M. Calandra, R. Car, C. Cavazzoni, D. Ceresoli, G. L. Chiarotti, M. Cococcioni, I. Dabo, *et al.*, QUANTUM ESPRESSO: A modular and open-source software project for quantum simulations of materials, J. Phys.: Condens. Matter **21**, 395502 (2009).
[39] N. Troullier and J. L. Martins, Efficient pseudopotentials for plane-wave calculations, Phys. Rev. B **43**, 1993 (1991).
[40] J. P. Perdew, K. Burke, and M. Ernzerhof, Generalized gradient approximation made simple, Phys. Rev. Lett. **77**, 3865 (1996).
[41] H. J. Monkhorst and J. D. Pack, Special points for Brillouin-zone integrations, Phys. Rev. B **13**, 5188 (1976).
[42] A. A. Mostofi, J. R. Yates, G. Pizzi, Y.-S. Lee, I. Souza, D. Vanderbilt, and N. Marzari, An updated version of Wannier90: A tool for obtaining maximally-localised Wannier functions, Comput. Phys. Commun. **185**, 2309 (2014).
[43] Z. Zhang, Z.-M. Yu, G.-B. Liu, and Y. Yao, MagneticTB: A package for tight-binding model of magnetic and non-magnetic materials, Comput. Phys. Commun. **270**, 108153 (2022).

[44] R. Yu, X. L. Qi, A. Bernevig, Z. Fang, and X. Dai, Equivalent expression of Z_2 topological invariant for band insulators using the non-Abelian Berry connection, Phys. Rev. B **84**, 075119 (2011).
[45] Q. Wu, S. Zhang, H.-F. Song, M. Troyer, and A. A. Soluyanov, WannierTools: An open-source software package for novel topological materials, Comput. Phys. Commun. **224**, 405 (2018).
[46] S. Fredericks, R. Parrish, D. Sayre, and Q. Zhu, PyXtal: A Python library for crystal structure generation and symmetry analysis, Comput. Phys. Commun. **261**, 107810 (2021).
[47] B. Deng, P. Zhong, K. Jun, J. Riebesell, K. Han, C. J. Bartel, and G. Ceder, CHGNet as a pretrained universal neural network potential for charge-informed atomistic modeling, Nat. Mach. Intell. **5**, 1031 (2023).
[48] A. Togo and I. Tanaka, First-principles phonon calculations in materials science, Scr. Mater. **108**, 1 (2015).
[49] B. Bradlyn, L. Elcoro, J. Cano, M. G. Vergniory, Z. Wang, C. Felser, M. I. Aroyo, and B. A. Bernevig, Topological quantum chemistry, Nature (London) **547**, 298 (2017).
[50] H. C. Po, A. Vishwanath, and H. Watanabe, Symmetry-based indicators of band topology in the 230 space groups, Nat. Commun. **8**, 50 (2017).
[51] G. Chang, S.-Y. Xu, B. J. Wieder, D. S. Sanchez, S.-M. Huang, I. Belopolski, S.-Y. Lee, G. Bian, H. Zheng, N. Alidoust, *et al.*, Unconventional chiral fermions and large topological Fermi arcs in RhSi, Phys. Rev. Lett. **119**, 206401 (2017).
[52] D. S. Sanchez, I. Belopolski, T. A. Cochran, X. Xu, J.-X. Yin, G. Chang, W. Xie, K. Manna, V. Süß, C.-Y. Huang, *et al.*, Topological chiral crystals with helicoid-arc quantum states, Nature (London) **567**, 500 (2019).
[53] Z. Rao, N. B. M. Schröter, Y. Sun, N. Kumar, P. J. W. Moll, C. Felser, B. Yan, and J. Gooth, Observation of unconventional chiral fermions with long Fermi arcs in CoSi, Nature (London) **567**, 496 (2019).
[54] B. Bradlyn, J. Cano, Z. Wang, M. G. Vergniory, C. Felser, R. J. Cava, and B. A. Bernevig, Beyond Dirac and Weyl fermions: Unconventional quasiparticles in conventional crystals, Science **353**, aaf5037 (2016).
[55] P. Tang, Q. Zhou, G. Zhang, S. Liu, Q. Niu, S.-C. Zhang, and X. Wan, Three-dimensional strongly topological gapless phases in noncentrosymmetric metals, Nat. Phys. **13**, 683 (2017).
[56] N. B. M. Schröter, D. Pei, M. G. Vergniory, Y. Sun, K. Manna, F. De Juan, Jonas. A. Krieger, V. Süss, M. Schmidt, P. Dudin, B. Bradlyn, T. K. Kim, T. Schmitt, C. Cacho, C. Felser, V. N. Strocov, and Y. Chen, Chiral topological semimetal with multifold band crossings and long Fermi arcs, Nat. Phys. **15**, 759 (2019).
[57] T. Zhang, Z. Song, A. Alexandradinata, and C. Fang, Double-Weyl phonons in transition-metal monosilicides, Phys. Rev. Lett. **120**, 016401 (2018).
[58] H. Miao, T. Zhang, L. Wang, D. Meyers, A. H. Said, V. B. Prakapenka, J. Kohlbrecher, W. Yao, Y. Song, C. Fang, *et al.*, Topological phonons and phonon surface arcs in transition-metal monosilicides, Phys. Rev. Lett. **121**, 035302 (2018).
[59] G. Ding, F. Zhou, Z. Zhang, Z.-M. Yu, and X. Wang, Charge-two Weyl phonons with type-III dispersion, Phys. Rev. B **105**, 134303 (2022).
[60] Q.-B. Liu, Z. Wang, and H.-H. Fu, Charge-four Weyl phonons, Phys. Rev. B **103**, L161303 (2021).
[61] Y. Yang, C. Xie, Y. Cui, X. Wang, and W. Wu, Maximally charged single-pair multi-Weyl point phonons in *P*23-type BeH_2, Phys. Rev. B **107**, 054310 (2023).
[62] L. Lu, Z. Wang, D. Ye, L. Ran, L. Fu, J. D. Joannopoulos, and M. Soljačić, Experimental observation of Weyl points, Science **349**, 622 (2015).
[63] W. Gao, M. Lawrence, B. Yang, F. Liu, F. Fang, B. Béri, J. Li, and S. Zhang, Photonic Weyl degeneracies in magnetized plasma, Nat. Commun. **7**, 12435 (2016).
[64] J. Noh, S. Huang, D. Leykam, Y. D. Chong, K. P. Chen, and M. C. Rechtsman, Experimental observation of optical Weyl points and Fermi arc-like surface states, Nat. Phys. **13**, 611 (2017).
[65] B. Yang, Q. Gao, Y. Guo, B. Tremain, F. Liu, L. E. Barr, S. Zhang, L. Chen, W. Gao, and L. Lu, Ideal Weyl points and helicoid surface states in artificial photonic crystal structures, Science **359**, 1013 (2018).
[66] P. Diaconis and B. Sturmfels, Algebraic algorithms for sampling from conditional distributions, Ann. Statist. **26**, 363 (1998).
[67] B. Sturmfels, *Gröbner Bases and Convex Polytopes* (American Mathematical Society, Providence, RI, 1996).
[68] H. Zhang, J. Wang, G. Xu, Y. Xu, and S.-C. Zhang, Topological states in ferromagnetic CdO/EuO superlattices and quantum wells, Phys. Rev. Lett. **112**, 096804 (2014).
[69] M. M. Hirschmann, A. Leonhardt, B. Kilic, D. H. Fabini, and A. P. Schnyder, Symmetry-enforced band crossings in tetragonal materials: Dirac and Weyl degeneracies on points, lines, and planes, Phys. Rev. Mater. **5**, 054202 (2021).
[70] J.-R. Soh, F. De Juan, M. G. Vergniory, N. B. M. Schröter, M. C. Rahn, D. Y. Yan, J. Jiang, M. Bristow, P. A. Reiss, J. N. Blandy, Y. F. Guo, Y. G. Shi, T. K. Kim, A. McCollam, S. H. Simon, Y. Chen, A. I. Coldea, and A. T. Boothroyd, Ideal Weyl semimetal induced by magnetic exchange, Phys. Rev. B **100**, 201102 (2019).
[71] L.-L. Wang, N. H. Jo, B. Kuthanazhi, Y. Wu, R. J. McQueeney, A. Kaminski, and P. C. Canfield, Single pair of Weyl fermions in the half-metallic semimetal $EuCd_2As_2$, Phys. Rev. B **99**, 245147 (2019).
[72] Z. Li, D.-D. Xu, S.-Y. Ning, H. Su, T. Iitaka, T. Tohyama, and J.-X. Zhang, Predicted Weyl fermions in magnetic GdBi and GdSb, Int. J. Mod. Phys. B **31**, 1750217 (2017).
[73] D. Bulmash, C.-X. Liu, and X.-L. Qi, Prediction of a Weyl semimetal in $Hg_{1-x-y}Cd_xMn_yTe$, Phys. Rev. B **89**, 081106 (2014).
[74] X.-L. Yu, Y.-J. Jin, and J. Wu, Theoretical study of $HgCr_2Se_{3.5}Te_{0.5}$: A doping-site-dependent semimetal, Sci. Rep. **6**, 30866 (2016).
[75] J. Li, C. Wang, Z. Zhang, B.-L. Gu, W. Duan, and Y. Xu, Magnetically controllable topological quantum phase transitions in the antiferromagnetic topological insulator $MnBi_2Te_4$, Phys. Rev. B **100**, 121103 (2019).
[76] Y. Gao, W. K. Wu, B. C. Gong, H. C. Yang, X. F. Zhou, Y. Liu, S. A. Yang, K. Liu, and Z. Y. Lu, Intrinsic ferromagnetic axion states and single pair of Weyl fermions in the stable-state $MnX_2B_2T_6$ family of materials, Phys. Rev. B **107**, 045136 (2023).

[77] H. Liu, J. Cao, Z. Zhang, J. Liang, L. Wang, and S. A. Yang, Ideal spin-polarized Weyl half-semimetal with a single pair of Weyl points in the half-Heusler compounds X CrTe (X = K, Rb), Phys. Rev. B **109**, 174426 (2024).

[78] S. M. Nie, T. Hashimoto, and F. B. Prinz, Magnetic Weyl semimetal in $K_2Mn_3(AsO_4)_3$ with the minimum number of Weyl points, Phys. Rev. Lett. **128**, 176401 (2022).

[79] A. Pham and P. Ganesh, Quantum material topology via defect engineering, Phys. Rev. B **100**, 241110 (2019).

[80] V. Ivanov, X. Wan, and S. Y. Savrasov, Topological insulator-to-Weyl semimetal transition in strongly correlated actinide system UNiSn, Phys. Rev. X **9**, 041055 (2019).

[81] Z. Wang, Q. Liu, J.-W. Luo, and A. Zunger, Digging for topological property in disordered alloys: The emergence of Weyl semimetal phase and sequential band inversions in PbSe–SnSe alloys, Mater. Horiz. **6**, 2124 (2019).

[82] J. Liu, X. Ma, L. Sun, Z. Zhang, Y. Ni, S. Meng, and M. Zhao, Ideal type-I Weyl phonons in $BAsO_4$ with fewest Weyl points, Phys. Rev. B **109**, 045203 (2024).

[83] C. Zhang, X.-Y. Ding, L.-Y. Gan, Y. Cao, B.-S. Li, X. Wu, and R. Wang, Symmetry-guaranteed ideal Weyl semimetallic phase in face-centered orthogonal C_6, Phys. Rev. B **101**, 235119 (2020).

[84] E. V. Gorbar, V. A. Miransky, I. A. Shovkovy, and P. O. Sukhachov, Surface Fermi arcs in Z_2 Weyl semimetals A_3Bi (A = Na, K, Rb), Phys. Rev. B **91**, 235138 (2015).

[85] K. Koepernik, D. Kasinathan, D. V. Efremov, S. Khim, S. Borisenko, B. Büchner, and J. Van Den Brink, $TaIrTe_4$: A ternary type-II Weyl semimetal, Phys. Rev. B **93**, 201101 (2016).

[86] S. Fan, B. Fu, D.-S. Ma, and R. Wang, Complete topological phase diagram and realization of minimum Weyl nodes in a sheared chiral crystal of elemental tellurium, Phys. Rev. B **108**, 235211 (2023).

[87] L. Meng, J. Wu, J. Zhong, and R. A. Römer, A type of robust superlattice type-I Weyl semimetal with four Weyl nodes, Nanoscale **11**, 18358 (2019).

[88] C.-L. Zhang, F. Schindler, H. Liu, T.-R. Chang, S.-Y. Xu, G. Chang, W. Hua, H. Jiang, Z. Yuan, J. Sun, H.-T. Jeng, H.-Z. Lu, H. Lin, M. Z. Hasan, X. C. Xie, T. Neupert, and S. Jia, Ultraquantum magnetoresistance in the Kramers-Weyl semimetal candidate β-Ag_2Se, Phys. Rev. B **96**, 165148 (2017).

[89] C.-C. Liu, J.-J. Zhou, Y. Yao, and F. Zhang, Weak topological insulators and composite Weyl semimetals: β-Bi_4X_4 (X = Br, I), Phys. Rev. Lett. **116**, 066801 (2016).

[90] E. Liu, Y. Sun, N. Kumar, L. Muechler, A. Sun, L. Jiao, S.-Y. Yang, D. Liu, A. Liang, Q. Xu, *et al.*, Giant anomalous Hall effect in a ferromagnetic kagome-lattice semimetal, Nat. Phys. **14**, 1125 (2018).

[91] W. Shon, D.-C. Ryu, K. Kim, B. I. Min, B. Kim, B. Kang, B. K. Cho, H.-J. Kim, and J.-S. Rhyee, Magnetic field-induced type-II Weyl semimetallic state in geometrically frustrated Shastry-Sutherland lattice GdB_4, Mater. Today Phys. **11**, 100168 (2019).

[92] B. Singh, A. Sharma, H. Lin, M. Z. Hasan, R. Prasad, and A. Bansil, Topological electronic structure and Weyl semimetal in the $TlBiSe_2$ class of semiconductors, Phys. Rev. B **86**, 115208 (2012).

[93] Z. Wang, K. Luo, J. Zhao, and R. Yu, Large Fermi arc and robust Weyl semimetal phase in Ag_2S, Phys. Rev. B **100**, 205117 (2019).

[94] J. Ruan, S.-K. Jian, D. Zhang, H. Yao, H. Zhang, S.-C. Zhang, and D. Xing, Ideal Weyl semimetals in the chalcopyrites $CuTlSe_2$, $AgTlTe_2$, $AuTlTe_2$, and $ZnPbAs_2$, Phys. Rev. Lett. **116**, 226801 (2016).

[95] X. Wan, A. Vishwanath, and S. Y. Savrasov, Computational design of axion insulators based on 5*d* spinel compounds, Phys. Rev. Lett. **108**, 146601 (2012).

[96] G. B. Halász and L. Balents, Time-reversal invariant realization of the Weyl semimetal phase, Phys. Rev. B **85**, 035103 (2012).

[97] T. Rauch, S. Achilles, J. Henk, and I. Mertig, Spin chirality tuning and topological semimetals in strained $HgTe_xS_{1-x}$, Phys. Rev. Lett. **114**, 236805 (2015).

[98] T. Rauch, S. Achilles, J. Henk, and I. Mertig, Multiple topological nontrivial phases in strained $Hg_xCd_{1-x}Te$, Phys. Rev. B **96**, 035124 (2017).

[99] G. Autès, D. Gresch, M. Troyer, A. A. Soluyanov, and O. V. Yazyev, Robust type-II Weyl semimetal phase in transition metal diphosphides XP_2 (X = Mo, W), Phys. Rev. Lett. **117**, 066402 (2016).

[100] Z. Wang, D. Gresch, A. A. Soluyanov, W. Xie, S. Kushwaha, X. Dai, M. Troyer, R. J. Cava, and B. A. Bernevig, $MoTe_2$: A type-II Weyl topological metal, Phys. Rev. Lett. **117**, 056805 (2016).

[101] I. Belopolski, D. S. Sanchez, Y. Ishida, X. Pan, P. Yu, S.-Y. Xu, G. Chang, T.-R. Chang, H. Zheng, N. Alidoust, *et al.*, Discovery of a new type of topological Weyl fermion semimetal state in $Mo_xW_{1-x}Te_2$, Nat. Commun. **7**, 13643 (2016).

[102] G. Chang, S.-Y. Xu, D. S. Sanchez, S.-M. Huang, C.-C. Lee, T.-R. Chang, G. Bian, H. Zheng, I. Belopolski, N. Alidoust, H.-T. Jeng, A. Bansil, H. Lin, and M. Z. Hasan, A strongly robust type II Weyl fermion semimetal state in Ta_3S_2, Sci. Adv. **2**, e1600295 (2016).

[103] A. A. Soluyanov, D. Gresch, Z. Wang, Q. Wu, M. Troyer, X. Dai, and B. A. Bernevig, Type-II Weyl semimetals, Nature (London) **527**, 495 (2015).

[104] S. Borisenko, D. Evtushinsky, Q. Gibson, A. Yaresko, K. Koepernik, T. Kim, M. Ali, J. Van Den Brink, M. Hoesch, A. Fedorov, E. Haubold, Y. Kushnirenko, I. Soldatov, R. Schäfer, and R. J. Cava, Time-reversal symmetry breaking type-II Weyl state in $YbMnBi_2$, Nat. Commun. **10**, 3424 (2019).

[105] R. Wang, Y. J. Jin, J. Z. Zhao, Z. J. Chen, Y. J. Zhao, and H. Xu, Ferromagnetic Weyl fermions in CrO_2, Phys. Rev. B **97**, 195157 (2018).

[106] Y.-H. Su, W. Shi, C. Felser, and Y. Sun, Topological Weyl semimetals in $Bi_{1-x}Sb_x$ alloys, Phys. Rev. B **97**, 155431 (2018).

[107] J. Liu and D. Vanderbilt, Weyl semimetals from noncentrosymmetric topological insulators, Phys. Rev. B **90**, 155316 (2014).

[108] H. Gao, Y. Kim, J. W. F. Venderbos, C. L. Kane, E. J. Mele, A. M. Rappe, and W. Ren, Dirac-Weyl semimetal: Coexistence of Dirac and Weyl fermions in polar hexagonal *ABC* crystals, Phys. Rev. Lett. **121**, 106404 (2018).

[109] Y. J. Jin, Y. Xu, Z. J. Chen, and H. Xu, Type-II quadratic and cubic Weyl fermions, Phys. Rev. B **105**, 035141 (2022).

[110] S. Ullah, L. Wang, J. Li, R. Li, and X.-Q. Chen, Structural, elastic, and electronic properties of topological semimetal WC-type MX family by first-principles calculation, Chin. Phys. B **28**, 077105 (2019).

[111] Y. Du, X. Bo, D. Wang, E.-J. Kan, C.-G. Duan, S. Y. Savrasov, and X. Wan, Emergence of topological nodal lines and type-II Weyl nodes in the strong spin-orbit coupling system InNb X_2 (X = S, Se), Phys. Rev. B **96**, 235152 (2017).

[112] H. Sun and J. Zhao, New family of Dirac and Weyl semimetals in XAuTe (X = Na, K, Rb) ternary honeycomb compounds, Sci. China Phys. Mech. Astron. **59**, 107011 (2016).

[113] J. Kübler and C. Felser, Weyl fermions in antiferromagnetic Mn_3Sn and Mn_3Ge, Europhys. Lett. **120**, 47002 (2017).

[114] S. Nakatsuji, N. Kiyohara, and T. Higo, Large anomalous Hall effect in a non-collinear antiferromagnet at room temperature, Nature (London) **527**, 212 (2015).

[115] T. Inoshita, M. Hirayama, N. Hamada, H. Hosono, and S. Murakami, Topological semimetal phases manifested in transition metal dichalcogenides intercalated with 3d metals, Phys. Rev. B **100**, 121112 (2019).

[116] D. Grassano, N. Marzari, and D. Campi, High-throughput screening of Weyl semimetals, Phys. Rev. Mater. **8**, 024201 (2024).

[117] J.-P. Sun, D. Zhang, and K. Chang, Coexistence of topological nodal lines, Weyl points, and triply degenerate points in TaS, Phys. Rev. B **96**, 045121 (2017).

[118] S. Gupta, R. Juneja, R. Shinde, and A. K. Singh, Topologically nontrivial electronic states in $CaSn_3$, J. Appl. Phys. **121**, 214901 (2017).

[119] Y. Xu, C. Yue, H. Weng, and X. Dai, Heavy Weyl fermion state in $CeRu_4Sn_6$, Phys. Rev. X **7**, 011027 (2017).

[120] L. Li, H.-H. Xie, J.-S. Zhao, X.-X. Liu, J.-B. Deng, X.-R. Hu, and X.-M. Tao, Ternary Weyl semimetal $NbIrTe_4$ proposed from first-principles calculation, Phys. Rev. B **96**, 024106 (2017).

[121] Y. Du, E.-J. Kan, H. Xu, S. Y. Savrasov, and X. Wan, Turning copper metal into a Weyl semimetal, Phys. Rev. B **97**, 245104 (2018).

[122] Y. Venkateswara, S. S. Samatham, P. D. Babu, K. G. Suresh, and A. Alam, Coexistence of spin semimetal and Weyl semimetal behavior in FeRhCrGe, Phys. Rev. B **100**, 180404 (2019).

[123] Y. Qian, S. Nie, C. Yi, L. Kong, C. Fang, T. Qian, H. Ding, Y. Shi, Z. Wang, H. Weng, and Z. Fang, Topological electronic states in HfRuP family superconductors, npj Comput. Mater. **5**, 121 (2019).

[124] L. Meng, Y. Li, J. Wu, L. Zhao, and J. Zhong, A type of novel Weyl semimetal candidate: Layered transition metal monochalcogenides Mo_2XY (X, Y = S, Se, Te, X $\neq$ Y), Nanoscale **12**, 4602 (2020).

[125] L. Meng, J. Wu, Y. Li, L. Zhao, and J. Zhong, Weyl semimetal phase in the noncentrosymmetric superlattice W_2XY (X, Y = S, Se, Te, X $\neq$ Y), Phys. Rev. B **100**, 155151 (2019).

[126] R. Tan, Z. Li, P. Zhou, Z. Ma, C. Tan, and L. Sun, Coexistence of Weyl and type-II triply degenerate fermions in a ternary topological semimetal YPtP, Phys. Status Solidi RRL **13**, 1900421 (2019).

[127] G. Chang, B. Singh, S.-Y. Xu, G. Bian, S.-M. Huang, C.-H. Hsu, I. Belopolski, N. Alidoust, D. S. Sanchez, H. Zheng, *et al.*, Magnetic and noncentrosymmetric Weyl fermion semimetals in the R AlGe family of compounds (R = rare earth), Phys. Rev. B **97**, 041104 (2018).

[128] S.-Y. Xu, N. Alidoust, G. Chang, H. Lu, B. Singh, I. Belopolski, D. S. Sanchez, X. Zhang, G. Bian, H. Zheng, *et al.*, Discovery of Lorentz-violating type II Weyl fermions in LaAlGe, Sci. Adv. **3**, e1603266 (2017).

[129] S.-M. Huang, S.-Y. Xu, I. Belopolski, C.-C. Lee, G. Chang, T.-R. Chang, B. Wang, N. Alidoust, G. Bian, M. Neupane, D. Sanchez, H. Zheng, H.-T. Jeng, A. Bansil, T. Neupert, H. Lin, and M. Z. Hasan, New type of Weyl semimetal with quadratic double Weyl fermions, Proc. Natl. Acad. Sci. USA **113**, 1180 (2016).

[130] H. Li, S. Xu, Z.-C. Rao, L.-Q. Zhou, Z.-J. Wang, S.-M. Zhou, S.-J. Tian, S.-Y. Gao, J.-J. Li, Y.-B. Huang, H.-C. Lei, H.-M. Weng, Y.-J. Sun, T.-L. Xia, T. Qian, and H. Ding, Chiral fermion reversal in chiral crystals, Nat. Commun. **10**, 5505 (2019).

[131] X. Xiao, Y. Jin, D.-S. Ma, H. Wei, J. Fan, R. Wang, and X. Wu, Single pair of charge-2 high-fold fermions with surface type-II Van Hove singularities in ultralight chiral crystals, Phys. Rev. B **109**, 165136 (2024).

[132] G. Ding, J. Wang, Z.-M. Yu, Z. Zhang, W. Wang, and X. Wang, Single pair of type-III Weyl points half-metals: $BaNiIO_6$ as an example, Phys. Rev. Mater. **7**, 014202 (2023).

[133] N. Heinsdorf, M. H. Christensen, M. Iraola, S.-S. Zhang, F. Yang, T. Birol, C. D. Batista, R. Valentí, and R. M. Fernandes, Prediction of double-Weyl points in the iron-based superconductor $CaKFe_4As_4$, Phys. Rev. B **104**, 075101 (2021).

[134] S. Zhang, Y. Liu, X. Zhang, P. Wang, A. Kuang, Z. Cheng, H. Yuan, and T. Yang, Doubly charged single Weyl pair with complete spin polarization, J. Mater. Chem. C **12**, 16799 (2024).

[135] G. Xu, H. Weng, Z. Wang, X. Dai, and Z. Fang, Chern semimetal and the quantized anomalous Hall effect in $HgCr_2Se_4$, Phys. Rev. Lett. **107**, 186806 (2011).

[136] L. Jin, X. Zhang, Y. Liu, X. Dai, L. Wang, and G. Liu, Fully spin-polarized double-Weyl fermions with type-III dispersion in the quasi-one-dimensional materials X_2RhF_6 (X = K, Rb, Cs), Phys. Rev. B **102**, 195104 (2020).

[137] S. Chen, R.-J. Slager, B. Monserrat, and A. Bouhon, High-chirality and multiquaternion Weyl nodes in hexagonal ReO_3, Phys. Rev. B **111**, 195110 (2025).

[138] X.-P. Li, K. Deng, B. Fu, Y. Li, D.-S. Ma, J. Han, J. Zhou, S. Zhou, and Y. Yao, Type-III Weyl semimetals: $(TaSe_4)_2I$, Phys. Rev. B **103**, L081402 (2021).

[139] Y. Chen, D. L. Bergman, and A. A. Burkov, Weyl fermions and the anomalous Hall effect in metallic ferromagnets, Phys. Rev. B **88**, 125110 (2013).

[140] J. Wang, H. Yuan, W. Wang, G. Ding, X.-P. Li, and X. Wang, Fully spin-polarized hourglass charge-three Weyl points and sextuple-helicoid surface arcs in $P6_322$-type $BaNiIO_6$, Phys. Rev. B **108**, 054424 (2023).

[141] G. Liu, P. Qin, J. Ren, Z. Chen, G. Zhou, and H. Xu, Magnetic triple Weyl semimetals that are robust against spin-orbit coupling, Phys. Rev. B **110**, L140409 (2024).

[142] Y. Li, L. Wu, S. Zhou, and H. Wu, $P6_322$-type $SrNiIO_6$: An ideal half-metallic candidate with a fully spin-polarized Weyl complex, Results Phys. **52**, 106829 (2023).

[143] X. Xiao, Y. Jin, D.-S. Ma, W. Kong, J. Fan, R. Wang, and X. Wu, Realization of charge-four Weyl point in fermionic systems, Phys. Rev. B **108**, 075130 (2023).

[144] B. Pan, Y. Hu, P. Zhou, H. Xiao, X. Yang, and L. Sun, Higher-order double-Weyl semimetal, Phys. Rev. B **109**, 035148 (2024).

[145] R. Wang, B. W. Xia, Z. J. Chen, B. B. Zheng, Y. J. Zhao, and H. Xu, Symmetry-protected topological triangular Weyl complex, Phys. Rev. Lett. **124**, 105303 (2020).

[146] Z. Huang, Z. Chen, B. Zheng, and H. Xu, Three-terminal Weyl complex with double surface arcs in a cubic lattice, npj Comput. Mater. **6**, 87 (2020).

[147] X.-F. Yang, Q.-B. Liu, Z.-Q. Wang, and H.-H. Fu, Unconventional charge-two Weyl phonons in high-symmetry lines, Adv. Phys. Res. **2**, 2300004 (2023).

[148] I. V. Getmanskii, R. M. Minyaev, D. V. Steglenko, V. V. Koval, S. A. Zaitsev, and V. I. Minkin, From two- to three-dimensional structures of a supertetrahedral borane using density functional calculations, Angew. Chem. Int. Ed. **56**, 10118 (2017).

[149] L. Cui, T. Song, J. Cai, X. Cui, Z. Liu, and J. Zhao, Three-dimensional borophene: A light-element topological nodal-line semimetal with direction-dependent type-II Weyl fermions, Phys. Rev. B **102**, 155133 (2020).

[150] A. R. Oganov and V. L. Solozhenko, Boron: A hunt for superhard polymorphs, J. Superhard Mater. **31**, 285 (2009).

[151] F. Mouhat and F.-X. Coudert, Necessary and sufficient elastic stability conditions in various crystal systems, Phys. Rev. B **90**, 224104 (2014).